HAL open science

Magnetic imaging of unconventional superconductors by scanning SQUID microscopy

Danny Hykel

To cite this version:

Danny Hykel. Magnetic imaging of unconventional superconductors by scanning SQUID microscopy. Other [cond-mat.other]. Université de Grenoble, 2011. English. NNT : 2011GRENY011 . tel-00579514

HAL Id: tel-00579514

https://theses.hal.science/tel-00579514v1

Submitted on 24 Mar 2011

HAL is a multi-disciplinary open access archive for the deposit and dissemination of scientific research documents, whether they are published or not. The documents may come from teaching and research institutions in France or abroad, or from public or private research centers.

L'archive ouverte pluridisciplinaire **HAL**, est destinée au dépôt et à la diffusion de documents scientifiques de niveau recherche, publiés ou non, émanant des établissements d'enseignement et de recherche français ou étrangers, des laboratoires publics ou privés.

UNIVERSITÉ DE GRENOBLE

THÈSE

Pour obtenir le grade de

DOCTEUR DE L'UNIVERSITÉ DE GRENOBLE

Spécialité : **Physique**

Arrêté ministériel : 7 août 2006

Présentée par

Danny HYKEL

Thèse dirigée par **Klaus HASSELBACH**

préparée au sein du **Institut Néel**
dans **l'École Doctorale Physique**

Microscopie à micro-SQUID: étude de la coexistence de la supraconductivité et du ferromagnétisme dans le composé UCoGe

Thèse soutenue publiquement le **15/02/2011**,
devant le jury composé de :

M. Hermann SUDEROW
Rapporteur
M. Alain PAUTRAT
Rapporteur
M. Hervé COURTOIS
Président
M. Klaus HASSELBACH
Directeur

L'art c'est moi, la science c'est nous.
Claude Bernard (1813-1878)

Remerciments

Le travail effectué pendant ma thèse n'aurait pas été possible sans l'aide de beaucoup de gens. Ainsi, en adaptant la fameuse phrase de Newton à notre salle de manip: "J'ai pu développer ce microscope parce que je me suis juché sur une boîte en bois pour atteindre le haut du cryostat".

Tout d'abord je voudrais remercier Alain Fontaine et André Sulpice de m'avoir accueilli au sein de l'Institut et du département. Je remercie Alain Pautrat, Hermann Suderow d'avoir accepté d'être membre de mon jury et d'être rapporteurs de mon travail. Je remercie également Hervé Courtois d'avoir accepté d'être le Président de ce jury.

Un grand merci à Klaus, qui m'a donné la possibilité de construire une manip "from scratch", qui m'a soutenu et m'a donné beaucoup de liberté dans mon travail. Il était toujours à l'ecoute pour discuter des nouvelles idées et m'aider à résoudre des problèmes. Klaus est probablement le seul directeur de thèse qui a déja transporté un de ses thesards en amazone sur son vélo.

I thank Dai Aoki for growing the UCoGe crystal. Je remercie Thierry Crozes, Dominique Mailly, Yves Gamberini, Arnaud Barbier et Karl Schuster pour la fabrication et le façonnage des SQUIDs en pointe.

Je remercie tous les chercheurs qui m'ont aidé tant sur le plan théorique qu'expérimental, comme Carley Paulsen, Elsa Lhotel et Pierre Rodière. I thank John Kirtley who taught me a lot of things during his stay: from some numerical simulations to his approach to focus on only one problem (if possible) per day.

Un très grand merci aux services électronique et mécanique. Notamment Julien Minet qui m'a beaucoup appris sur le plan électronique et informatique, Guillaume Bres qui a rapidement changé les amplificateurs brulés, ainsi que Maurice Grollier et Jean-Luc Mocellin qui ont été là quand j'ai eu besoin. Je remercie Olivier Exshaw pour les discussions geek et également Christoph Guttin, Gilbert Simiand et Pierre Carecchio. Je remercie Gregory Garde qui nous a fourni les pièces nécessaires à la construction du microscope et qui a aussi fabriqué les pieces pour le nouveau microscope. Je remercie Anne Gerardin pour la fabrication rapide de pièces.

Je remercie le gourou de LabVIEW Philippe Gandit, qui a pris le temps de discuter de la meilleure façon d'avancer, et Gerard Vermeulen qui m'a montré pas mal d'astuces en Python.

Je remercie les personnes qui ont "subi" mes répétitions et m'ont aidé à corriger ma thèse, entre autres Indranil Paul.

Je tiens à remercier les autres thésards, notamment Germain (qui m'a supporté pendant plus de trois années, cinq fois par semaines), Oana (qui nous a montré la beauté de la Roumanie et pour avoir organisé plein de fêtes chez elle), Thomas ("mon âme frère" par rapport aux blagues: on est arrivé de faire les mêmes blagues simultanément plus d'une fois), Io(a)n (qui nous a montré comment se comporter dans un contexte officiel, c'est impressionant!), Laetitia (pour sa gentillesse, sa bonne humeur et son aide à l'organisation du pot), Zhao (who taught me a lot about China and who impressed me with his patience, search of truth in my LabVIEW code and his skillful hands), Piotr (qui a eu souvent des histoires drôles à nous raconter, dont le rôle principal est souvent tenu par sa guitare), Yannick (qui aime les mêmes séries que moi), Johannes (avec qui j'ai eu des discussions très interessantes sur la physique), Gildas, David (mon partenaire de squash, on a réussi de perdre quatre balles en 20 minutes!), Maela (qui a su défendre la Bretagne à toutes les attaques), Raf

et Mikhail (who published the first paper with my name on it!). Je remercie également tous les thésards non mentionnés en les appelant *et al.*

Děkuji rodičům za všechno, co jste mi umožňili: šťastné dětství, studium, pobyt ve Francii a ještě mnohem více. Děkuji vám i za to, že jste přišli na můj doktorát, a samozřejmě za “žrádlo”!

Je voudrais remercier également Meryll qui connait toutes les parties du microscope qui peuvent être kaputt, ce qui lui fait regretter de poser des questions comme: “alors, ca avance?” ou “Tu as vu des vortex?”. Je la remercie d’avoir organisé la plus grande partie du tour de monde et aussi d’avoir cuisiné jusqu’à une heure du matin pour mon pot.

Abstract

We present the development of a scanning SQUID/AFM microscope and measurements performed on different samples. The microscope can take topographic and magnetic images simultaneously. The magnetic resolution is of the order of $10^{-4}\Phi_0/\sqrt{\mathrm{Hz}}$ and the spatial resolution of the SQUIDs used in this thesis goes up to 600 nm. The scanning range is 70 μm × 85 μm. The temperature range accessible is between 200 mK and 10 K at the time of writing.

Measurements on a thin rhenium film (80 nm) give an estimate of the minimal pinning force of a vortex of about 3.9×10^{-16} N. Furthermore, the penetration depth λ on this sample was determined as a function of temperature. For $T \to 0$, $\lambda \to 79$ nm.

We have for the first time shown local measurements of the domain structure of the superconducting ferromagnet UCoGe and determined the average domain size in the virgin state (10 μm). By magnetic imaging we were capable of determining the magnetic field difference above opposite domains along the **c**-axis to be 45 G and 16 G along the **b**-axis. Due to these magnetic field measurements we were able to give an upper limit for the domain wall width ($\sim$ 1 μm) and domain reconstruction depth (100 nm). This is supported by simple calculations leading to a domain wall width of several angstroms. Thus UCoGe can be considered an ideal Ising ferromagnet. Different possible domain structures for an Ising ferromagnet have been discussed. The complicated domain structure found in the zero field cooled virgin state corresponds to up domains embedded in larger down domains and vice versa.

We have shown evidence for coexistence of superconductivity and ferromagnetism. The weak Meissner effect can be explained by a spontaneous vortex state, put forward by other groups. Numerical simulations suggest that the strong magnetic background signal and the limited spatial and magnetic resolution of the used SQUID made it difficult to resolve the expected spontaneous vortex state.

The relaxation of the domain structure over a time scale of hours was observed. More work needs to be done to clarify the reason of this relaxation taking place at temperatures below 1K.

We showed that the theoretical prediction of domain shrinking, put forward by Fauré and Buzdin, when the sample temperature decreases below T_{SC} cannot be applied in its state to the case of UCoGe and discussed several reasons for this.

Keywords

SQUID/AFM microscopy, rhenium, penetration depth measurement, pinning force, UCoGe, SC/FM coexistence

Resumé français

Cette thèse porte sur le développement d'un microscope SQUID/AFM qui permet de réaliser des images magnétiques et topographiques simultanément. La résolution magnétique est de l'ordre de $10^{-4}\Phi_0/\sqrt{\text{Hz}}$. La résolution spatiale des SQUIDs utilisés est de 600 nm et 1100 nm. La taille maximale d'une image, étalonnée avec un échantillon de niobium avec des motifs d'échiquier, est de 70 μm × 85 μm. La plage accessible de température de l'échantillon est comprise actuellement entre 200 mK et 10 K.

Le microscope a été utilisé pour faire de l'imagerie magnétique sur trois échantillons: un film de niobium pour la calibration, comme déjà mentionné, un film de rhénium fabriqué de façon épitaxiale et un cristal d'UCoGe qui est un supraconducteur ferromagnétique.

Ci-dessous un résumé des différents chapitres.

Chapitre 1: Supraconductivité conventionnelle

Dans ce chapitre tous les concepts de la supraconductivité utiles à la bonne compréhension du dispositif expérimental, notamment le fonctionnement du SQUID, sont introduits. Tout d'abord les équations de London sont presentées, puis la théorie de Ginzburg-Landau est utilisée pour comprendre l'effet de la quantification du flux magnétique dans une boucle supraconductrice fermée. Enfin, le lien avec la théorie BCS est fait brièvement et les champs critiques dues aux effets orbitaux et paramagnétiques sont abordés.

Chapitre 2: Dispositif expérimental

Le dispositif expérimental est décrit en commençant tout d'abord par la caractérisation de nos SQUIDs. Le diapason, notre capteur de force, et la microscopie à champs proche sont introduits. L'électronique ainsi que les logiciels implémentés pendant la thèse sont expliqués. Enfin, les mesures de calibration sur un film de niobium avec un motif d'échiquier sont discutées et les perspectives d'amélioration sont données.

Chapitre 3: Comparaison à d'autres microscopes

Le microscope est comparé à d'autres techniques d'imagerie magnétique et en particulier à d'autres microscopes à SQUID et sonde de Hall sur le plan de la résolution spatiale et magnétique, la durée d'acquisition d'une image, la fiabilité et les contraintes pratiques. Ceci, nous permet d'orienter le futur développement. De plus, brièvement, une méthode pour une imagerie à haute vitesse est introduite.

Chapitre 4: Mesures sur un film de rhénium

Dans ce chapitre, les mesures de caractérisation effectuées sur un film de rhénium d'une épaisseur de 80 nm, crû par epitaxie, sont présentées. En particulier, la force de piègage d'un vortex est estimée à $F = 3.9 \times 10^{-16}$ N et la longueur de pénétration du film en fonction de la température est déterminée ($\lambda(T \to 0) = 79$ nm).

Chapitre 5: Supraconductivité non-conventionnelle

Ce chapitre introduit la supraconductivité non-conventionnelle. On discute le cas du composé UCoGe, un supraconducteur ferromagnétique avec une température de Curie d'environ 2.5 K et une température de transition supraconductrice de 0.5 K. Les mesures effectuées par d'autres groupes, montrant la coexistence entre l'état superconducteur et l'état ferromagnetique, sont abordées. Les calculs théoriques prédisant la diminution de la taille de domaine dans l'état supraconducteur (par rapport à l'état normal) sont présentés.

Chapitre 6: Mesures sur UCoGe

Le dernier chapitre aborde les mesures effectuées par microscopie à SQUID sur un échantillon d'UCoGe crû par Dai Aoki. Ce chapitre présente les premieres images de la transition ferromagnétique et l'apparition d'une structure de domaines dans un supraconducteur ferromagnétique. Les mesures sont cohérentes avec les mesures de volume effectuées par C. Paulsen. Le comportement des domaines sous différents champs et états (état normal, état supraconducteur) est étudié. Enfin, on montre les relaxations de la structure des domaines sur une échelle de temps de quelques heures au bord de l'échantillon.

Des simulations numériques effectuées montrent que la résolution spatiale et magnétique du SQUID utilisé n'est pas satisfaisante pour observer les vortex dans ce composé. Les résultats de ces simulations soutiennent l'hypothèse d'état à vortex spontané.

Contents

1 Conventional superconductivity 3
1.1 Introduction . . . 3
1.2 London equations . . . 4
1.3 Ginzburg-Landau Theory . . . 5
1.3.1 Landau's theory of second order phase transitions . . . 6
1.3.2 Superconducting transition . . . 6
1.3.3 Coherence length and penetration depth . . . 7
1.3.4 Two types of superconductors . . . 9
1.3.5 Flux quantisation . . . 10
1.3.6 Vortex lattice . . . 11
1.3.7 Josephson effect . . . 12
1.3.8 SQUID . . . 12
1.4 Relation with BCS Theory . . . 13
1.4.1 Magnetic limits . . . 14

2 Experimental setup 16
2.1 Introduction . . . 16
2.2 SQUID . . . 17
2.3 Introduction . . . 17
2.3.1 Fabrication . . . 18
2.3.2 Measurement of the critical current . . . 19
2.3.3 Characterisation . . . 20
2.3.4 Noise estimation . . . 21
2.4 AFM . . . 22
2.4.1 Introduction . . . 22
2.4.2 Modelisation . . . 23
2.4.3 Tuning fork properties . . . 24
2.5 Tuning fork resonance frequency . . . 25
2.6 Thermal behaviour of the frequency spectrum . . . 26
2.7 Regulation . . . 27
2.7.1 Z-Actuator . . . 27
2.7.2 Regulation . . . 27
2.8 Scanner . . . 28
2.8.1 Introduction . . . 28
2.8.2 Deviation from plane . . . 29
2.9 Imaging . . . 30
2.10 Coarse Positioning . . . 31
2.10.1 Coarse lateral positioning . . . 32
2.10.2 Coarse approach . . . 33
2.11 Cryostat . . . 34
2.12 Magnetic field . . . 36
2.13 Electronics . . . 36
2.13.1 Overview . . . 36

2.13.2 Thermometry . . . 36
2.13.3 Motor control . . . 38
2.14 SQUID read-out and tuning fork excitation . . . 38
2.15 Software . . . 39
2.15.1 Overview . . . 39
2.15.2 Regulation . . . 39
2.16 Validation and Calibration of the microscope . . . 40
2.16.1 Approach-Curves . . . 41
2.16.2 Calibration . . . 41
2.17 Possible improvements . . . 46

3 Comparison with other microscopes 48
3.1 General techniques . . . 48
3.2 Scanning Hall probe microscopy . . . 50
3.3 Scanning SQUID microscopy . . . 50
3.3.1 Stanford group . . . 51
3.3.2 Weizmann group . . . 52
3.4 High speed scanning SQUID microscopy . . . 53

4 Rhenium 54
4.1 Introduction . . . 54
4.2 Vortex penetration . . . 55
4.3 Vortex pinning . . . 56
4.3.1 SQUID/vortex interaction . . . 57
4.3.2 Pinning force estimation . . . 59
4.3.3 Comparison . . . 60
4.4 Penetration depth measurements . . . 61
4.4.1 Introduction . . . 61
4.4.2 Confidence region . . . 62
4.4.3 Fitting the vortex profiles . . . 63
4.5 Tip abrasion . . . 65
4.6 Conclusion . . . 65

5 Unconventional superconductivity in UCoGe 67
5.1 Introduction . . . 67
5.2 Symmetry of the order parameter . . . 67
5.3 Different families of unconventional superconductors . . . 68
5.4 Heavy fermions . . . 69
5.5 Behaviour of magnetic domains in a ferromagnetic superconductor . . . 71
5.6 UCoGe . . . 73
5.6.1 Introduction . . . 73
5.6.2 Sample quality . . . 73
5.6.3 Ferromagnetism . . . 74
5.6.4 Superconductivity coexisting with ferromagnetic order . . . 75
5.6.5 Order Parameter . . . 76
5.6.6 Pressure Phase Diagram . . . 76
5.6.7 Estimates for coherence length and penetration depth . . . 77
5.6.8 Other aspects . . . 77
5.6.9 Conclusion . . . 77
5.6.10 Open Questions . . . 78

6 Measurements on UCoGe 80
6.1 Introduction . . . 80

6.2 Sample fabrication and preparation . . . 80
6.3 Interpretation of the critical current images . . . 81
6.3.1 Introduction . . . 81
6.3.2 Laplace equation . . . 82
6.3.3 Numerical calculations . . . 84
6.3.4 Magnetic domains . . . 84
6.3.5 Images at different heights . . . 88
6.4 Specific heat . . . 88
6.5 Susceptibility . . . 88
6.6 Magnetic field measurements . . . 89
6.6.1 Ferromagnetic transition . . . 89
6.6.2 Diamagnetic screening . . . 91
6.6.3 Meissner effect . . . 94
6.6.4 Hysteresis . . . 96
6.6.5 Conclusion . . . 101
6.7 Vortex lattice . . . 105
6.7.1 Introduction . . . 105
6.7.2 Perfect vortex lattice . . . 106
6.7.3 Disordered vortex lattice . . . 107
6.8 Behaviour of domain walls . . . 108
6.8.1 Field cooled . . . 109
6.8.2 Border . . . 109
6.8.3 Center . . . 110
6.8.4 Discussion . . . 111
6.9 Conclusion . . . 112
6.10 Outlook . . . 113

References 115

Introduction

Since the discovery of superconductivity (SC) in 1911 much experimental and theoretical progress has been made. First pragmatic and phenomenological theories like the London model and the Ginzburg-Landau theory were proposed. Later, the BCS theory explained superconductivity on the microscopic scale. However, new superconducting materials not explicable by BCS theory appeared. In 1979 heavy fermions superconductors and later high T_{SC} cuprates were discovered. Both are highly correlated electron systems close to magnetic instabilities. For the moment no unique theory exists. What is more, recently several uranium based compounds with coexistence of SC and ferromagnetism were reported, two orders formerly considered antagonistic.

On the experimental side, technical progress lead from bulk and transport measurements to sophisticated scientific instruments like synchrotrons, neutron reactors and high field laboratories. But also on the laboratory scale scanning tunneling microscopy (STM) and atomic force microscopy (AFM) opened up the way to surface science in real space on the local scale. AFM tips equipped with magnetic sensors like Hall probes or magnetic tips have been found to be useful in order to probe the magnetic field distributions above the sample surface dynamically in contrast to the static Bitter decoration technique successfully used since the late 1960s.

Superconducting QUantum Interference Devices (SQUIDs) are very versatile systems permitting to measure the flux penetrating them by the determining their critical current and are used for different applications like brain scans or material fatigue science.

They were first used to image the magnetic flux distribution above superconductors in the 1990s. In our group a first microscope combining AFM and SQUID microscopy was built 10 years ago by C. Veauvy and K. Hasselbach using a SQUID positioned close to the edge of the Si substrate. This edge corresponds to the physical tip used for tuning fork based AFM.

In this thesis we present a newly developed scanning SQUID/AFM microscope. The SQUID sizes used during our measurements were 1.1 µm and 0.6 µm (limiting the spatial resolution). The SQUID/sample distance is typically $\sim$ 500 nm. We project that future SQUIDs could be as small as 200 nm and that the distance could be reduced to $\sim$ 50 nm increasing the spatial and magnetic resolution considerably, putting it far ahead of currently available devices.

The advantage of using AFM to regulate the SQUID/sample distance is twofold: First, we can detect surface defects and correlate them with the magnetic image, giving rise to the possibility to observe vortex pinning centers or to analyse nano-fabricated devices magnetically and topographically. Second, in contrast to simpler techniques, it allows the user to take images at different distances above the sample to probe the evolution of the magnetic field with height.

In this work we will discuss measurements done on three different samples. A patterned niobium film was used to make calibration measurements and to characterize the microscope's performance.

Furthermore, measurements were performed on an epitaxially grown rhenium film. We determined the temperature dependence of the absolute value of the penetration depth, the field value H_{relax} upon which vortices in the sample move collectively and the vortex pinning force.

In 2007 a new superconducting ferromagnet UCoGe was discovered with properties perfectly adapted to our scanning SQUID microscopy: it has transition temperatures well in the range accessible by our microscope ($\sim$ 0.5 K and $\sim$ 2.5 K for the superconducting and ferromagnetic transition temperature,

respectively) and shows both transitions at ambient pressure.

We will present the first magnetic images made on a superconducting ferromagnet and its domain structure. Moreover, the behaviour under different fields and between the superconducting and normal state will be addressed in detail.

Several numerical calculations were performed to help interpret the images and to extract quantitative results from the data. Two main calculations can be distinguished: modelling the field above an Ising magnet and above a vortex lattice.

The outline of this thesis is as follows:

In chapter 1 I will give a brief introduction to conventional superconductivity needed for understanding the working principles of the microscope, notably the SQUID.

The experimental setup will be be discussed in chapter 2. We will characterize the SQUIDs used during this thesis, explain the working principles of AFM and how it is implemented using a tuning fork as a force sensor. A large part of this chapter is devoted to the electronics and software development that has been achieved during this thesis. Finally, the first calibration measurements will be discussed to analyse the performance of the microscope. Possible short and long-term improvements of the experimental setup are assessed.

The microscope will be compared to other setups from other groups in chapter 3. This is useful in order to plan future improvements and developments as it gives an orientation in the vast experimental parameter space (spatial resolution, image acquisition time, magnetic resolution, reliability and practical constraints). An experimentalist has to choose a very confined space in this parameter space and make compromises that are well adapted to the physics in question. At the end of this chapter, we will also briefly present a new method of scanning SQUID microscopy allowing for images to be taken in seconds instead of hours.

In chapter 4 we will discuss the experimental results on a thin rhenium film (80 nm). We will deduce several physical quantities like the absolute value of the penetration depth, magnetic fields linked to vortex movement and the vortex pinning force. In order to determine the latter we will introduce a simple model allowing for an estimate of the SQUID/vortex interaction.

Chapter 5 gives a brief introduction of unconventional superconductivity and discusses measurements realized on the superconducting ferromagnet UCoGe. This compound exhibits local coexistence of ferromagnetism and superconductivity. The Curie temperature is about ~ 2.5 K, whereas superconductivity appears at ~ 0.5 K. Theoretical calculations, put forward by M. Fauré and A. Buzdin, predicting domain structure shrinking between the normal state and the superconducting state are presented and their relevance to the case of UCoGe is examined.

In the last chapter we will discuss measurements on UCoGe made on samples grown by Dai Aoki. We will present the first images of the domain structure of a superconducting ferromagnet. The results are consistent with bulk measurements performed by C. Paulsen. The domain structure behaviour dependence on the applied field, the temperature (SC or normal state) will be described. We will also show meta-stable states with relaxation times of several hours or longer.

Numerical calculations will show that the spatial and magnetic resolution of the used SQUID were not sufficient to resolve vortices in this compound. The results of the simulations support the hypothesis of the first compound presenting a spontaneous vortex phase.

1 Conventional superconductivity

In this chapter I will briefly discuss some aspects of conventional superconductivity which are important for the understanding of the experimental setup and our measurements. First I will recall the historical key events, then introduce the London model. After a brief introduction of Landau's theory of second order phase transitions and the Ginzburg-Landau theory, I will allude to some properties of conventional superconductors. I will conclude the chapter with the key point of our microscope: superconducting quantum interference devices, before finishing with limiting magnetic fields of SC.

1.1 Introduction

In 1911, Kamerlingh Onnes and Gilles Holst found that the resistance of mercury goes to zero below T_{SC}, which is the critical temperature of mercury [1].

In 1933 it was discovered that the magnetic field in a superconductor is expelled when cooling the sample below T_{SC} [3]. The perfect diamagnetic behaviour is named after its discoverers the **Meissner-Ochsenfeld effect**. The magnetic field is excluded from the interiour in the two following cases: By cooling down below T_{SC} and applying a field (ideal conductor) and by inversing the order of this process. By the independence of the order of these two processes (cooling down, applying a magnetic field) the Meissner-Ochsenfeld effect demonstrates that the superconducting state is a true thermodynamical state.

In 1935, Fritz and Heinz **London** put forward a simple model to explain the zero resistivity and the Meissner-Ochsenfeld effect [4]. In order to explain these two aspects they made the following two assumptions: first, that there is a density n_s of electrons moving without resistance and second, n_s, has to be zero at T_{SC} and grow steadily with lower temperatures. In combination with Maxwell's equations the London equations establish the electrodynamics of superconductors.

It took another 15 years and Landau's theory of phase transitions to develop a phenomenological theory (**Ginzburg-Landau theory** [5]) of superconductivity that renders possible the description of phenomena where the spatial variation of n_s is crucial. One famous example is the vortex lattice, first described by Abrikosov in 1957 [6].

By that time, it was also tried to grasp the underlying microscopic physics. This effort culminated in the **BCS theory**[1] [7], [8]. A requirement for the BCS theory is an attractive potential between

[1] after Bardeen, Cooper and Schrieffer

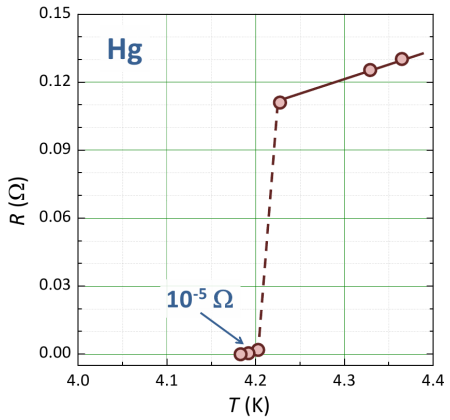

Figure 1.1: Discovery of superconductivity in mercury in 1911 by Kamerlingh Onnes [1] by resistivity measurements. Image taken from [2].

electrons that is stronger than the Coulomb repulsion. The intuitive picture is the following: An electron that passes the ions of the lattice interacts with them, but because of their inertia their reponse is too slow so that once the electron is gone a positive charge density attracts another electron. This attractive interaction was put forward by Fröhlich in 1950 [9].

Also in 1950, Fröhlich predicted the **isotope effect** [10], i.e. the anti-correlation of the T_{SC} of a superconducting element with its isotopic mass that was experimentally discovered by Maxwell [11] and later Reynolds [12]. This was the decisive proof that phonons are the origin of the attractive potenial.

In 1956, Cooper showed that the attractive interaction - even if arbitrarily weak - would lead to an instability of the Fermi sea and to a bound state of two electrons called **Cooper-pairs** [13].

The most important prediction made by the BCS theory is the energy gap $\Delta = 1.76 k_B T_{SC}$ that opens up at the Fermi level. The energy gap is responsible for the exponential behaviour of several physical quantities observed experimentally, like specific heat.

1.2 London equations

As mentioned in the introduction F. and H. London developed a simple model accounting for the electromagnetic properties of a superconductor [4] using the equation of motion of the electron in the Drude model as a starting point:

$$m\frac{d\mathbf{v}}{dt} = q\mathbf{E} - m\frac{\mathbf{v}_{drift}}{\tau} \tag{1.1}$$

with τ being the time between collisions ($\tau \to \infty$ for an ideal conductor) and m and q corresponding to the mass and charge of the superconducting particles. To account for the different behaviour in the normal and superconducting state it seems plausible to use a **two liquids model** to describe superconductivity. We assume that the total charge carrier density n can be written as the sum of two contributions: the density of normal carriers n_n and the density of superconducting carrier n_s. We further assume $n = n_n$ in normal state and $n = n_s$ at $T \to 0$.

By using $\mathbf{j} = -en\mathbf{v}$ the superconducting current can be written as (**first London equation**):

$$\frac{\partial\left(\frac{m_s}{n_s q_s^2}\right)\mathbf{J_s}}{\partial t} = \mathbf{E} \tag{1.2}$$

The physical meaning of this equation is the zero resistivity of a superconductor, since in contrast to Ohm's law $J = \sigma \mathbf{E}$ it is the derivative of the current density that is proportional to the electric field.

Applying the third Maxwell equation ($\nabla \times \mathbf{E} + \frac{\partial \mathbf{B}}{\partial t} = 0$) to equation 1.2 yields:

$$\frac{\partial}{\partial t}\left[\nabla \times \frac{m_s}{n_s q_s^2}\mathbf{J_s} + \mathbf{B}\right] = 0 \tag{1.3}$$

This equation applies for all ideal conductors: the magnetic flux through an arbitrary area inside the sample is constant in time. But the Meissner-Ochsenfeld effect states that the flux itself has to disappear. This leads to **second London equation**:

$$\nabla \times \frac{m_s}{n_s q_s^2}\mathbf{J_s} + \mathbf{B} = 0 \tag{1.4}$$

In the case of a superconductor in the $x > 0$ half space with an applied field $\mathbf{B} = B_0\mathbf{z}$ the solution of equation 1.4 is

$$B_z(x) = B_0 e^{-x/\lambda_L}$$
$$J_{s,y}(x) = J_{s,0} e^{-x/\lambda_L}$$

with λ_L being the **London penetration depth**, given by:

$$\lambda_L = \sqrt{\frac{m_s}{\mu_0 n_s e_s^2}} \tag{1.5}$$

with μ_0 being the vacuum permeability.

This means that the magnetic field penetrates only in a thin layer, at the surface of the superconductor, with a characteristic thickness of λ.

Remark: In the derivation of the London equations we used local relations between $\mathbf{J_s}$, $\mathbf{E}$ and $\mathbf{B}$. For an electron gas one has always to consider the mean value in a sphere with a diameter l (free mean path). But this free mean path goes to infinity for $\tau \to \infty$. Pippard introduced the coherence length $\xi_0 = \frac{\hbar v_F}{\pi \Delta(0)} = 0.18 \frac{\hbar v_F}{k_B T_{SC}}$ (with the superconducting gap $\Delta(0)$ and the Fermi velocity v_F) in order to account for discrepancies between experimental estimations and λ_L due to non-local effects. The coherence length is the shortest length scale on which physical quantities of a superconductor, like n_s, can vary. The London penetration depth can only be defined in the case $\lambda \gg \xi$.

1.3 Ginzburg-Landau Theory

In the London theory the density of superconducting carriers is constant in space. In reality, this cannot be the case at the surface of a superconducting sample or a superconducting/normal interface.

In 1950, Ginzburg and Landau (GL) put forward a theory that can be used in the case of a spatial variation of n_s [5]. The GL theory is an enhanced version of the Landau theory of second order phase transitions [14], [15] in which a complex, spatially varying order parameter is used instead of a real, spatially constant one:

$$\Psi(\mathbf{r}, t) = \Psi(\mathbf{r}, t)\exp(i\theta(\mathbf{r}, t)) \tag{1.6}$$

The square of the absolute value of this order parameter corresponds to n_s.

In contrast to the London theory the GL theory also explains the phase transition between the normal and superconducting state near T_{SC}, gives rise to the notion of a critical field and it predicts flux quantisation (one of its huge successes).

In the following, we first discuss Landau's theory of second order phase transitions and then discuss the implication of a macroscopic wavefunction in more detail.

1.3.1 Landau's theory of second order phase transitions

Landau's theory of second order phase transitions[2] is a framework to study transitions like paramagnetism/ferromagnetism. It introduces the notion of an order parameter Ψ that evolves continuously from zero (just above the transition temperature) in the unordered, higher symmetry phase to a non-zero value in the ordered, symmetry-broken phase.

One can develop the free energy F in terms of the order parameter (close to the transition temperature). An important point is, that the expansion of F has the same symmetry as the Hamiltonian of the system and thus not all terms of the Taylor expansion appear in the free energy.

This order parameter can be for example the magnetization (magnetic transition), the difference between two lengths in a lattice (structural transition) or the electric polarisation (ferroelectric transition).

In the case of an Ising ferromagnet this free energy expansion yields (cutting off at fourth order):

$$F = aM^2 + bM^4 + constant \tag{1.7}$$

with M being the absolute value of the magnetisation and the order parameter of the system. a and b are functions of temperature. Because the symmetry $\mathbf{M} \rightarrow -\mathbf{M}$ yields, only even power terms appear.

By minimizing this free energy with respect to M we obtain:

$$2aM + 4bM^3 = 0 \Rightarrow M = 0 \; or \; M_s = \pm\sqrt{\frac{a}{2b}} \tag{1.8}$$

In figure 1.2 the free energy for the above calculated one-dimensional order parameter is depicted. Above the transition temperature the lowest free energy is obtained for zero magnetization. As one crosses the transition temperature (T_{Curie} for $a < 0$) two absolute minima appear at finite magnetization values. These two values correspond to a spontaneous magnetisation: Without the influence of an external magnetic field, the system has the magnetization $+M_s$ or $-M_s$.

Once the system is in the state $-M_s$, one has to overcome the local minimum of the free energy curve in order to drive the system into the M_s state. This is done by applying a magnetic field in positive direction until the dip of the $-M_s$ state disappears and the system falls into the now deeper M_s valley. This effect is called hysteresis.

1.3.2 Superconducting transition

In contrast to the above described ferromagnetic transition, Ginzburg and Landau proposed a complex order parameter - inspired by the quantum mechanical wavefunction for a free electron[3] -

[2] 1st order phase transitions: the symmetries of two phases can be unrelated, 2nd order phase transitions: the symmetries of the two phases are related through symmetry breaking.

[3] It is interesting to notice that Fritz London deduced the London equations by starting with the assumption of a wave function of the same form [16]. He had realized that the superconductivity is an inherently quantum mechanical phenomenon.

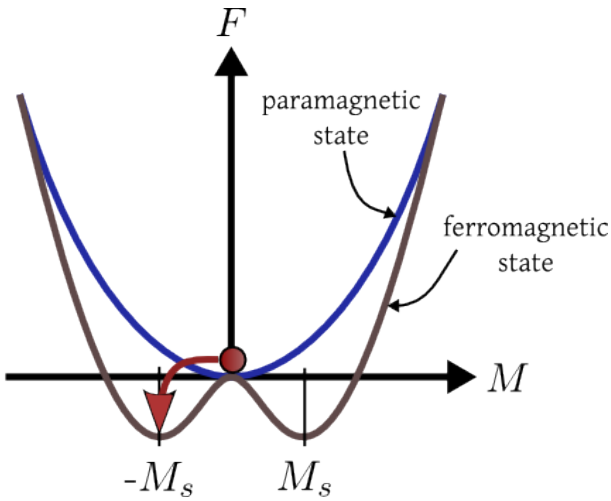

Figure 1.2: The free energy vs. magnetisation dependence for the paramagnetic and the ferromagnetic state. The system (represented by the red circle) will minimize its free energy by a spontaneous magnetisation. Note that constant contributions are neglected.

$\Psi = \| \Psi(\mathbf{r}) \| \exp(i\theta(\mathbf{r}))$. The norm of this position dependent order parameter describes the density of the superconducting carriers (Cooper pairs).

In this section we will denote the mass m_s and the charge q_s as m and $-2e$, respectively.

With this complex order parameter the notion of a phase in the system gets established[4], so the free energy has to be invariant under $\Psi \to \Psi \exp(i\varphi)$. Thus, considering the magnetic field energy and the coupling to the superconducting current the free energy can be written as (developing to fourth order):

$$F = F_n + \alpha |\Psi(\mathbf{r})|^2 + \frac{1}{2}\beta |\Psi(\mathbf{r})|^4 + \frac{|\mathbf{B}|^2}{2\mu_0} + \frac{1}{2m}\left|\left(\frac{\hbar}{i}\nabla - 2e\mathbf{A}\right)\right|^2 \tag{1.9}$$

The free energy for this order parameter is illustrated in figure 1.3. When the system crosses the superconducting transition its former minimum becomes unstable and the system finds a new minimum with a random phase (symmetry breaking). Notice the rotational symmetry of the free energy. The difference between the one-dimensional (figure 1.2) and the two-dimensional case is that in the latter the minima all lie on a circle thus the system can get from one phase to another without having to overcome the central hump. This has consequences that will become apparent when we will talk about SQUIDs: a ring with a continuously evolving phase along the path around it.

The next step is to minimize the free energy with respect to the vector potential A and Ψ. This yields the **Ginzburg-Landau equations**:

$$\alpha\Psi + \beta |\Psi|^2 \Psi + \frac{1}{2m}(-i\hbar\nabla + 2e\mathbf{A})^2 \Psi = 0 \tag{1.10}$$

$$\mathbf{J_s} = \frac{ie\hbar}{m}\left(\Phi^*\nabla\Psi - \Psi\nabla\Psi^*\right) - \frac{4e^2}{m}|\Psi|^2 \mathbf{A} \tag{1.11}$$

1.3.3 Coherence length and penetration depth

Two characteristic length scales can be defined in the GL theory: the penetration depth λ and the coherence length ξ. First, we derive the former:

[4]The symmetry broken is called U(1): gauge symmetry

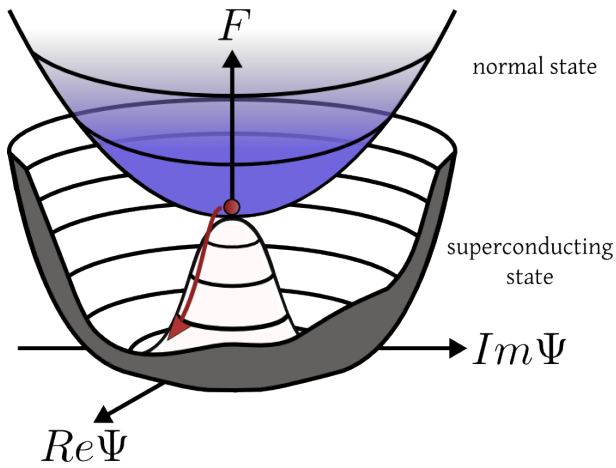

Figure 1.3: The order parameter dependence of the free energy. When crossing the transition the system (represented by the red sphere) finds itself at a local maximum and relaxes into an arbitrary minimum. Note that constant contributions are neglected.

The order parameter in a large sample without magnetic field is constant and the first GL equation 1.10 becomes simply $|\Psi|^2 = -\alpha/\beta$. By plugging this into the second GL equation 1.11 we obtain:

$$\mathbf{J_s} = \frac{4e^2}{m}\frac{|\alpha|}{\beta}\mathbf{A} \tag{1.12}$$

Comparing this with the second London equation 1.4 yields a penetration depth of

$$\lambda = \sqrt{\frac{m\beta}{4\mu_0 e^2 |\alpha|}} \tag{1.13}$$

thus the penetration depth of both theories is identical.

As already mentioned, the coherence length is the characteristic length scale of the variation of the order parameter. In order to deduce it, we consider the surface of a superconductor extending into the halfspace $x > 0$ without magnetic field. The first GL equation can then be written in one dimension as follows:

$$-\frac{\hbar^2}{2m}\frac{d^2\Psi}{dx^2} + \alpha\Psi + \beta\Psi^3 = 0 \tag{1.14}$$

We now define the convenience function $f = \Psi(x)/\Psi_\infty$. The denominator, Ψ_∞, represents the solution $x \to \infty$ (deep inside the sample). Thus equation 1.14 can be rewritten as:

$$\frac{\hbar^2}{2m|\alpha|}\frac{d^2 f(x)}{dx^2} + f(x) - f^3(x) = 0 \tag{1.15}$$

With the boundary conditions:

$$f(0) = 0 \tag{1.16}$$
$$\lim_{x\to\infty} f(x) = 1 \tag{1.17}$$
$$\lim_{x\to\infty} df(x)/dx = 0 \tag{1.18}$$

we obtain the following solution:

$$f(x) = \tanh\frac{x}{\sqrt{2}\xi} \tag{1.19}$$

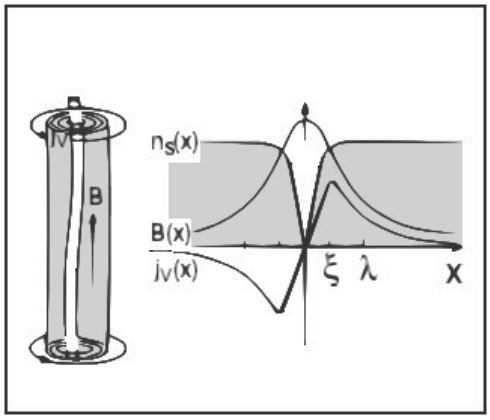

Figure 1.4: Illustration of a vortex: inside the vortex the Cooper pair density drops to zero. The penetrating magnetic flux is shielded by a circulating current, from: [19].

with $\xi = \frac{\hbar^2}{2m|a|}$ the coherence length: the order parameter at the surface rises from zero to one on a length scale of ξ.

In the BCS picture the coherence length can be imagined as the approximate extent of a Cooper pair.

1.3.4 Two types of superconductors

In magnetic field we distinguish between two types of superconductors. The type depends on which of the two characteristic length scales (coherence length and penetration depth) dominates. In the following I want to use a simplified illustration to distinguish these two types [17]. We will replace the continuous spatial evolution of the Cooper pair density by a step function.

The coherence length ξ is the extent of the Cooper pair depleted region Ξ (this region is at the normal/superconducting interface). The penetration depth λ determines the thickness of a region Λ into which the magnetic field can penetrate.

As there are no Cooper pairs in Ξ, the system does not gain any condensation energy. On the other hand, the system does gains magnetic energy in Λ, since the field is not expelled there.

Thus, there are two possible types of superconductors in regard to their behaviour when they are exposed to a magnetic field, that wants to penetrate in the superconductor:

- $\xi > \lambda$: The system wants to gain condensation energy and minimizes the interfaces (*type I*). If the applied field exceeds H_c the whole system is in the normal state.
- $\xi < \lambda$: The interfaces becomes energetically more favourable and the system (in a *type II* superconductor) tries to maximize them by letting single flux quanta (see next section) enter the bulk in the form of vortices. Vortices are regions where the order parameter drops to zero and a superconducting current encloses the penetrating magnetic flux (see figure 1.4). With increasing magnetic field more and more vortices nucleate until the core regions overlap and superconductivity vanishes. The corresponding field is called $H_{c2} = \frac{\Phi_0}{2\pi\xi^2}$.

When we take the smoothness of the Cooper pair density and the critical current at interfaces into account, we obtain a type I superconductor if $\kappa < \frac{1}{\sqrt{2}}$ and otherwise a type II superconductor (with $\kappa = \frac{\lambda}{\xi}$ being the Landau parameter)[5].

In the following sections we will discuss some consequences of the GL-Theory that are due to the

[5] for the derivation see [18]

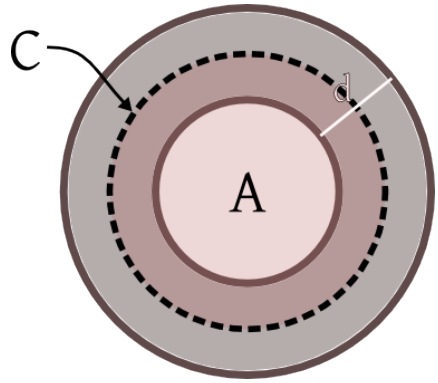

Figure 1.5: A superconducting ring of thickness d enclosing a magnetic flux Φ in the area A. The curve C is deep inside the superconductor (no supercurrents). See discussion in the text.

notion of a macroscopic wave function.

1.3.5 Flux quantisation

Before discussing the flux quantization we have to derive the **superconducting current density**:

$$\begin{aligned} \mathbf{J} &= Re\{\Psi^* \frac{\mathbf{p}}{m}\Psi\} && (1.20)\\ &= Re\{\Psi^* \left(\frac{\hbar}{im_s}\nabla - \frac{q_s}{m_s}\mathbf{A}\right)\Psi\} && (1.21)\\ &= \frac{q_s\hbar}{2m_s i}\left(\Psi^*\nabla\Psi - \Psi\nabla\Psi^*\right) - \frac{q_s^2}{m_s}\Psi\Psi^*\mathbf{A} && (1.22) \end{aligned}$$

by replacing the canonical momentum $\mathbf{p}$ by $\frac{\hbar}{i}\nabla - q\mathbf{A}$, q by q_s and m by m_s.

Plugging in the wave function from equation 1.6 yields:

$$\mathbf{J_s} = q_s n_s(\mathbf{r},t)\underbrace{\{\frac{\hbar}{m_s}\nabla\theta(\mathbf{r},t) - \frac{q_s}{m_s}\mathbf{A}(\mathbf{r},t)\}}_{\mathbf{v_s}} \tag{1.23}$$

Let us imagine a superconducting ring (see figure 1.5) that is cooled below T_{SC}. By applying a field $\mathbf{B}$ perpendicular to the ring plane, we can induce a stationary supercurrent. In the classical case, one could obtain any value for the supercurrent I_s for different values of $B_\perp$. But the superconducting state is a macroscopic quantum mechanical state, thus stationary states are described by quantum numbers. In the system at hand these stationary states can be represented as standing waves around the ring, thus we expect a quantization. This was first suggested by F. London [16].

By integrating equation 1.23 along a closed loop C, we obtain (using the Stokes theorem):

$$\oint_C \frac{m_s}{n_s q_s}\mathbf{J_s}\cdot d\mathbf{l} + \int_A \mathbf{B}\cdot d\mathbf{s} = \frac{\hbar}{q_s}\oint_C \nabla\theta\cdot d\mathbf{l} \tag{1.24}$$

with A being the area inside the closed loop C.

The integral on the right hand side has an infinity of solutions of the form $2\pi n$ as the wave function has to be a single-valued function.

Hence equation 1.24 can be written as:

$$\oint_C \frac{m_s}{n_s q_s}\mathbf{J_s}\cdot d\mathbf{l} + \int_A \mathbf{B}\cdot d\mathbf{s} = n\Phi_0 \tag{1.25}$$

with $\Phi_0 = \frac{h}{|q_s|} = \frac{h}{2e}$ being the flux quantum:

$$\Phi_0 = \frac{h}{2e} \approx 2.07 \times 10^{-15} \text{ Wb} \tag{1.26}$$

If the ring is thick enough so that we can choose a closed loop C deep inside the ring, we can neglect the term corresponding to the superconducting current and we obtain:

$$\int_A \mathbf{B} \cdot d\mathbf{s} = n\Phi_0 \tag{1.27}$$

This means that the flux trapped inside the ring is quantized. This quantization has been measured independently by two groups in 1961 (R. Doll, M. Näbauer [20] and B.S. Deaver, W. M. Fairbanks [21]).

1.3.6 Vortex lattice

One manifestation of the flux quantization discussed in the previous section is the vortex state. As was mentioned above, there exist a Meissner and a vortex state for type II superconductors. Experimentally however, it is very rare not to observe any vortices in a sample. This is due to the fact that the ambient magnetic field is trapped in the form of vortices by defects in the material where superconductivity is weakened. When the applied field is increased the vortex density and inter-vortex repulsion will grow. It was shown by Abrikosov in 1957 [6] that the vortices will form a lattice to minimize the energy of the system.

The vortex lattice was first observed by U. Essmann and H. Träuble [22] by means of Bitter decoration in 1967 (see figure 1.6(a)).

Nowadays, this lattice can also be seen by near field imaging techniques like STM [23] (see figure 1.6(b)).

We will discuss the vortex lattice in chapter 6 in the context of our numerical simulations.

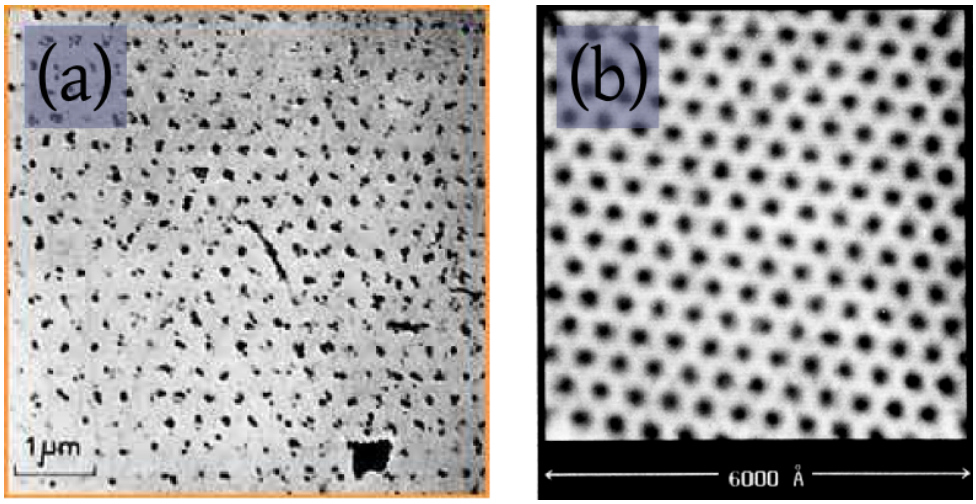

Figure 1.6: (a) First visualisation of a vortex lattice by Bitter decoration [22] in a lead-indium'4%) alloy. The vortex lattice is freezed in a field of 195G. (b) STM measurement of vortex lattice [23] in $NbSe_2$ at 1T. The color scale corresponds to the dI/dV values between $1 \times 10^{-8} \frac{1}{\Omega}$ (black) and $1.5 \times 10^{-9} \frac{1}{\Omega}$ (white).

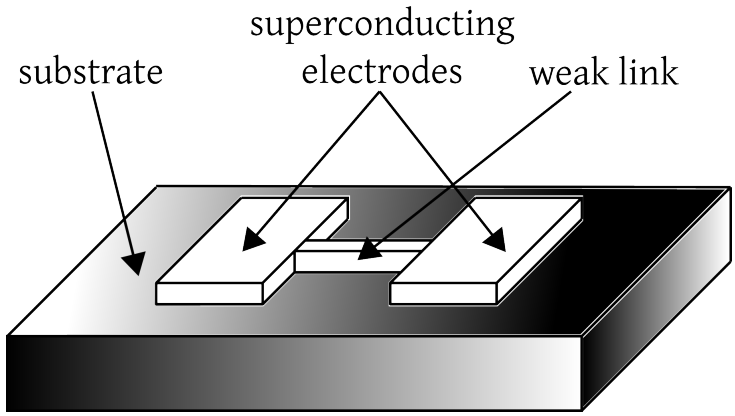

Figure 1.7: Schematic of a Josephson junction (weak link).

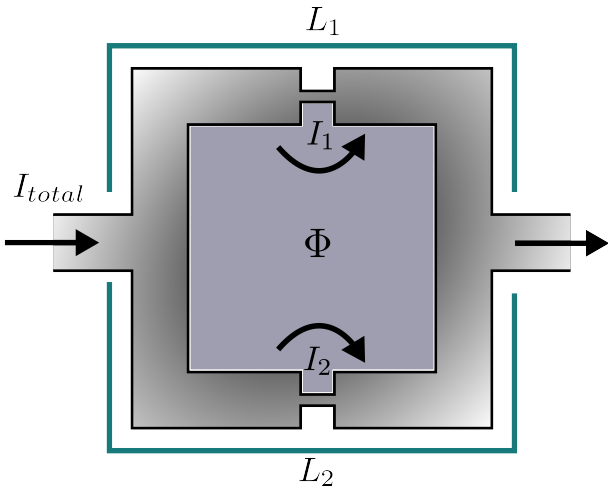

Figure 1.8: Illustration of a SQUID with two Josephson junctions. For details refer to the text.

1.3.7 Josephson effect

If two superconductors are put very close, so that their respective wave functions overlap, a coupling between them arises, leading to a current. In the BCS image, this can be explained by a non-zero probability for the Cooper pairs to tunnel from one side to the other. This was first described by Josephson in 1962 [24] (**Josephson dc-current**):

$$\mathbf{I} = I_0 \sin \varphi \tag{1.28}$$

with $\varphi = \varphi_2 - \varphi_1$ being the phase difference of the two superconductors.

The link between the two superconductors can be an insulating layer or a geometric obstruction, a so-called **weak link** (see figure 1.7). In the second case, equation 1.28 becomes non-sinusoidal, if the Josephson junction length becomes bigger than the coherence length ξ [25].

1.3.8 SQUID

In this section we give a brief introduction to direct current **s**uperconducting **qu**antum **i**nterference **d**evices (SQUIDs) based on [26]. A dc SQUID consists of two Josephson junctions as depicted in figure 1.8.

For an inductive SQUID with two weak links the following equations apply:

$$I_{total} = I_{c1}\sin\varphi_1 + I_{c2}\sin\varphi_2 = I_1 + I_2 \tag{1.29}$$
$$\Phi = \Phi_{ext} - L_1 I_1 + L_2 I_2 \tag{1.30}$$

The first equation simply states that the Josephson junctions are in parallel, the second that the flux inside the SQUID loop is modified by its own current.

Using equation 1.25, we obtain

$$\underbrace{\varphi_2 - \varphi_1}_{current\ term} + \frac{2\pi}{\Phi_0}(\Phi_{ext} + L_2 I_2 - L_1 I_1) = 2\pi n \tag{1.31}$$

where we added the Josephson current term.

Now, we can set $L = L_1 + L_2$ (notice that $L_1 \neq L_2$ in general). We consider both junctions to be identical: $I_{c1} = I_{c2} = I_{c0}$.

Plugging this into equation 1.31 yields

$$2\pi n = \varphi_2 - \varphi_1 + f + g\sin\varphi_2 - h(\sin\varphi_2 + \sin\varphi_1) \tag{1.32}$$

with $f = 2\pi\Phi_a/\Phi_0$, $g = 2\pi L I_{c0}/\Phi_0$ and $h = 2\pi L_1 I_{c0}/\Phi_0$. In the symmetric case we have $h/g = 1/2$.

In order to obtain the critical current equation 1.32 has to be solved for φ_1. Plugging the result into equation 1.29 and maximizing it yields I_c. The results for the symmetric case are depicted in figure 1.9.

By comparing the numerical results to experimental I_c over H curves of our SQUIDs (refer to chapter 2) we deduce a total inductance L of about 33 pH for a typical 1.1µm SQUID. For comparison, the geometrical inductance calculated by using $5\mu_0 C/16$ with C being the inner circumference of the SQUID is 1.57pF [27]. The total inductance has two contributions: the inductance of the loop and the inductance of the Josephson junctions. In our case the total inductance is governed by the latter as our weak links are narrow and thus the kinetic inductance contribution is dominating [28].

1.4 Relation with BCS Theory

Up to now, many aspects of SC have been solely explained by the existence of a macroscopic wave function. In order to understand its origin, a microscopic understanding of the underlying principles has to be developed. This was achieved in 1957 by Bardeen, Cooper and Schrieffer who presented a microscopic theory of superconductivity ([7] [8]) in which electron pairs (Cooper pairs [13]) play the role of the superconducting charge carrier. Cooper put forward a mechanism that explained this pairing: if two electrons are put onto the Fermi sea (at energy E_F) they will stay there, since all lower-energy states are already occupied. But if an attractive potential between the two electrons existed, they could go to lower energies, thus creating a **gap in the density of states**.

The existence of an energy gap in the excitation spectrum is indicated by the exponential behaviour of several macroscopic physical quantities, e.g. the specific heat and by the zero resistivity of a superconductor: In a normal metal electrons can transfer infinitesimal small energies to the lattice which leads to a finite resistance. In superconductors this transfer seems to be suppressed. Thus, it seems plausible that the electron energy spectrum in a superconductor is modified by a gap Δ. In the limit of conventional BCS theory this gap converges to $\Delta(T \to 0) = 1.76 k_B T_{SC}$.

An intuitive picture of the attractive phonon-interaction is given in [2]: We consider that electrons deform the lattice. The resulting positive charge density attracts other electrons which appear in

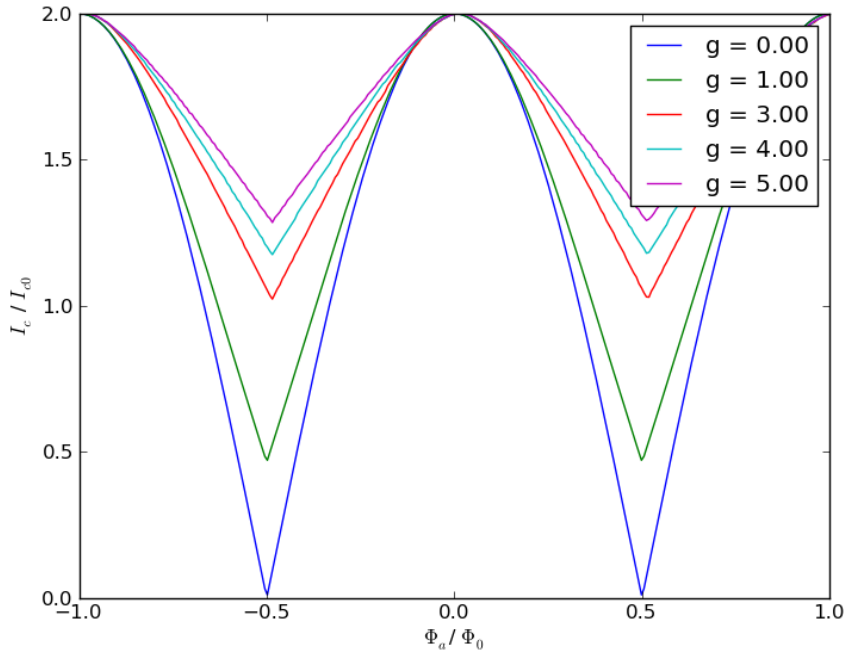

Figure 1.9: Results of the numerical calculations of the I_c over Φ characteristics for symmetric SQUIDs ($g = 2h$), identical junctions $I_{c1} = I_{c2} = I_{c0}$ and $g = 2\pi L I_{c0}/\Phi_0$. Maximal modulation is achieved for $g = 0$, when neglecting the inductance of the SQUID.

their trails. After the deformation, the positive charge density does not disappear instantly, but relaxes on a time scale of $\tau = 1/\omega_q$ (ω_q is the frequency of the lattice vibration). The first electron having caused the deformation will have travelled a distance $s = v_F \cdot \tau$ of 100 nm up to 1 µm (choosing $v_F \sim 10^6$ m/s and $\tau \sim 10^{-13}$ s $- 10^{-12}$ s). The **retarded interaction** is essential as it weakens the Coulomb repulsion.

Without going into details it should be mentioned that electrons forming a Cooper pair in BCS theory have opposite momenta and spins. The gap opens isotropically, therefore this kind of superconductor is called **s-wave** superconductor.

In 1959 Gor'kov showed that the GL theory can be derived from a constrained form of BCS theory that is well suited for the description of spatial variations [29].

1.4.1 Magnetic limits

Now, we want to briefly discuss the interplay between superconductivity and the magnetic field. In conventional superconductivity electrons with anti-parallel spins (singlet) and opposite momenta form a Cooper pair (s-wave superconductivity). Applying a magnetic field can destroy this singlet superconductivity by two effects: the orbital and the paramagnetic limit.

Orbital limit The applied magnetic field acts on the two electrons with opposite momenta by exerting the Lorentz force on each of them in opposite directions (see figure 1.10). As a consequence, these electrons are forced to move on circles with decreasing radii as the field increases. Once the radii become of the order of the coherence length, superconductivity is destroyed.

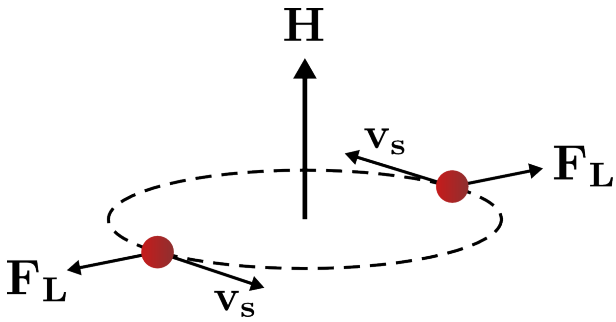

Figure 1.10: Illustration of the orbital effect: The Lorentz force breaks the Cooper pair. v_s denotes the superfluid velocity.

The critical field can be expressed as [30]:

$$H_{c2}^{orb}(T) = \frac{\Phi_0}{2\pi\xi^2(T)} \tag{1.33}$$

since ξ is proportional to $\frac{1}{m}$ (the mass m being dependent of the direction) the orbital limit is usually quite large for heavy fermion systems (see chapter 5).

Paramagnetic limit So far we did not consider any interaction between the applied field and the electron spin. It is clear that by increasing the applied field the energy of the anti-parallel aligned electron increases ($\sim \mu_B B$) until it is energetically favorable for the electron to spin-flip and to break the Cooper pair ($\sim \Delta$). In the zero temperature limit, the field at which spin-flip occurs, can be written as:

$$H_{c2}^{para}(T=0) = \frac{\sqrt{2}\Delta(T \to 0)}{g\mu_B} \tag{1.34}$$

with the Bohr magneton μ_B, the gyromagnetic factor for electrons g.

For $g = 2$ (free electron g-factor) this yields (in tesla for T_{SC} in kelvin):

$$H_{c2}^{para}(T=0) = 1.85 T_{SC} \tag{1.35}$$

In the case of unconventional superconductors with equal spin pairing states, this limit will not apply (see chapter 5).

2
Experimental setup

In the first part of this chapter I will explain the different sub-systems of the microscope, beginning with the SQUID and the AFM regulation. The last part is dedicated to the discussion of calibration and performance measurements.

2.1 Introduction

The microscope was planned to be used to image vortices in superconductors. Because the flux going through a superconducting vortex is $\Phi_0 = h/2e = 2.07 \times 10^{-15}$ Wb a high magnetic resolution is required, thus we chose to use a SQUID. Another reason to use a SQUID is that it can be fabricated relatively easily (compared to Hall-probes) and the fact that the read-out electronics existed already in the laboratory.

In order to scan a sample surface with a high spatial resolution the SQUID/sample distance has to be very small. This can be obtained by different means. We opted for the AFM technique with a tuning fork, as it is very stiff. This enables us to glue a SQUID-chip on top of it and to microbond the connections on the SQUID. A schematic of the microscope can be seen in figure 2.1:

At the bottom our custom z-motor, which is used for the coarse approach, is shown: Shear piezos in the interiour of a titanium block move a hexagonal slider up and down [31]. Inside the slider we integrated bimorph piezos moving the sample holder laterally beneath the SQUID during scanning.

Thus, in our design it is the sample that is moved beneath the SQUID during the approach and the imaging, the tuning fork with the SQUID glued on it are only moved in the z-direction in order to maintain a constant height above the surface of the sample. This movement in z-direction is obtained by a piezo stack changing its dimensions as a function of applied voltage and is used as an actuator in our regulation loop maintaining the SQUID/sample distance constant. Two attocube motors (slip-stick motors) are attached on top of the microscope moving up to 5 mm in x and y direction (i.e. laterally with respect to the sample). This allows for scanning different regions of the sample.

In order to access easily all components of the microscope, the 3 pillars are divided so that the microscope can be opened up. The top and bottom parts are depicted in figure 2.1.

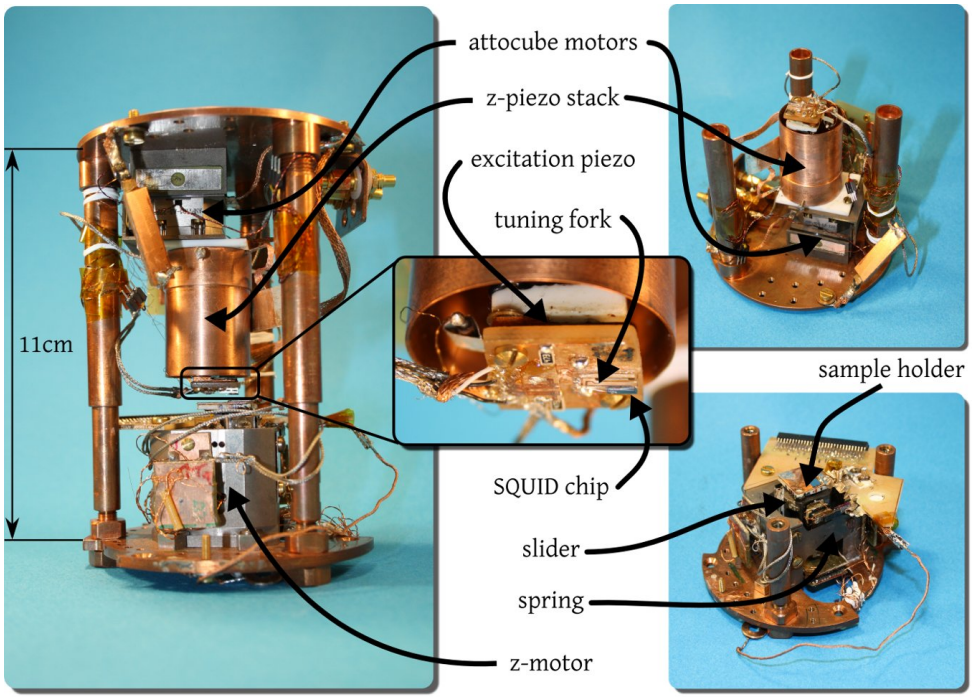

Figure 2.1: Photos of the microscope. Left: the completely assembled microscope, center: zoom of the tuning fork with the SQUID-chip underneath, right: the top part with the sensors (top) and the bottom part of the microscope with the sample holder (bottom).

2.2 SQUID

The crucial part of our microscope is the SQUID. The theoretical model has been already introduced in chapter 1, so the focus in this section the focus will be on its fabrication, the measurement of the critical current and the magnetic sensitivity.

2.3 Introduction

We use aluminum SQUIDs with a $T_{SC} \sim 1.2\,\mathrm{K}$. The SQUID geometry is a square with an inner circumference of 4 µm. The width of the SQUID arms is 200 nm which leads to an effective area of about 1.1 μm^2. A typical SQUID is depicted in figure 2.2.

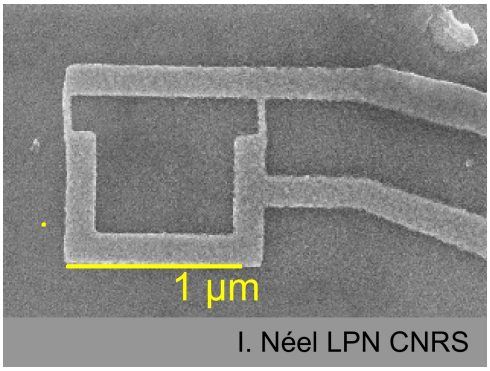

Figure 2.2: Image of a SQUID with an effective area of 1.2 μm^2. SQUID fabricated by D. Mailly (LPN, Paris).

2.3.1 Fabrication

The fabrication process of the SQUIDs using a lift-off procedure is illustrated in figure 2.3.

1. A silicon wafer is spincoated with PMMA[1].
2. An electron beam (scanning electron microscopy) is used to draw the SQUID on the PMMA and destroys its polymer chains on the exposed parts.
3. The development process removes the exposed PMMA and the silicon is uncovered. This results in a negative SQUID motif.
4. Thermal evoparation of a 30nm thin aluminum film.
5. PMMA lift-off in acetone.

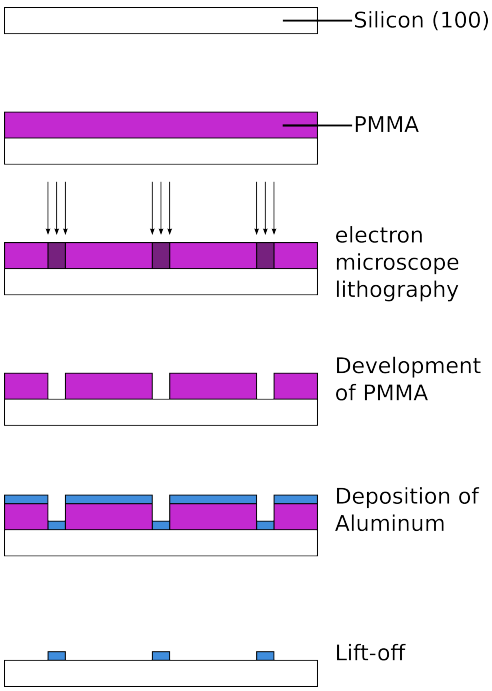

Figure 2.3: Schematics of the fabrication process. For details refer to text.

This procedure provides us with a wafer containing hundreds of SQUIDs. However, we need the SQUID to be close to the border of the wafer for the SQUID/sample distance to be as small as possible. This is obtained by cutting or etching the wafer around the SQUID.

We used two different techniques:

cutting: We let the wafer be cut with a diamand saw (a technique widely used in the semiconductor industry). Its precision is about $2-3$ µm, due to small unavoidable misalignements. This cutting is done by Y. Gamberini (Crolles) on wafers fabricated by D. Mailly (LPN). One SQUID-tip obtained by this technique is shown in figure 4.12.

The main advantage of this technique is its simplicity. The main drawbacks are the limited precision and the fact that only parallelogram geometries can be cut out.

deep reactive ion etching This technique (K. Schuster and A. Barbier, IRAM[2]) provides better control of the SQUID position and can be used for more complicated geometries allowing ultimately for shorter SQUID/sample distances. The SQUID wafer is fabricated at the Néel

[1] Poly(methyl methacrylate)
[2] Institut de Radioastronomie Millimétrique, Grenoble

institute by T. Crozes, who also made a mask in the shape of a tip protecting the SQUIDs from the etching process. The resulting SQUID-tips are depicted in figure 2.4.

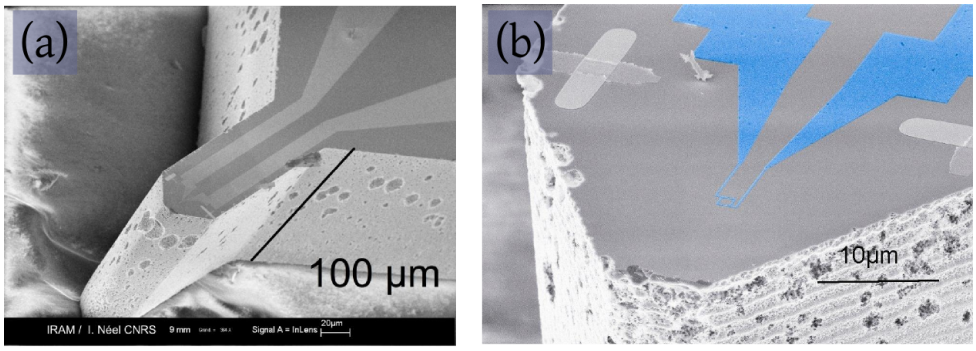

Figure 2.4: (a) Electron microscope image of the SQUID chip geometry obtained by etching. Etching by A.Barbier at IRAM. (b) Zoom: the SQUID can be positioned very close to the edge to obtain a small SQUID/sample distance. SQUID made by T. Crozes

2.3.2 Measurement of the critical current

The fabrication process of our SQUIDs is very simple (only one aluminum layer) and SQUIDs can be mass-produced (between 100 and several hundreds per wafer, depending on the technique). In comparison to Hall probes or other SQUID designs (see next chapter) this simplicity is the most important advantage of our fabrication process compared to Hall probe fabrication, especially when considering its use as a scanning sensor which breaks easily. However, a more complicated read-out electronics is needed, as no feedback mechanism can be used in order to measure the magnetic flux penetrating through the SQUID loop directly.

This stems from the fact that our SQUID is thermally hysteretic [32]: The junctions transit into the resistive state once the bias current exceeds the critical current. The electron temperature increases after the transition because of the thermal resistance of the junction heating the metal. In order to bring the system back into the SC state the bias current has to fall below the so-called retrapping current (significantly smaller than the critical current). Figure 2.5 shows this hysteretic behaviour for an S-N-S junction (top: electron temperature; bottom: V over I).

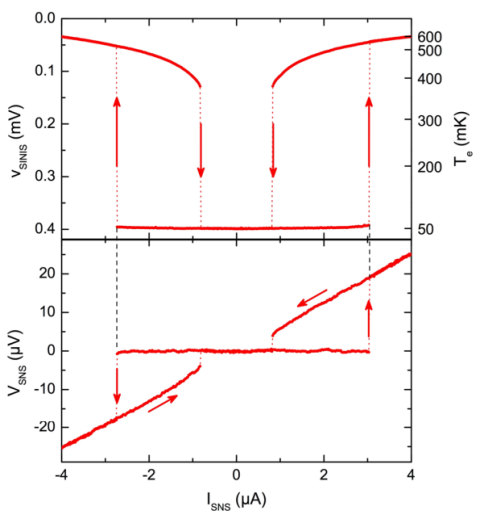

Figure 2.5: Current-voltage characteristic of an S-N-S junction (bottom). The electron temperature was measured simultaneously (top). The cryostat temperature is 50mK, from: [32].

A feedback not only increases the sensitivity of the SQUID by making it possible to measure continuously, but it also provides a way to measure the magnetic flux through the SQUID loop in a linear manner, in contrast to critical current measurements that modulate with the flux, resulting in the same critical current for different fields. We will see in the last chapter that the latter makes it harder to interpret images of samples with a high magnetic signal.

In the scope of SuperNanoCharac[3] an effort is underway in order to make non-hysteretic microbridge SQUIDs with a feedback.

For the time being, we use our one-layer Al-SQUIDs in combination with sophisticated electronics (40 MHz clock) to measure the critical current: We apply a bias current ramp and detect when the critical current is exceeded. This transition is detected by a sudden change of the dV/dI slope above a user-defined threshold using a comparator. Once this happens the current is cut to zero within 40 ns. The critical current is deduced by measuring the duration of the current ramp (see figure 2.6).

To improve the temporal resolution and to minimize the measurement time, we start the current ramp at a value close to I_c.

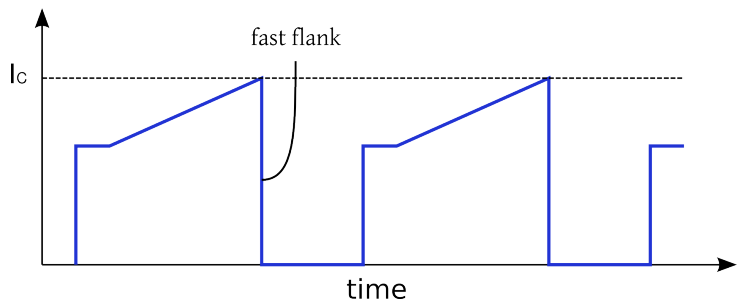

Figure 2.6: A current ramp is used to determine the critical current of the SQUID. The repetition rate is of the order of 600 Hz.

2.3.3 Characterisation

Now, we will discuss the magnetic sensitivity of the SQUID used during this thesis.

In figure 2.7 an experimental characteristics (I_c over H_{app} curve) of a 1.1 µm SQUID is depicted. The ordinate shows the time it takes for a given ramp to reach the critical current. The time is measured in bits. 2^{16} bits correspond to one cycle of 1.5 ms. The minimum and maximum critical current are 50 µA and 80 µA, respectively. At each field 30 measurements of the critical current are taken. With these 30 measurements we can thus deduce the **average standard deviation** for each field. The average standard deviation over a whole period of the characteristic is $\sigma = 120$ bits. The average slope of the characteristics can be taken as $\bar{m} = 2 \cdot 20000$ bits / 16.8G = 2380 bits/G, the steepest slope corresponds to $m_{max} = 5100$ bits/G.

The **uncertainty per measurement** in units of gauss can be deduced from these slopes and σ by σ/m:

$$\sigma/\bar{m} = 0.05\text{G} \tag{2.1}$$

$$\sigma/m_{max} = 0.024\text{G} \tag{2.2}$$

$$\tag{2.3}$$

As expected the uncertainty is the smallest at the steepest slopes of the I_c vs. H_{app} curve. When imaging the magnetic field distribution we usually take **30 measurements per pixel** (at a **sampling**

[3] ongoing project supported by the NanoScience Foundation (Grenoble, France), for more details see section 2.17

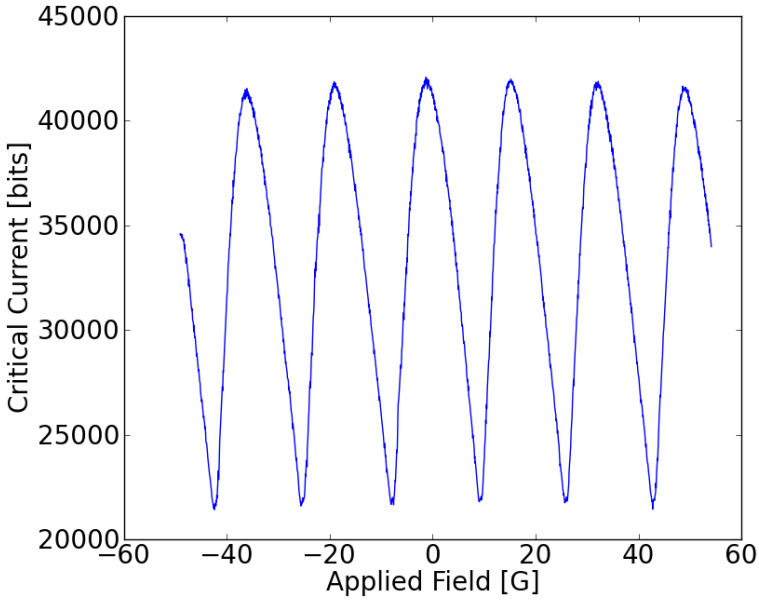

Figure 2.7: A typical critical current vs. applied field curve. For this plot we used the raw data of the SQUID measurement. The period is 16.8G.

rate of 600 Hz) this leads to an average sensibility of:

$$\bar{\sigma}_{pixel} = 9 \times 10^{-3}\mathrm{G/px} = 5.4 \times 10^{-4}\Phi_0/\mathrm{px} \tag{2.4}$$

$$\bar{\sigma}_{sec} = \sigma/\bar{m}\frac{1}{\sqrt{600}} = 2 \times 10^{-3}\mathrm{G}/\sqrt{\mathrm{Hz}} = 1.2 \times 10^{-4}\Phi_0/\sqrt{\mathrm{Hz}} \tag{2.5}$$

$$\tag{2.6}$$

We have characterized two 1.1 micron SQUIDs and two 0.6 micron SQUIDs. The results are summarized in table 2.1

Table 2.1: The noise levels of four of our weak link μ-SQUIDs.

SQUID size (effective diameter) [μm]	noise [$\Phi_0/\sqrt{\mathrm{Hz}} \times 10^{-4}$]
1.1	1.2
1.1	3.0
0.6	2.1
0.6	1.1

It is interesting to notice that the noise level does not depend on the effective area. The period of the 1.1 micron SQUIDs is 16.8G, while the period of the 0.6 micron SQUIDs is 54G, corresponding to their geometrical dimensions. In other words, the smaller the SQUID and the penetrating flux, the smaller the resulting signal is.

2.3.4 Noise estimation

The following calculation leading to an estimate of the SQUID's noise is based on [33].

The SQUID energy E can be written as

$$E = \frac{1}{2} L I^2 \tag{2.7}$$

with $L = 33$pH being the inductance of the SQUID. Using $\Phi = LI$ this can be rewritten as:

$$E = \frac{1}{2} \frac{\Phi^2}{L} \tag{2.8}$$

The minimal energy variation ΔE in the time interval Δt is thus equal to the flux noise power multiplied by $2L$:

$$\Delta(\Phi^2) = S_\Phi^2 = 2L\Delta E = 2L\hbar/\Delta t = 2L\hbar f \tag{2.9}$$

with f being the bandwidth. In order to get from the second term to the third, we used the Heisenberg uncertainty principle $\Delta E \Delta t = \hbar$, since quantum physics limits the sensitivity of the SQUID.

The flux spectral noise density is thus given by:

$$S_\Phi = \sqrt{2L\hbar}/\sqrt{\mathrm{Hz}} \tag{2.10}$$

In order to achieve this sensitivity we would have to be capable of measuring the critical current at the frequency characterizing the quantum phenomena, the Josephson frequency f_J. As our sampling frequency f_s is 600Hz, the sensitivity of the SQUID is therefore reduced by a factor of $\sqrt{\frac{f_J}{f_s}}$:

$$S_\Phi = \sqrt{\frac{f_J}{f_s}} \sqrt{2L\hbar}/\sqrt{\mathrm{Hz}} \tag{2.11}$$

To determine the Josephson frequency $f_J = V/\Phi_0$, we have to know the voltage at the SQUID junctions at the moment of the transition. Calculating the resistance of the microbridges $R = \rho_{Al} L/A$ (L=200 nm being the length, $A = 40\,\mathrm{nm} \cdot 30\,\mathrm{nm}$ the cross-section and $\rho_{Al} = 1.64 \cdot 10^{-8}\,\Omega\mathrm{m}$) and taking a critical current of 65 µA yields a Josephson frequency of ~ 90 GHz. Plugging this frequency into equation 2.11 leads to a sensibility of the SQUID of the order of $5 \cdot 10^{-4} \Phi_0/\sqrt{\mathrm{Hz}}$. This is in good agreement with the experimental results.

In this simple treatment we have neglected other noise contributions (thermal, shot noise).

2.4 AFM

2.4.1 Introduction

In 1981 scanning tunneling microscopy was invented by Binnig and Rohrer [34]. Atomic resolution was demonstrated by observing the structure of the Si(111)-(7x7) surface [35]. Only five years later, Binnig and collaborators introduced the atomic force microscopy [36]. With this scanning microscope it was possible to scan non-conductive surfaces. Atomic resolution was first achieved in 1991 by Giessibl (see ref. [37], [38]).

The force between tip and sample is measured with a “spring“: Cantilevers are only sensitive to normal forces (w.r.t. the sample surface). Their deflection (proportional to the tip/sample force) was used at the beginning for static contact modes [38]. The first cantilevers were very simple: gold foils with a small diamond tip [36] or aluminum foils [39]. Micromachined tips were fabricated from 1990 on (see ref. [40] and [41]).

The deflection of these cantilevers is usually determined by measuring the deviation of a reflected laser beam by means of photo-diodes. In the case of the first atomic force microscope an STM-like

design on the backside of the cantilever was used to determine the deflection [36]. Nowadays, for experimental convenience piezo-resistive [42] or piezo-electric cantilevers have been developed to determine the deflection.

Several operation modes are possible: In the beginning **static modes** have been used to control the sample/tip distance: an actuator compensates for changes in the deflection, maintaining it constant. Each pixel of the resulting image corresponds to a height (at constant deflection). Sensitive cantilevers are quite soft (of the order of 1 N/m). As a consequence, problems like jump-to-contact of the tip to the sample arise.

In the **dynamic modes**, the cantilever is mechanically excited. The experimentally simplest dynamic mode is the *amplitude modulation-AFM* (AM-AFM) [43]. The excitation actuator is driven at constant amplitude at a fixed frequency. By interacting with the sample surface the amplitude of the cantilever changes. Using the amplitude in a feedback loop allows for the tip/sample distance to be maintained constant. The drawback of the AM-AFM is that the response time (change in amplitude) of the cantilever is of the order of $\tau_{AM} = 2Q/f_0$ [44] (where Q denotes the quality factor of the cantilever). The quality factor can become very large in vacuum and low temperatures (several 10000) leading to slow scanning speeds.

By using a *frequency modulation mode* (FM-AFM) this problem can be overcome since the change of resonance frequency occurs within $\tau_{FM} = 1/f_0$. This is the mode we opted for for our microscope.

In 1995, Karrai and Grober introduced **quartz tuning forks** for scanning optical near-field microscopy [45]. Tuning forks have several advantages over standard cantilevers:

piezo-electric the deflection/oscillations of quartz tuning forks can be easily measured due to the piezo-electricity of quartz. This simplifies the experimental setup. Compared to piezo-resistive cantilevers piezo-electric ones dissipate less heat and are thus better adapted to low temperature experiments.

frequency stability the resonance frequency is very stable over time in a large temperature range. This is essential for the primary use of the tuning forks in watches. It is also very important for scanning microscopy as these drifts are a major noise factor in silicon cantilever devices [44].

mechanical stiffness we use the tuning fork as a force sensor and glue a SQUID chip on top of it. The SQUID has to be microbonded. The microbonding is only possible because of the stiffness of the tuning fork. Due to this high spring constant jump-to-contact problems do not occur in the case of a tuning fork[4].

ease of use the dimensions of a tuning fork are such that it can be handled easily with a tweezer, in contrast to a cantilevers which have to be handled with micro-tweezers.

2.4.2 Modelisation

In this section we will describe a very simple linear model for the tip-sample interaction. In this model the tip is replaced by a vertically oscillating point mass connected to a spring [47].

For an oscillating point mass interacting[5] with the sample surface (see figure 2.8(a)) we obtain the following equation of motion:

$$m^*\ddot{z} + c\dot{z} + kz = \underbrace{f\cos\omega t}_{excitation} + \underbrace{F(D+z)}_{interaction} \tag{2.12}$$

[4] another solution to avoid jump-to-contact is to use large oscillation amplitudes of a cantilever (see [46] for details)

[5] different kinds of attractive or repulsive forces exist. Exemplarily we mention two of them: chemical forces (short-range) and van der Waals (long-range forces). See ref [48] for more details on this matter.

with m^* being the effective mass (in the model: mass of the oscillator), c the friction coefficient, k the Hooke's constant, f the amplitude of the oscillations, ω the excitation's angular frequency, F the interaction force between tip and sample and D their mean distance.

This equation can be rewritten as:

$$\ddot{z} + 2\gamma\dot{z} + \omega_\infty^2 z = \frac{f}{m^*}\cos\omega t + \frac{F(D+z)}{m^*} \tag{2.13}$$

with γ being the damping, $\omega_\infty = \sqrt{\frac{k}{m^*}}$ the oscillator's angular frequency far away from the surface (without interaction).

Under the assumption of a weak tip-sample interaction, we can develop the interaction term to first order and yield:

$$\ddot{z} + 2\gamma\dot{z} + \omega_\infty^2 z = \frac{f}{m^*}\cos\omega t + \frac{F(D)}{m^*} + \frac{1}{m^*}\frac{\partial F(D)}{\partial z} z \tag{2.14}$$

with $\frac{\partial F(D)}{\partial z}$ being the force gradient at the oscillator's mean position. By subtracting the gradient term we obtain:

$$\ddot{z} + 2\gamma\dot{z} + \underbrace{\left[\omega_\infty^2 - \frac{1}{m^*}\frac{\partial F(D)}{\partial z}\right]}_{\omega_0^2} z = \frac{f}{m^*}\cos\omega t + \frac{F(D)}{m^*} \tag{2.15}$$

This new term can be interpreted as a new spring between the sample and the oscillator with the following Hooke's constant:

$$k_{pot} = -\frac{\partial F(D)}{\partial z} \tag{2.16}$$

For attractive interaction forces the resonance frequency decreases and for repulsive interactions it increases:

$$\omega_0 = \omega_\infty\sqrt{1 - \frac{1}{k}\frac{\partial F(D)}{\partial z}} \approx \omega_\infty\left[1 - \frac{1}{2k}\frac{\partial F(D)}{\partial z}\right] \tag{2.17}$$

The potential near the surface of the sample can be described by the Lennard-Jones potential:

$$V_{LJ} = -E_{bond}(2\frac{\sigma^6}{z^6} - \frac{\sigma^{12}}{z^{12}}) \tag{2.18}$$

the first term corresponds to the attractive van der Waals interaction [49], the second term is repulsive.

As a consequence the frequency shift has different signs for the two different regimes. This makes a traditional AFM regulation difficult as it is only stable on one branch of the potential. Refer to section 2.16.1 for experimental results for our tip.

2.4.3 Tuning fork properties

The geometry and dimensions of our tuning fork is depicted in figure 2.8(b). With these values the spring constant k (see Ref. [50] for details) can be determined:

$$k = \frac{E}{4}W\left(\frac{T}{L}\right)^3 \tag{2.19}$$

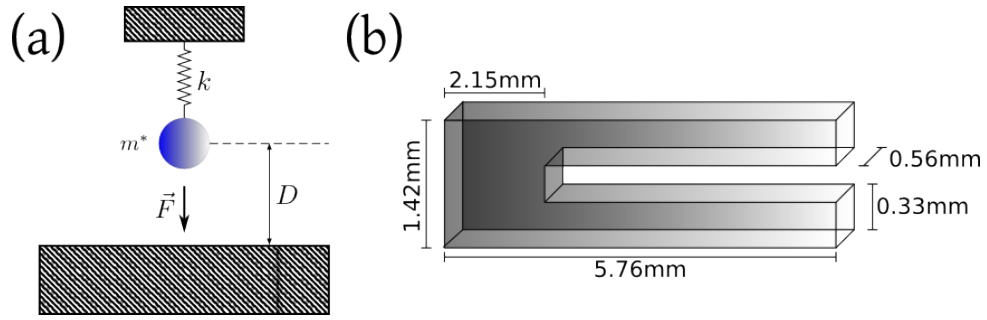

Figure 2.8: (a) Illustration of the tip/sample interaction. Refer to the text for details. (b) the tuning fork geometry and dimensions.

E stands for the Young's modulus (for quartz: $E = 7.87 \times 10^{10} \frac{\mathrm{N}}{\mathrm{m}^2}$). This yields (for our dimensions) $k = 25500 \frac{\mathrm{N}}{\mathrm{m}}$.

When the tuning fork is bent, surface charges are generated in the piezo-electric quartz. When the tuning fork oscillates these ac-currents can be collected by electrodes on the tuning fork surface. We use a custom current-voltage amplifier with a very high gain ($\sim 10^6$V/A) to probe the oscillation of the tuning fork. The signal's frequency and phase with respect to the excitation are used for the AFM regulation.

Following reference [50] the sensitivity of the tuning fork can be estimated as 0.4 nm/nA.

2.5 Tuning fork resonance frequency

The tuning fork[6] in its housing (its original state) has a resonance frequency of $2^{15} = 32768$ Hz with a quality factor of several 10000.

Once the housing and thus the vacuum is broken, the resonance frequency and quality factor drop due to the friction with the surrounding air.

To use the tuning fork in the our microscope we glue one prong on a PCB board. The broken symmetry and losses in the glue bring down the quality factor even further. This configuration with one fixed and one free prong is referred to as *Q-Plus* in literature. Exciting the tuning fork mechanically leads to a harmonic behaviour which can be described by a lorentzian peak for the amplitude and a monotonic variation of the phase between the excitation and the reponse of the tuning fork. The response is asymmetric in the case of electrical excitation [51] because of the capacitive current associated with the electrodes of the tuning fork. In order to compensate for this, one needs a more complicated electrical setup (see [52], [53]). Therefore, we opted for the mechanical excitation.

The last step is glueing the SQUID chip on top of the free prong. This naturally increases the effective mass of our oscillator and decrease the eigen-frequency. By choosing the position of the SQUID chip, one can adjust the resonance frequency.

To connect the SQUID electrically we use a bonding machine that bonds a thin aluminum wire (25μm) to the SQUID pads by using ultrasound vibrations. If the resonance frequency of the tuning fork is close to the ultrasound frequency or multiples of it, the bonding does not work, thus we have to put paper in between the two prongs to avoid vibrations.

In table 2.2 the different configurations and their properties at room temperature are summarized.

[6] Bürklin 78D202

Table 2.2: Different tuning fork (TF) configurations and their corresponding resonance frequencies and quality factors. All measurements done at room temperature.

configuration	resonance frequency [Hz]	quality factor
TF in housing	32768	36410
free TF	32760	7620
free TF + SQUID	28826	115
one glued prong	31948	177
one glued prong + SQUID chip	23455	67

2.6 Thermal behaviour of the frequency spectrum

As we cool down the tuning fork, the glue and the quartz itself becomes stiffer, increasing the resonance frequency. At the same time the quality factor increases to ~ 1000 at 4 K, and several thousand at 0.2 K. The spectra for different temperatures are shown in figure 2.9.

The spectra can look much more complicated with multiple peaks, peaks that shift to lower frequencies with decreasing temperature and peaks that appear and disappear during the cooldown. The spectra can also change between different cooldowns.

This complex behaviour is due to the glassy properties of the glue (Araldite) whose quality factor changes non-monotonically with temperature. When warming the glue up and cooling it down again (during an approach), this can lead to a relaxation of the glue changing the resonance frequency.

In general, it is considered best to use only tuning forks with a good spectrum (one isolated sharp peak) at room temperatures and to use as little glue as possible to obtain good excitation transmission.

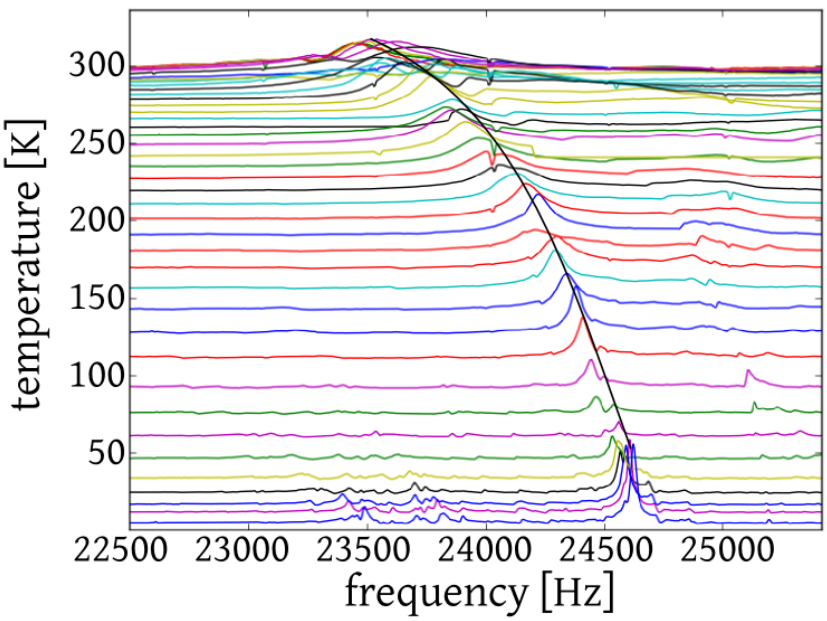

Figure 2.9: Tuning fork spectra taken at different temperatures. As we cool down, the glue and the quartz of the tuning fork become stiffer, increasing the resonance frequency. The black line is a guide to the eye.

2.7 Regulation

2.7.1 Z-Actuator

The distance between the SQUID and the sample is controlled by the tuning fork's resonance frequency change. The resonance frequency is obtained by using a regulation to maintain the phase constant (phase locked loop). The resonance frequency is fed into another electronic regulation that controls the voltage of a piezo-electric z-stack[7] (out of PZT-5A) that either elongates or shortens. This z-stack is attached below the attocube motors. Its length is 3.6 cm and its piezo-electrical expansion coefficient is 0.32 µm/V at room temperature. This equates to a maximal elongation of 35.2 µm at 110 V.

2.7.2 Regulation

The key component of the microscope and in particular its electronics is the regulation that keeps the tuning fork at a constant distance from the sample surface. This is depicted in figure 2.10:

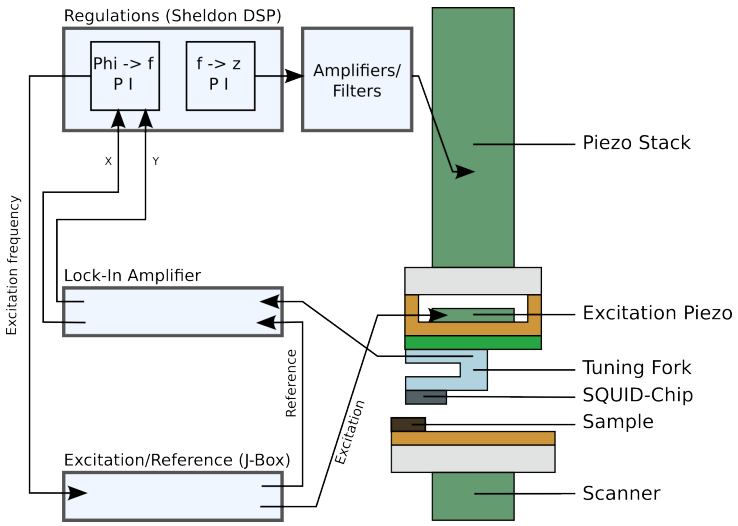

Figure 2.10: Schematics of the regulation loops: The tuning fork is excited by a piezo actuator. As we approach the surface its resonance frequency changes. This is compensated by a piezo stack keeping the tip/sample distance constant.

Preparation: Before starting the regulation, we perform a frequency sweep to establish a frequency spectrum. Then we choose a frequency range containing a peak and a smooth, monotonic phase dependency. We choose a set phase (reference) inside this range (typically at about 40%-60% of the interval). Up to now, we only setup the resonance frequency regulation. Since there was no interaction with the sample surface, we are at the resonance frequency f_∞ (far away from sample). To control the z-piezo stack, a set frequency f_{set} is required. Typically $\Delta f = f_{set} - f_\infty$ between 1 Hz and 3 Hz.

Compared to ordinary STM measurements Δf is rather large: In STM measurements a value of about 100mHz is typically used. This has several reasons:

First, our SQUID chip is not comparable with an AFM tip (with a small apex). Second, our tuning fork resonances are much broader due to the fact that one prong is fixed and that the SQUID chip is heavier than a STM tip.

[7]Manufacturer: Piezo Ceramic, Model: P-885.90

Regulation: Once all these initial values are set, the z-piezo stack extends, while the resonance frequency is measured by regulating the phase. As soon as the current resonance frequency f is at f_{set} the approach stops and the system stabilizes.

The two cascading proportional-integral controllers (PI) (for the resonance frequency and for the distance control) are implemented on a digital signal processor (DSP)[8] performing 15625 cycles per second. The sampling rate of the signal is increased to 125 kHz by multiplexing 8 channels.

For the **frequency regulation** the DSP communicates by means of 9 digital I/0 ports (one for message notification, eight for the command and the data) with a FPGA[9] in the J-Box (see figure 2.21). The FPGA passes the new frequency to two DDS (Digital Data Synthesizer) connected to the excitation piezo and the reference input of the lock-in amplifier, respectively.

The response of the tuning fork is phase shifted. This phase shift is picked up by the lock-in amplifier[10] which outputs X and Y by means of its DACs. The time constant of the lock-in amplifier is set to 100 µs. This means that the DAC output is averaged over ~ 3 oscillations of the tuning fork. X and Y are used to calculate the phase before feeding it into the resonance frequency regulation. This closes the first regulation loop.

The second PI controller, responsible for the **distance regulation**, uses the resonance frequency as its input, compares it to f_{set} and controls the z-piezo-voltage (by a DAC) accordingly. As the capacity of the z-piezo-stack is rather high (3.3μF) the charge needed to change its voltage are as well rather high and can heat up the microscope. Consequently, a compromise has to be made: fast regulation, but no big responses. The ideal parameters depend on the scanned surface.

2.8 Scanner

2.8.1 Introduction

The inner part (slider) of the z-motor can be propelled up and down by shear piezo elements. Inside the slider there are four bimorph piezo elements[11] (see figure 2.11). Two of those are glued to the slider and a floating platform. The other two are glued to the platform and the sample holder. By this "folding" we can move the sample in x and y-direction. The floating platform and the sample holder are made of Macor that has a similar thermal expansion coefficient as the piezo-electric ceramics (PZT-5A) the piezos are made of. The scanner is based on designs from J. Siegel (see [54]).

One can move the sample beneath the SQUID during a scan by applying a voltage to the bimorph piezo elements as shown in figure 2.13(a): Each half of the piezo bends in different directions so that the upper part moves laterally with respect to the lower part. Notice that both ends by and large stay parallel to the initial state.

The piezo elements are 31.8 mm long, 6.4 mm wide and 0.5 mm thick. In order to estimate the scan range we used

$$x_{max} = d_{31} V \frac{L^2}{T^2} \tag{2.20}$$

with L, V and T being the voltage, thickness and length, respectively. When plugging in the coefficient d_{31} from the data sheet this yields a free deflection of 200 µm.

[8] Sheldon Instruments PLX-based SI-C6713 DSP card
[9] Altera ACEX1k
[10] Signal Recovery 7280 (main ADC sampling rate of 7.5MHz)
[11] Manufacturer: Piezo Systems, Model: T220-A4-203X

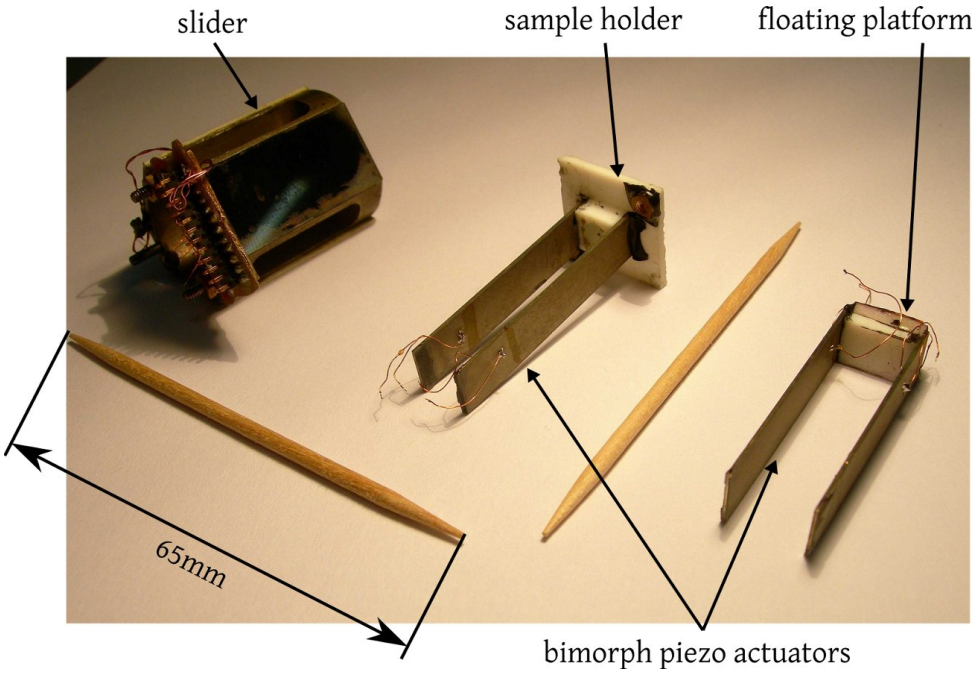

Figure 2.11: Photograph of the scanner consisting of four bimorph piezo-elements, the sample holder and the slider moved by the z-motor (not depicted).

2.8.2 Deviation from plane

When the bimorph piezo elements of the scanner are bent to move the sample, they also change the z-position of the sample, because of their finite length $l = 31.8mm$. For future developments it is interesting to calculate this drop Δz as a function of the deflection d. $2d$ corresponds to the full scan range.

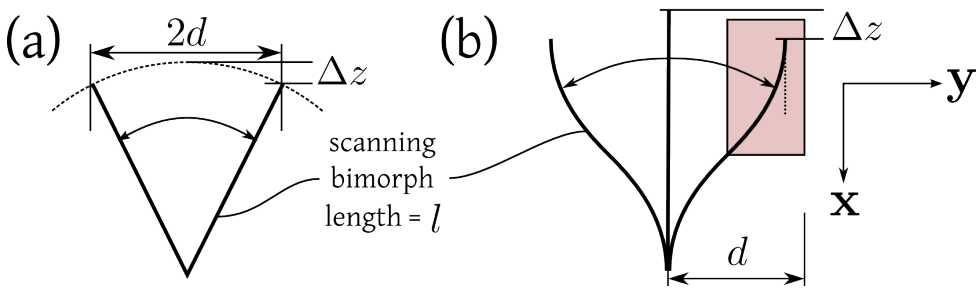

Figure 2.12: Schematics of the two models used to calculate the drop Δz during scan: (a) circle model, (b) polynomial model (only one half of the bimorph is used for the calculation). Refer to text for details.

Simple Model In a first model (see figure 2.12(a)) we consider a piezo element that is fixed at one end and moves at the other end in a circular manner. In this case we obtain:

$$\sqrt{l^2 - d^2} - l = \Delta z \tag{2.21}$$

Polynomial Model: In an improved model (see figure 2.12(b)) we also consider the shape of the bent piezo element and model it with:

$$y(x) = \frac{d}{2} - ax^2 \tag{2.22}$$

with $a > 0$. This equation models only one half of the piezo element. However this is sufficient due to symmetry considerations (see figure 2.12(b)).

This polynomial model takes also into account that the both ends of the piezo element are glued such that their respective slopes (dy/dx) vanishes.

The root n of the polynomial is:

$$n = \sqrt{\frac{d}{2a}} \tag{2.23}$$

The length of a function is given by:

$$L\{f(x)\} = \int \sqrt{dx^2 + dy^2} = \int dx \sqrt{1 + f'(x)^2} \tag{2.24}$$

consequently:

$$L\{f(x)\} = \int \sqrt{1 + 4a^2x^2} \stackrel{!}{=} \frac{l}{2} \tag{2.25}$$

This leads to

$$L\{f(x)\} = \left[\frac{\operatorname{asinh}(2ax)}{4a} + \frac{1}{2}x\sqrt{4a^2x^2 + 1} \right]_0^n \tag{2.26}$$

and by simplifying and plugging in n we have to solve the following equation:

$$\frac{1}{2a}\operatorname{asinh}(\sqrt{2ad}) + \sqrt{d^2 + \frac{d}{2a}} = l \tag{2.27}$$

This equation has to be solved numerically to obtain Δz as a functioin of the deflection.

Results and discussion The resulting Δz as a function of the deflection is given in figure 2.13(b) for both models. As one can see the maximal drop is $\sim 0.2\mu$m for a deflection of $\pm 42.5\mu$m and thus clearly within the range of our piezo stack.

2.9 Imaging

We have chosen the scanning scheme depicted in figure 2.14(a): We scan columns back and forth before going to the next line. This scheme was chosen to minimize heat built-up instead of a scheme in which the tip is lifted at the end of each line and returns quickly to the initial position.

The orientation of the SQUID compared to the scanning direction is as well shown in figure 2.14(a). As the scanning direction is parallel to the SQUID tip the probability of breaking the SQUID is decreased, when scanning from north to south.

To understand this better, we show the movement of the SQUID tip on a patterned sample schematically in figure 2.14(b): When scanning from north to south the regulation is smooth, as either the tip of the SQUID chip or other parts of it are touching the closest point of the surface, whereas when

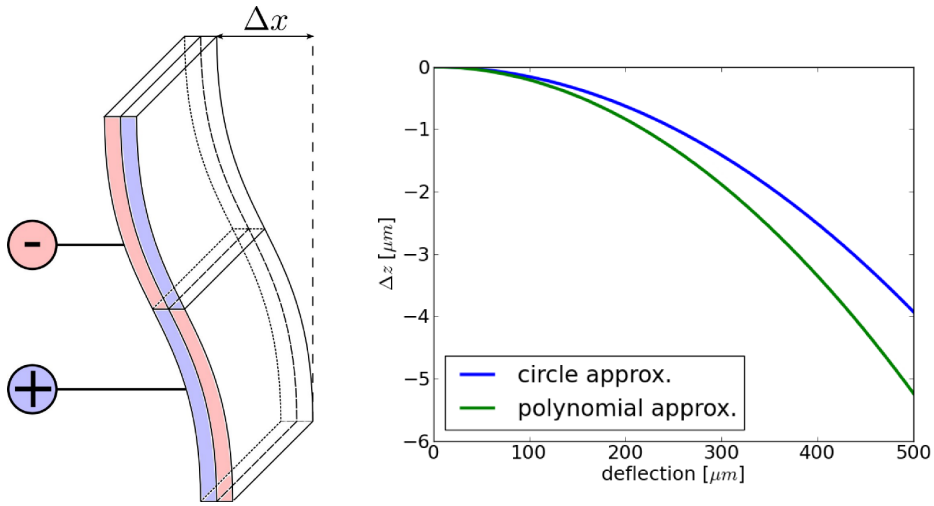

Figure 2.13: Left: Schematics of one bimorph used in the scanner. By applying a voltage the two halves curve in different direction thus moving the non-fixed upper part. Right: Comparison of the two approximations described in the text. The polynomial approximation of the vertical scanner movement is a more realistic model than the circular one. For both models the height drop is much smaller than the z-range of the z-stack actuator.

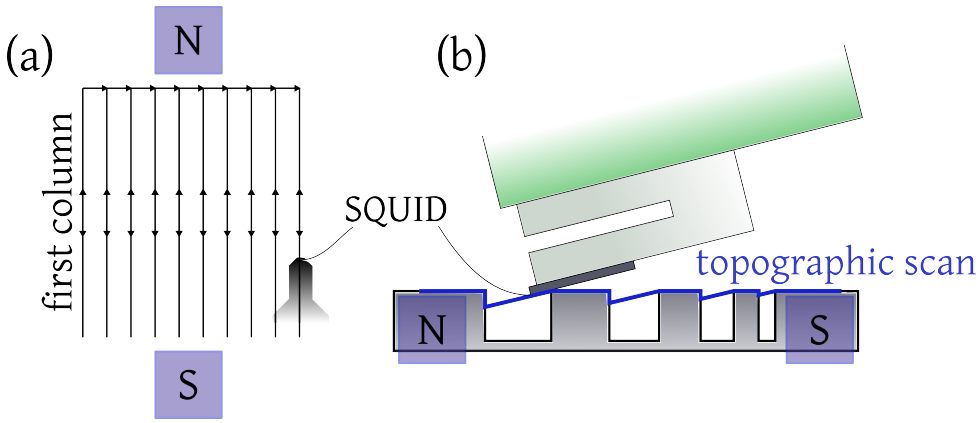

Figure 2.14: Left: Schematics of the scanning procedure. The high resolution scanning axis is in the direction of the SQUID tip. Right: The effect of an asymmetric tip is illustrated. Falling flanks can be followed whereas the slope of the tip itself makes a fast retracting impossible for rising flanks.

going from south to north the tip can be deep in a hole and crash the tip against a sudden flank. As a consequence samples with sharp borders (like cut out crystals) should only be scanned at the northern boundary. On the south side the SQUID tip easily breaks.

The information obtained by imaging is twofold: we save a topographic and a magnetic image. The former can be used to obtain magnetic images at different tip/sample heights by using the topographic image and adding a user-defined offset to this image while the AFM regulation is turned off. We call this the **fly over imaging mode**.

2.10 Coarse Positioning

In this section I will focus on the motors that are used either for approaching the sample and the SQUID, or for lateral movements in the millimeter range. The latter can be used to scan different

spots on a sample surface and/or find the sample in the first place. Naturally, we center the SQUID above the sample at room temperatures, but due to different thermal expansion coefficients and the geometry of the microscope it can happen - for small samples - that we will not be above the sample at low temperatures.

2.10.1 Coarse lateral positioning

For lateral movements with respect to the sample we use attocube-motors[12]. These are controlled via the corresponding Controller[13]. These motors are slip-stick motors that take advantage of inertia (see figure 2.15):

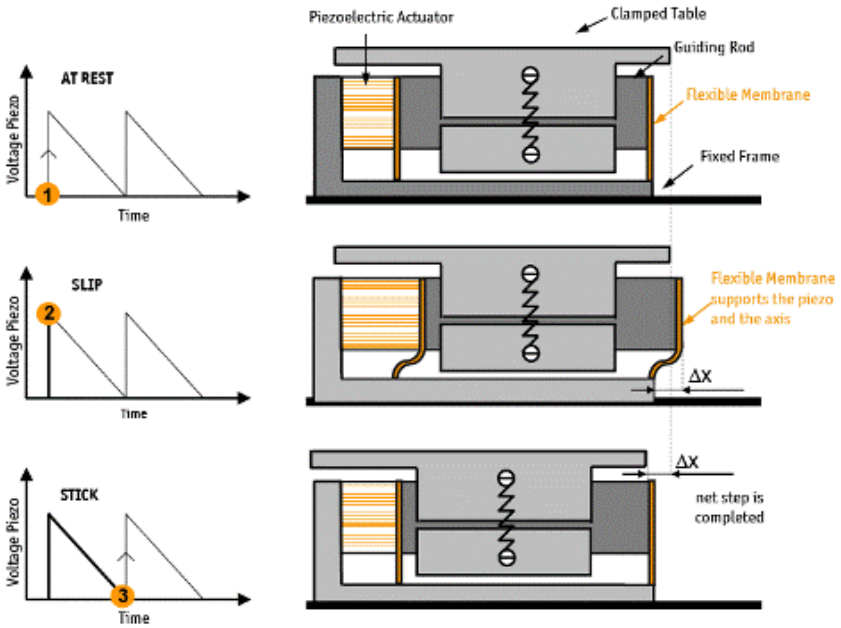

Figure 2.15: Working principle of slip-stick piezo motors, from: *attocube website*.

- **static friction:** One applies a slowly rising voltage at the piezo element inside the motor. This elongates and pulls one part (the slider) with it.
- **inertia:** In a second step the voltage jumps quickly to the initial state, thus shortening the piezo element. Because of the slider's inertia, it is left behind and has travelled a small distance during this cycle in respect to the piezo element.

The two step cycle is repeated until the designated position is attained. As described above the applied voltage is sawtooth-shaped. Changing the sign of this voltage, changes the direction. The Controller can deliver up to 70 V. (70 V should only be used at low temperatures, at room temperature 25 V should not be exceeded). The range of these motors is up to 5 mm. The motors are thermalised by putting thin silver foils with grease (thickness of 0.03 mm) in between the top motor and the copper plate and between the motors. The silver foils are connected to the thermal reference on the cryostat, either the mixing chamber or the still.

[12] AN-Pxyz101LT
[13] ANC150

2.10.2 Coarse approach

For coarse movements in the z-direction we use a custom-built motor inspired by the design of Sheheng Pan. The motor consists of a titanium base that surrounds a spring-loaded slider. This slider is moved by 6 shear piezo actuators[14]. A sawtooth voltage generator[15] delivering 800V (peak-peak) is connected to the shear piezos. These high voltages are important, because the capacitance of the piezos and thus their movement decreases considerably (factor of 6) at low temperatures.

The position read-out is done by a capacitor consisting of two pieces: one comb fixed to the slider and one double-comb attached to the titanium base (figure 2.16). One comb of the double-comb is excited with 10 V (Thandar TG503), the other comb is excited with the same signal but shifted by 180 degrees.

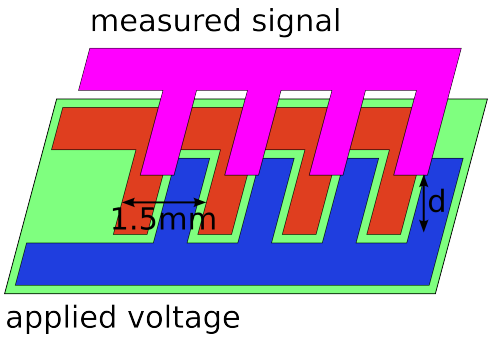

Figure 2.16: Combs used for position read-out: The moving comb on top is either face-to-face to the "in phase comb" or to "the counter-phase comb". The periodicity of the combs is 1.5 mm.

The capacity between the mobile and immobile combs is:

$$C = \frac{\epsilon_0 A}{d} \tag{2.28}$$

where A stands for the geometrical overlap and d for the distance between the two plates. The capacitance is of the order of a few pF.

When the slider moves up and down, its comb will be either face-to-face to the unshifted signal or to the shifted one. The signal is induced into the mobile comb and by amplifing it with a lock-in amplifier[16] we can get a resolution that is higher than the step size at room temperatures. One period of the double-comb is 1.5 mm, so we can deduce the distance moved with the z-motor.

In figure 2.17 the signal at the lock-in amplifier as a function of the number of walked steps in upward direction, against gravity, is shown. The average step size at ±300 V was 630 nm.

The slider is spring loaded, so by applying more or less pressure we can modify the static and dynamic frictions. We can determine the optimal spring pressure by putting a mass on the slider. The maximal mass the slider can move is ∼85 g. We get the following step sizes at this optimal pressure for room temperature :

The theoretical maximal step size x (without gravity) can be estimated with $x = d_{51} \times U$. For our shear piezo $d_{51} = 2 \times 580 \times 10^{-12}$ m/V at room temperature[17], at low temperature this would have to be divided by 6. We would obtain a stepsize of about 920 nm at ±400 V which is of the same order of magnitude as the experimental results.

[14] EBL Products Inc., PZT5a lead zirconate titanate
[15] Swissprobe Piezo-Motor Controller SP869
[16] EG&G Instruments 7220
[17] The factor 2 stems from the fact that we glued 2 piezos on top of each other.

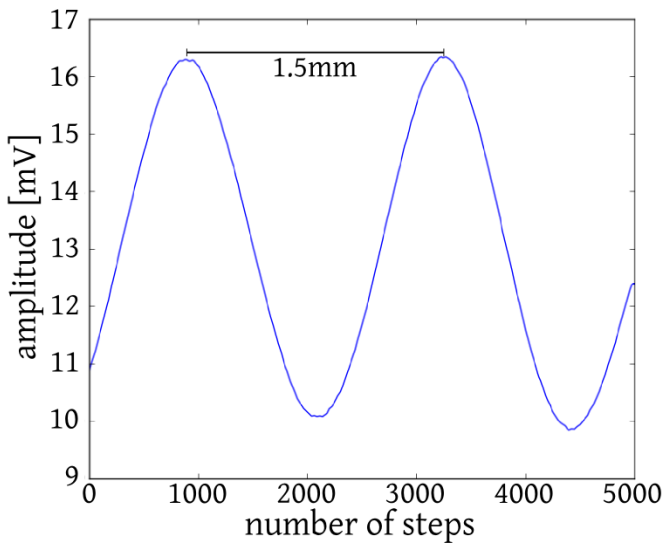

Figure 2.17: Position read-out for the z-motor. One period corresponds to 1.5 mm, thus it is possible to deduce the size of a step. In this example the slider moved upwards. The voltage used was ±300 V at room temperature.

Table 2.3: Step sizes of the z-motor for different temperatures, voltages and directions

temperature	voltage	direction	stepsize
300K	±200V	↑	390nm
300K	±200V	↓	470nm
300K	±300V	↑	630nm
300K	±300V	↓	850nm
300K	±400V	↑	910nm
300K	±400V	↓	1280nm
<1K	±400V	↓	130nm

2.11 Cryostat

For our experiment we use an inverse dilution cryostat[18] (Sionludi): The lowest temperatures are on the top stage, while the highest are at the bottom stage (see figure 2.18(a)). It was developed by A. Benoit, M. Caussignac and S. Pujol at the CRTBT (now Institut Néel).

In total, there are five stages and thus five gold coated cylinders to screen heat radiation from the environment. The sixth and outer most cylinder is the calorimeter.

Because the cryostat does not contain a helium bath when in operation the coldest stage has first to be in thermal contact with the 4 K-chamber. Once at 4 K, this contact has to be cut off to cool down further. The condensation of the helium mixture in the still 1 and 2 cuts off this thermal contact[19].

As can be seen in figure 2.18(b) the circuits for the mixture and ^{4}He are separated.

In the following I want to describe the cooling down in more detail:

1. The ^{4}He-circuit cools down the 4K-chamber. Typically we use a flow rate of 15 l/day (liquid)

[18]The reader is referred to [55] for a more detailed discussion of cryogenics.
[19]US Patent 4,672,823

or 125 ml/sec (gas). This corresponds to 30% on the gauge.

2. Now, we circulate the mixture in the 300 K → 4K circuit under pressure (∼3.5 bar) to obtain a flow rate of 125 ml/s. This gas is cooled down to 4 K by a counter flow heat exchanger (see figure 2.19). Then the gas passes through the still 2, the mixing chamber and still 1.
3. Once all components of the mixing stage are at 4 K (and after the sample approach), we close the 300 K → 4 K circuit.
4. We open the 4 K → 1.3 K circuit that also passes by the heat exchanger and then is cooled down by a Joule-Thomson expansion to 1.3 K. With this gas we cool down the mixing stage. In order to increase the flow rate we use (in addition to the compressor at the inflow) a roots pump and a rotary vane pump at the outflow.
5. When we arrive at 1.3 K, we close the 4 K → 1.3 K circuit and open the dilution circuit which injects the mixture directly into the mixing chamber.

The cooling effect takes place, because there are two phases in the mixing chamber: one ^{3}He-rich phase and one ^{4}He-rich phase. By evaporation of ^{3}He from the ^{3}He-rich phase to the ^{4}He-rich phase, heat is extracted from the mixing stage, so that temperatures of 50 mK - 100 mK can be achieved.

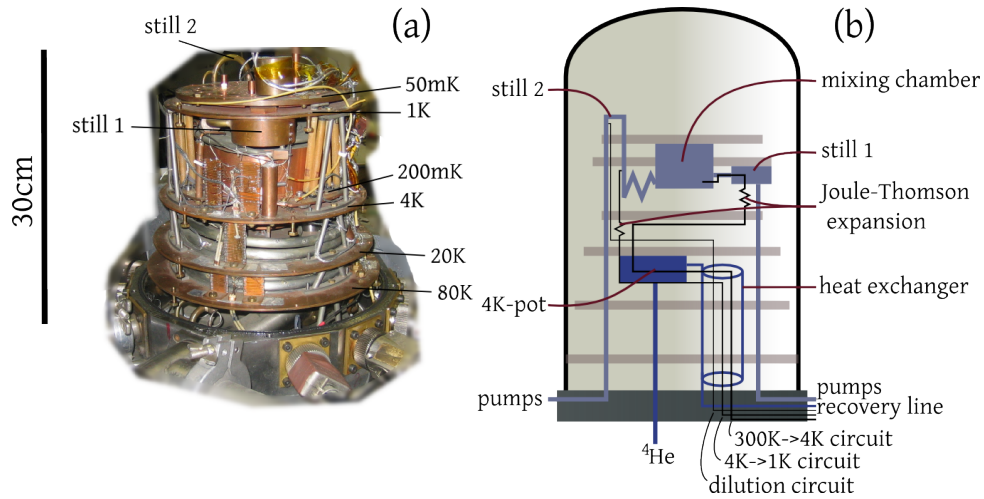

Figure 2.18: (a) Photo of the used inversed dilution cryostat. The lowest temperatures are achieved at the top. (b) Schematics of the cryostat. For details on the cooldown process refer to the text.

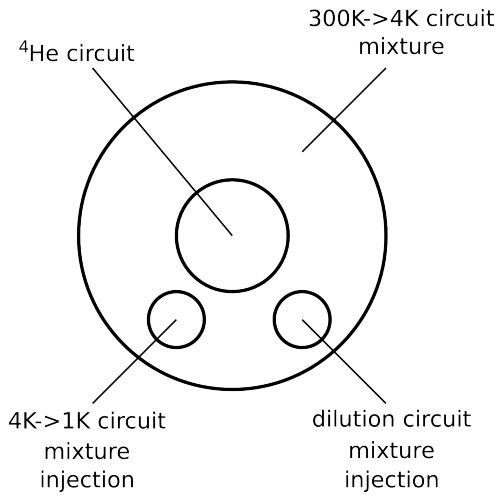

Figure 2.19: Cross-section through the tubular heat exchanger used to pre-cool the mixture.

2.12 Magnetic field

We used one copper coil in z-direction. The coil is directly attached to the calorimeter and provides 68 G/A. For the in-plane component of the magnetic field we can add two Helmholtz-coils that generate a magnetic field of 16.8 G/A at the sample position.

The current sources to drive these coils can provide maximal 3 A, thus giving us a magnetic field in z-direction of 204 G. This is higher than the critical field of our aluminium SQUID (∼120 G).

2.13 Electronics

2.13.1 Overview

An overview of the electronics is shown in figure 2.20.

The PC controlling the whole experiment, either directly or via the DSP card, can be seen in the center of the diagram. The J-Box beneath the PC is the starting point of the regulation loop[20] generating the excitation for the tuning fork and a reference for the lock-in amplifier. It also provides an interface between the PC and the SQUID electronics.

The current source generating the magnetic field via coils is controlled by the analog output signal of the DSP.

The thermometry is controlled via two serial connections between the PC and two control devices EPSON PX-16 (firmware written by Alain Benoit). The two EPSON PX-16 communicate with two ORPX (automatic resistance measurement devices) which are connected to the thermometer resistors.

The motor position control is done by the corresponding controller electronics in the case of the attocubes and by a Swissprobe sawtooth generator (SP869) in the case of the custom-built z-motor. The position read-out is done via a lock-in amplifier using the capacitance combs explained on page 33.

The first year of this thesis involved developing, debugging and progamming the - for the better part custom-built - electronics. As can be seen in figure 2.20 there are several subsystems that will be discussed separately in the following sections.

2.13.2 Thermometry

We have chosen a well-proven thermometry system developed in the lab (at that time CRTBT): two ORPX, each connected to one EPSON PX-16 for the temperature regulation and the user interface. Each one of these pairs can measure 8 thermometers simultaneously. As there are 4 thermometers (3 wires) connected to each Jaeger socket, 2 sockets are used by each ORPX.

For the different stages and locations of the cryostat we use different thermometers/resistors: The temperatures at the two stills are measured with two ruthenium resistors, the 4 K pot with one carbon resistances for lower temperatures and platinum for higher ones. The mixing chamber temperature is determined with four different thermometers: two carbon, one germanium and one ruthenium. The sample temperature is obtained by two different carbon resistors connected to the sample holder by means of a silver sheet.

The temperature of the SQUID is measured by a carbon resistor placed as close as possible to the SQUID. The critical current can also be used as temperature indication between scans at constant

[20] as already discussed on page 27

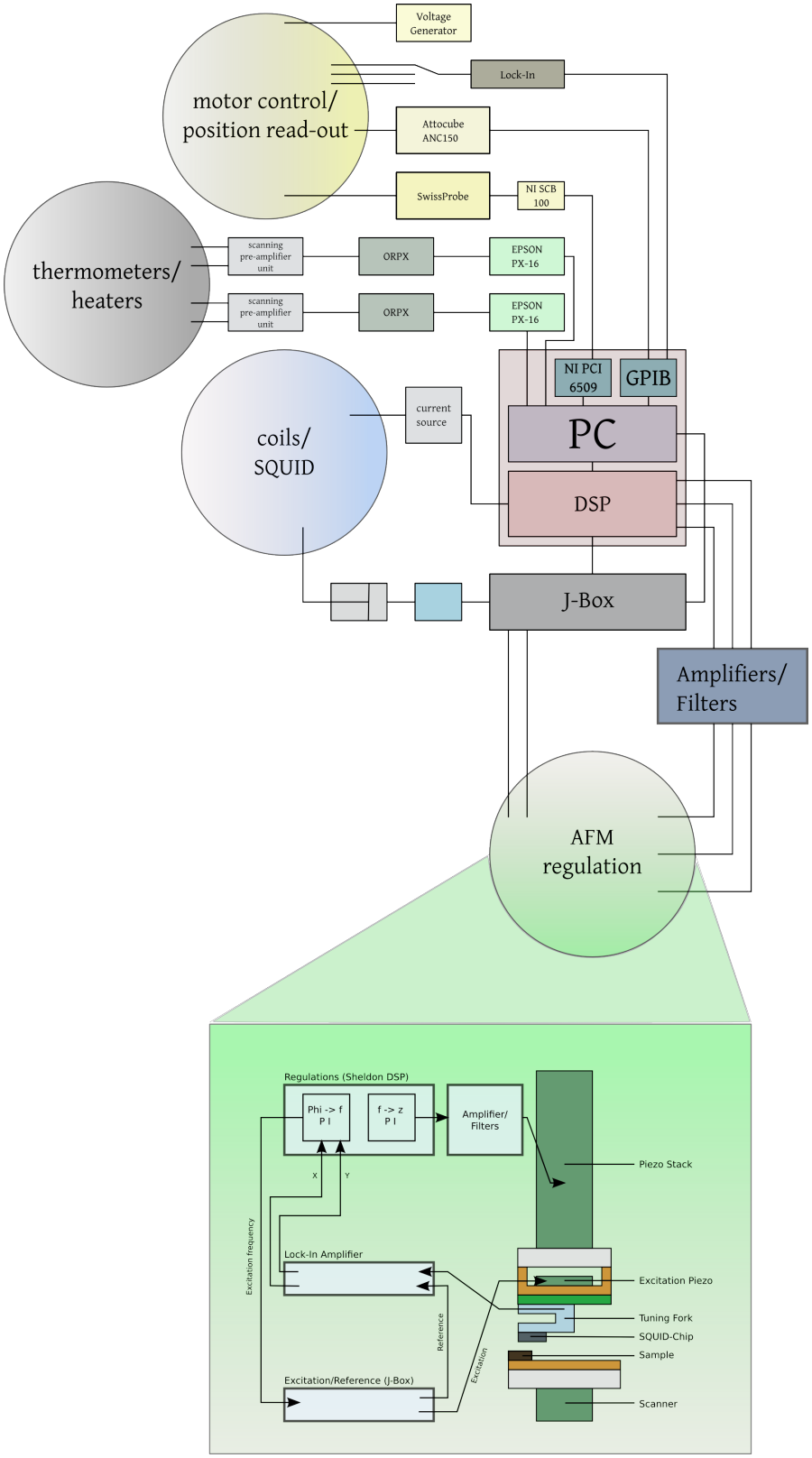

Figure 2.20: Overview of the electronics. Refer to text for explanations.

fields.

2.13.3 Motor control

We use one custom-built motor for the z-direction and two attocubes for lateral movements. The custom-built motor is controlled by a Swissprobe Piezo-Motor Controller. We can use the existing hand-controller or use the PC via a NI PCI-6509 input/output card interfaced by a NI SCB-100 card to the Swissprobe Controller.

We communicate by means of a serial connection with the ANC150 that controls the two attocube motors.

A voltage generator is used in combination with a lock-in amplifier for the position read-out (see page 2.10).

2.14 SQUID read-out and tuning fork excitation

A custom-built electronics (*J-Box*[21]) was implemented in order to control the SQUID ramp and read-out its critical current (see section 2.3.2).

The main feature of the J-Box is the possibility to generate two sinusoidal signals with the **same frequency** and a **constant phase**. For this, two Digital Data Synthesizers (DDS) using the Cordic algorithm to generate a sinusoidal signal are used. One signal excites the tuning fork by means of a piezo element, the other one is used as a reference for the lock-in amplifier. Refer to section 2.7 for more details.

An important feature of the J-Box is the possibility to control the excitation and reference frequency either by PC (used for frequency sweeps) via an embedded platform (Beck SC12) or by a direct connection with the DSP (used for the frequency regulation). This is accomplished by a field programmable gate array (FPGA) redirecting the inputs from the DSP or an ethernet connection to the two DDS. A schematic is depicted in figure 2.21

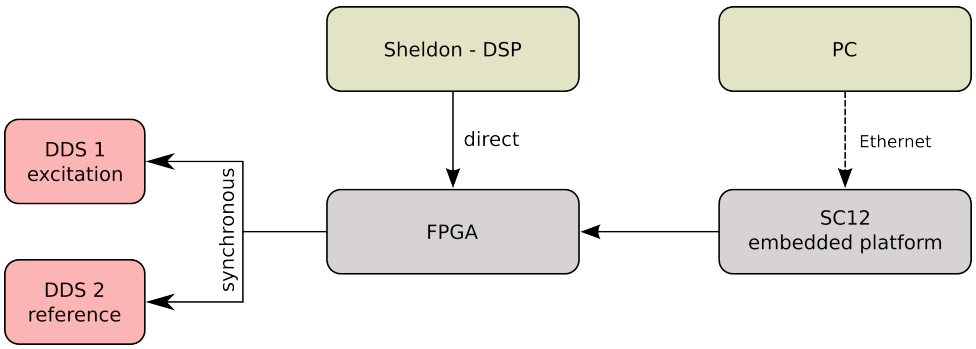

Figure 2.21: J-Box: electronics responsible for the excitation of the tuning fork and reference signal used in the regulation loop. Frequencies, phases and amplitudes can either be changed by the PC (for frequency sweeps) via an embedded platform (Beck SC12) or directly by the DSP card (for regulation).

[21] after Julien Minet who developed the electronics.

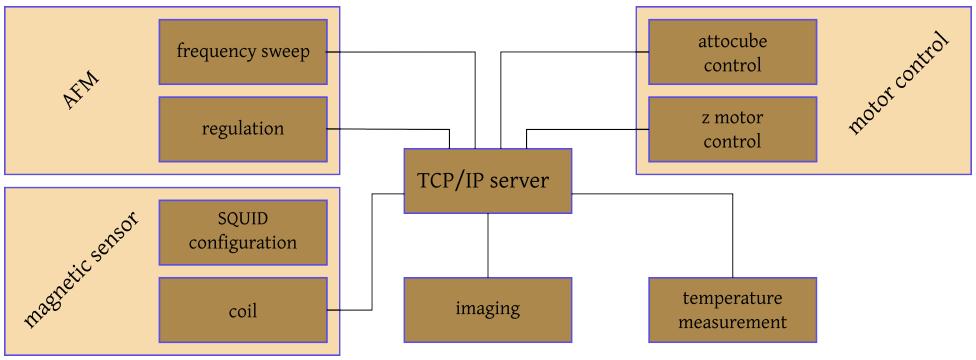

Figure 2.22: Software overview: most of the programs communicate with the TCP/IP server that controls the DSP card. Refer to text for more details.

2.15 Software

2.15.1 Overview

In figure 2.22 an overview of the software running on the control PC is given. Almost all the software is written in LabVIEW.

In order for different sub-systems to have access to the same hardware resources, most VIs connect to a TCP/IP server providing an interface to the DSP card controlling the hardware.

There are two virtual instruments (VI) for the **AFM control**: Either the frequency sweep VI or the regulation VI controls the DDS: The frequency sweep uses an ethernet connection (UDP) to change the frequency, whereas the regulation VI only passes the regulation parameters (proportional value P, integral value I) to the DSP that changes the frequency (see figure 2.21).

The **SQUID electronics** is independent of the TCP/IP interface VI, as it communicates directly by ethernet (UDP) with the SQUID electronics. The current through our coils and thus the magnetic field is adjusted by using one analog output of the DSP card connected to a custom-built current source.

Another independent group of programs are the VIs controlling the **motors (attocubes and z-motor)**.

The actual **imaging program** is also written in LabVIEW. By a TCP/IP connection to the DSP interface VI it controls the position of the scanner, reads out the z-piezo stack voltage (for AFM imaging) and simultaneously reads out the critical current of the SQUID (magnetic imaging).

The **temperature measurement** is done by an electronics (EPSON PX-16) connected via the serial port. The software is written in Python/PyQt and consists of a custom plotter widget.

The main reason LabVIEW was chosen as programming language is that the DSP card itself (see next section) is interfaced with LabVIEW. But the above described architecture allows us to use any language we like in the future as long as it is possible to connect to a TCP/IP server.

2.15.2 Regulation

The electronics is controlled by software written during the present thesis. We chose to use the LabVIEW environment for this task, as the DSP can be programmed by using LabVIEW's graphical language G. It was estimated that the development would be easier than programming the DSP directly with C and would not require to buy a compatible C cross-compiler.

Interpreter The user programs a sequential (each DSP-VI uses an input and output only for that purpose) LabVIEW program using the QuVIEW library. The structure of this sequence is very similar to assembler code: only statements and conditional jumps (only forward) are allowed. It is not possible to store values which can be used in the next iteration. The last VI then generates a table with these commands and conditional jumps (loops are not allowed).

Sheldon Instruments (manufacturer of the DSP) has written a fast interpreter running on the DSP that receives a sequential representation with all the commands and conditional jumps (if) of the user's LabVIEW program. This program is started on the DSP and will run in a loop until one shuts off the DSP.

Communication In order to access a variable that runs on the DSP one can use two methods: Either one sends variable values one by one after each cycle (15625 cycles/second). This is very time consuming for the DSP and too fast for the PC, so we opted for the second possibility: one buffers the values and sends it to the PC once the buffer is full.

When the PC program wants to write a value to a variable this is done by a two-sided memory so that no read/write conflict can occur.

Debugging One of the key problems in programming an embedded system is debugging: Conventionally debugging can be eased by the use of a JTAG[22] connection. It provides an interface between the hardware running the code and a debugger software giving the possibility of step-by-step execution of the program code and putting of break-points. Break-points stop the program at a designated line and from there on the programmer can use the step-by-step execution. This debugging technique has the advantage that the state of the program and its variables are visible to the programmer which can then more easily figure out the origin of a software bug.

In the case of the Sheldon DSP card, this procedure to find bugs is not built-in, so it is much more difficult to find bugs in a program. Typically bugs can freeze the PC host system. The most effective way to deal with them is to remove sub-program after sub-program until the program runs and then try to figure out where the bug came from. It is needless to say that this slows down the development considerably.

Conclusion In conclusion we have developed a flexible software system (client-server architecture) that can easily be extended in the future by using different programming languages. We have delegated the real time tasks (regulations) to a suitable DSP and gather all the data in parallel on the PC.

The server running on the host PC is connected to clients (imaging, frequency sweep etc.) sending and receiving data and commands. The real time tasks (regulations) are delegated to the DSP board in the host PC (for details on the regulation see section 2.7). All the DSP outputs (scanner position, z-stack voltage) can be directly controlled by the user via the client programs permitting a flexible use of the microscope.

2.16 Validation and Calibration of the microscope

In this section we show the first measurements done with this microscope. These measurements enabled us to characterize and study the sensitivity, the scanning range, possible scanning speeds and the regulation.

[22] Joint Test Action Group, IEEE 1149.1 Standard Test Access Port and Boundary-Scan Architecture

2.16.1 Approach-Curves

Figure 2.23 shows a typical approach curve obtained at 250 mK. As we approach the surface the resonance frequency of the tuning fork goes up. We do not see the attractive branch due to a limited frequency resolution and the stiff tuning fork. This simplifies the regulation process as we can consider our frequency-distance dependence being monotonic.

The fluctuations of the frequency become bigger as we approach the surface (between 10 and 15 nm). This is due to limited speed of our phase-frequency regulation as the P and I parameters which were chosen to minimize hard contact between tip and sample in combination with the frequency-z regulation.

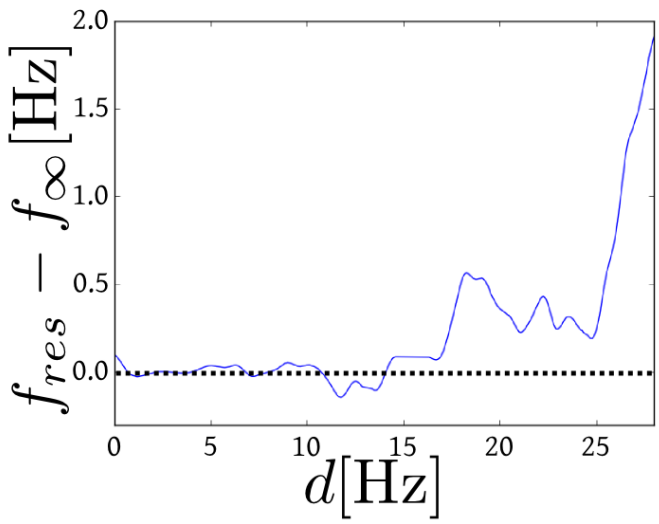

Figure 2.23: Typical approach curve. The phase-frequency regulation was set as it is used for scanning. Notice the unstable regulation in the vicinity of sample contact. Performed at 0.25K.

The frequency fluctuations of the approach curve can be explained by vibrations in the mechanical setup of the microscope. We have verified that the vibrations due to the scanner and z-Piezo are smaller than 1 Å. The most plausible source are therefore the attocubes on top of the microscope. For the magnetic imaging these vibrations are not important and are a part of the compromises made when building an experimental setup like a scanning microscope: In the case of magnetic imaging the scan range has to be larger than the features to be imaged (vortices, magnetic domains) making atomic resolution both difficult (due to high scanning speed to obtain images in a reasonable time) and low-priority.

2.16.2 Calibration

Sample

The sample used to calibrate the microscope scanning range is a thin niobium film (200nm) with 3 levels of self-similar checkerboard motifs as shown in figure 2.24(a): On the highest level it consists of 5 × 5 squares with a side length of 100 μm. One half of the squares are niobium squares, the others consist of a smaller 10μm × 10μm checkerboard (see figure 2.24(b)) in which the squares are either niobium squares or an even smaller 10 × 10 checkerboard with niobium islands of about 1μm side length 2.24(c).

The whole checkerboard is surrounded by lines growing in thickness with distance to the main checkerboard. This feature was added to facilitate the search for the sample and is generally useful for orientation on a periodic motif.

As one can see in figure 2.24(d) shaped holes were added in order to show the direction of the sample center (see arrow). These holes trap vortices as shown later on.

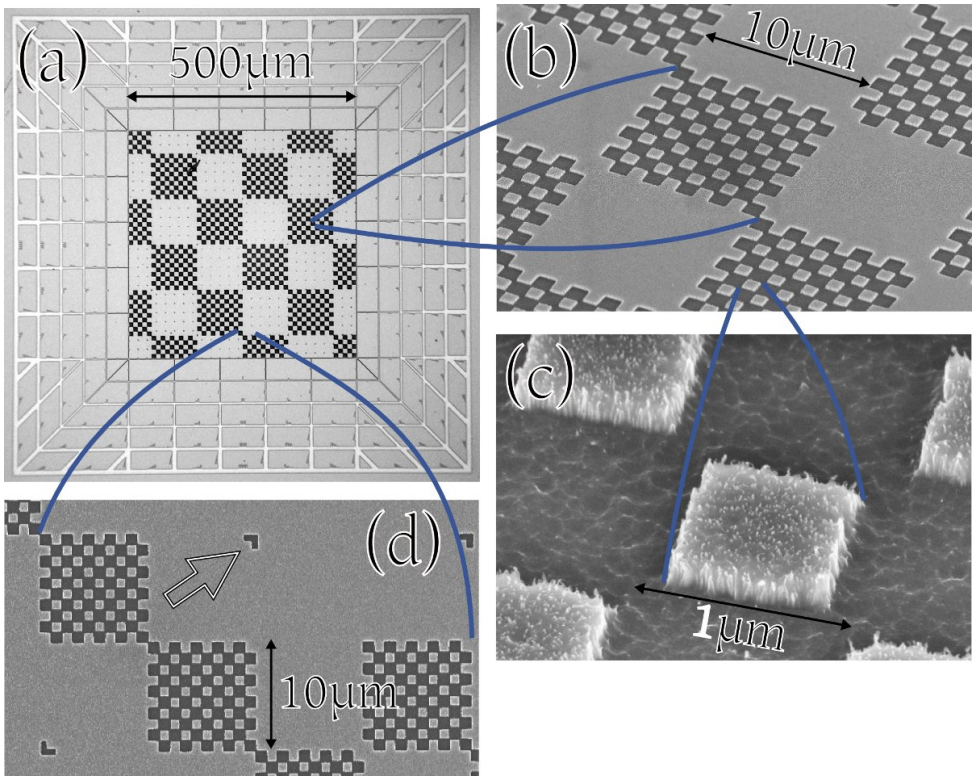

Figure 2.24: Sample: (a) optical image: around the chessboard you can see lines that help to find the center. (b) zoom on one small square of (a). (c) zoom on the smallest Nb element (1 micron). (d) the arrow points to a motif in the film (for orientation purposes).

Imaging

scanning range As already described this microscope does magnetic and topographic imaging simultaneously. In figure 2.25 one can see the images taken by measuring the critical current of the SQUID (a), (c), (e) and their corresponding topographic counterparts (b), (d), (f). Notice that the squares in the magnetic images correspond to $10\mu m \times 10\mu m$-squares, while we see also the $1\mu m$ niobium islands in the AFM images. The black or white discs in the magnetic images are vortices. Integrating the magnetic flux over an isolated vortex yields Φ_0 (the integration area is indicated by a circle in (c)). On top of figure 2.25 the critical current cross-sections are shown as indicated in the magnetic images. At the bottom the corresponding topographic cross-sections are depicted. They are used in the following to deduce the scanner and z-piezo range:

- **scanner range:** The maximal voltage applied to the bimorph piezo elements constituting the scanner is ± 200 V. By comparing this with the cross-section we deduce the maximal image range to be 85.0 µm($\pm$1.1 µm) $\times$ 70.1 µm($\pm$1.5 µm)
- **z-piezo range:** The data sheet of the z-piezo states that the maximal elongation is 35.2 µm $\pm$ 3.5 µm at 110 V (at room temperature). Typically the capacity and thus the piezo-electric properties decrease by a factor of 6 at low temperatures. Consequently, a voltage difference of

3 V at low temperatures results in an elongation/shortening of about 160 nm, being not too far from the Nb-film depth of 200 nm. This indicates that the tip does not reach the bottom of a hole. The smoothed out topographic cross-sections in figure 2.25 further support this explanation.

relation between topographic and magnetic images As one can see by comparing the corresponding magnetic and topographic images, they are **shifted** with respect to each other. The crosses in figure 2.25 show corresponding positions. The shifts stem from the fact that there is a certain distance between the SQUID and the point of the SQUID-wafer touching the sample. This distance is 15 μm (as well in the images as on the SQUID-chip, see figure 2.26).

scanning speed The quality of the topographic images depends naturally on the image resolution but also on the **scanning speed**. The faster we scan, the harder it is for the regulation loop and the z-piezo to compensate for sudden changes of the sample topography. This drop in quality can manifestly be seen in figure 2.25(f), in which the vertical lines appear, an indication for a too slow response of the AFM-regulation loop. Image (f) was taken with a scanning speed of 0.8 μm/s. For (d) and (c) the scanning speeds were 0.4 μm/s and 0.26 μm/s, respectively. The arrows in figure 2.25 connect identical surface defects on different images: the upper defect in (d) is clearly smaller than the surrounding checkerboard, whereas in (f) the defect seems to become bigger because of the regulation being too slow.

spatial resolutions The reason for the spatial magnetic resolution being much lower than the topographic one, is simply due to the fact that the SQUID-sample distance was about 1.5μm in this experiment.

vortex deformation It is difficult to find the orientation in the case of a featureless surface, consequently shapes where added in between checkerboards as indicated by the arrow in figure 2.24(d). The holes in the niobium film naturally trap magnetic flux. In figure 2.25(c) we can clearly make out the difference between isotropic vortices in the homogenous film and magnetic flux trapped in the orientation motifs. Three arrows indicate the location of these motifs.

filling The zero magnetic field can be deduced by finding the applied field that minimizes the number of vortices. It has been found to be 0.18 G for this experiment. In figure 2.27 one can see two images at different fields: (a) was taken at an applied field of 0.52 G, leading to a magnetic field of 0.34 G, (b) 1.01 G (0.83 G). The white squares in the images correspond to a chessboard with 1 μm^2 niobium islands. Here the field passes between the squares thus the magnetic contrast is homogenous.

By using $\Phi = B \cdot A$ we would expect a vortex density of $n_1 = 1.6/(10\ \mu\text{m}^2)$ and $n_2 = 4.0/(10\ \mu\text{m}^2)$ for the first and second field, respectively. By counting the number of vortices, one finds on average a filling factor of $0.75/(10\ \mu\text{m}^2)$ (a) and $4.85/(10\ \mu\text{m}^2)$ (b). The discrepancy from the calculated results stems from the fact that the superconductor is inhomogenous and as a consequence the flux passes preferentially between the SC regions.

border Vortex interaction in a thin film can be illustrated by two magnets repelling each other due to the spreading of their flux lines. In figure 2.27 one can see vortices trapped in a triangular niobium region (the magnetic field being 0.75 G). Outside of this region the magnetic flux lines are very dense thus repelling the vortices from the border. Since inter-vortex repulsion is weaker than the repulsion at the border, there is a thin region at the border with a low vortex density. This border

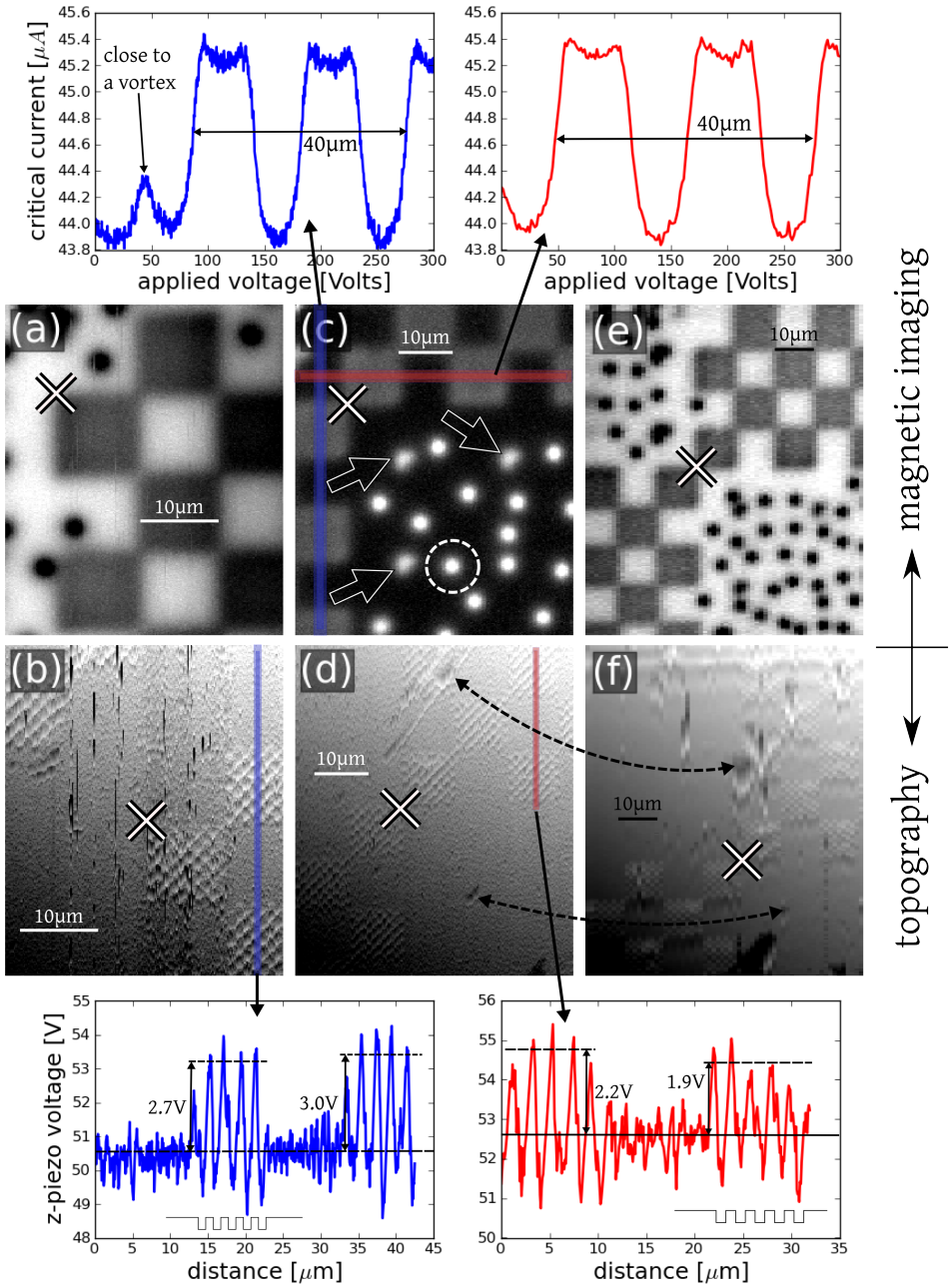

Figure 2.25: Calibration: in the first row magnetic images are depicted, their AFM counterparts are in the second row. The graphs on top and at the bottom are the cross sections taken at the lines with corresponding colors. (c) The arrows point to trapped magnetic flux due to the orientation motifs in the Nb film (see figure 2.24(d)). The flux inside the circle corresponds to Φ_0. The crosses show the corresponding spots between the magnetic and AFM images. The shift of 15 μm is due to the SQUID not being at the AFM tip's position (see figure 2.26).

repulsion was modelled and experimentally verified by Kuit in superconducting stripes of different width [56].

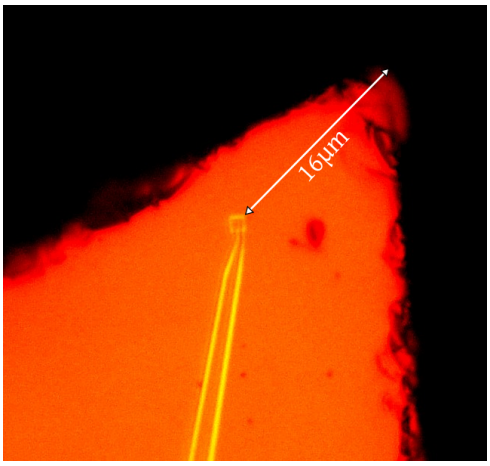

Figure 2.26: Optical image of a SQUID tip: The distance between the physical tip (AFM) and the SQUID corresponds to the shift between the AFM and the magnetic images in figure 2.25.

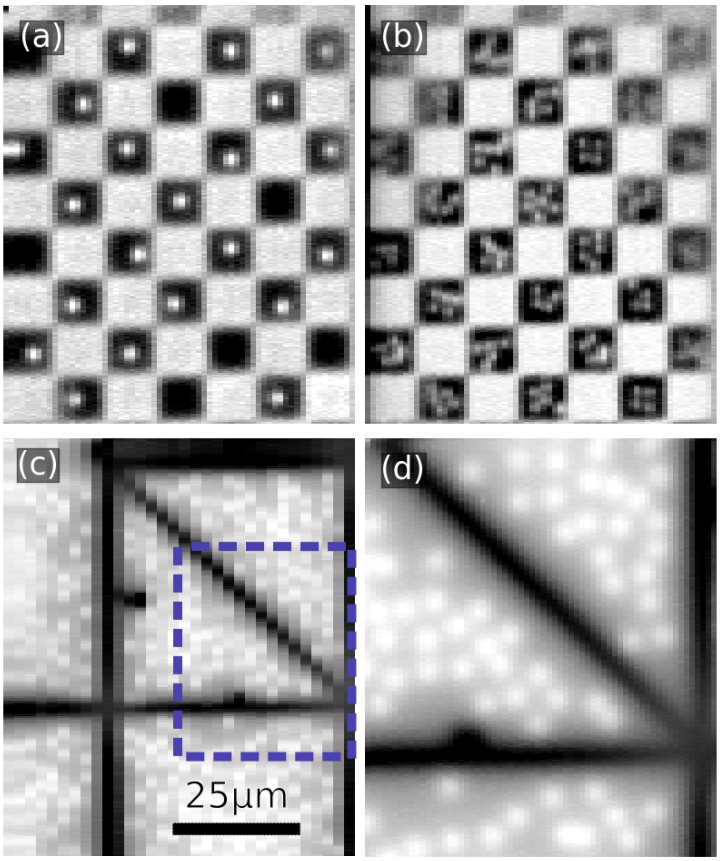

Figure 2.27: Magnetic images: (a) The white squares correspond to the patterned squares, whereas the dark squares are full niobium squares. Each square has a size of 10 µm by 10 µm (image size 70 µm × 85 µm. In a magnetic field of 0.34 G we observe a vortex density in the squares of $0.75/(10\ \mu m^2)$ (b) The magnetic field was increased to 1.01 G leading to a vortex density of $4.85/(10\ \mu m^2)$. (c) The black lines in the image correspond to orientation guides. Only in the white regions there is niobium. (d) A zoom on the rectangular region in (c). The vortices can be clearly distinguished. The field in (c) and (d) was 0.75 G.

Robustness

The purpose of our microscope is not to achieve atomic force microscopy with an atomic resolution, but to do magnetic field images. We also want to be able to scan larger areas than what is usually done by high resolution AFMs and for this we need higher scanning speeds without breaking the SQUID. For this specific goal we have to make a compromise between spatial resolution of the topographic images and the durability of the SQUID. From the beginning we wanted to be able to use the same SQUID during one cool-down for several weeks.

This goal was accomplished, as we were performing measurements during 2 cool-downs for 3 months on UCoGe with the same SQUID (see chapter 6) and for one month on Rhenium (see chapter 4).

2.17 Possible improvements

In the course of the development and the first measurements we have had several ideas how to improve the microscope. Some of them have already been implemented for a **new microscope model** built by Zhao-Sheng Wang. In this section I want to describe ideas that are being worked on and will be implemented before long:

new SQUID-tip design: We are developing a new SQUID design that combines the two advantages of the former designs obtained by cutting and etching: precise positioning of the SQUID close to the two edges of the tip and obtaining a precise AFM tip, by putting the SQUID on a sharp, narrow “finger“ (see figure 2.28).

increased spatial resolution: A new SQUID design will enable us to position the SQUID closer to the surface (see figure 2.28). The new asymmetric geometry allows simpler alignment between scanning tip and the sample, thus making a SQUID/sample distance of 50 nm possible. We think that SQUID sizes of 200 nm × 200 nm can be achieved by e-beam lithography.

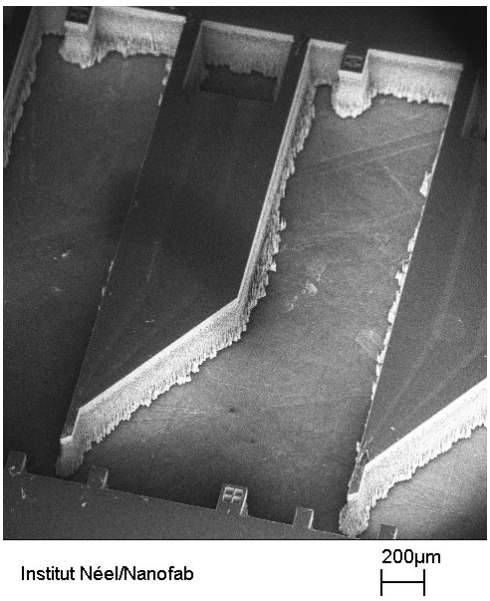

Figure 2.28: Electron microscope image of the new SQUID tips (image taken and devices fabricated by Thierry Crozes). The new geometry will allow scanning in only 50nm height. As a consequence of this reduced height the magnetic signals will be stronger making it possible to reduce the SQUID size to 200 nm.

non-hysteretic SQUIDs: There is an ongoing effort (SuperNanoCharac project of the NanoScience Fondation (Grenoble, France)) to develop shunted SQUIDs which would allow for linear flux measurements, in constrast to our periodic multi-valued critical current measurement. The sensitivity of a shunted SQUID would also be superior to the current SQUID as the SQUID noise is proportional to the factor $\sqrt{f_{Josephson}/f_{sampling}}$. Since this factor becomes 1 in the case of a shunted SQUID we gain - in the ideal case - four order of magnitudes of sensitivity (our current sampling rate is of the order of 1 kHz). Other groups (K. Moler, E. Zeldov) have SQUID sensitivities that are only two order of magnitudes higher than our SQUID's sensitivity, thus other noise sources (thermal noise, shot noise) have to be taken into account. Nevertheless, we project that the future SQUID will surpass the sensitivity of the current SQUID by at least a factor of 10.

advanced regulation loop: As we have seen in this chapter our sample distance regulation loop is based on PI controllers. This is also the case for commercially available electroncis like the Nanonis SPM controller. One interesting improvement would be to have a self-adjustable PI controller that automatically finds good P and I values for the regulation. Other more advanced regulation schemes like RST or H_∞ have been proposed [57] for use in scanning microscopes leading to faster feedback and thus ultimately sharper pictures (STM/AFM) and less tip abrasion (scanning SQUID microscopy).

smaller z-Stack: As the range of the piezo-stack we have been using is very large ($\sim$ 6 microns at low temperatures), we use a smaller z-Stack in a new version of the microscope, leading to less heat development having less capacitance when extending at the beginning of a scan.

custom-built lateral motors: We think it would be useful to build custom-built motors for lateral movement in order to replace the attocube motors, that are mechanically fragile. At time of writing the designs are already finished (G. Garde).

delegate scanning to separate electronics: In order to reduce the time it takes to scan the surface, we should also delegate the scanner control to a separate arbitrary waveform generator. At the moment the scanner is controlled by a VI running on the PC leading to needless latency between pixels.

3

Comparison with other microscopes

In this chapter we put into perspective our microscope to other techniques capable of magnetic imaging in real space. We address their advantages and disadvantages and compare our instrument with other magnetic scanning microscopes and their practical and technical differences.

Finally, we briefly introduce a new scanning scheme that reduces the imaging time by several orders of magnitude.

3.1 General techniques

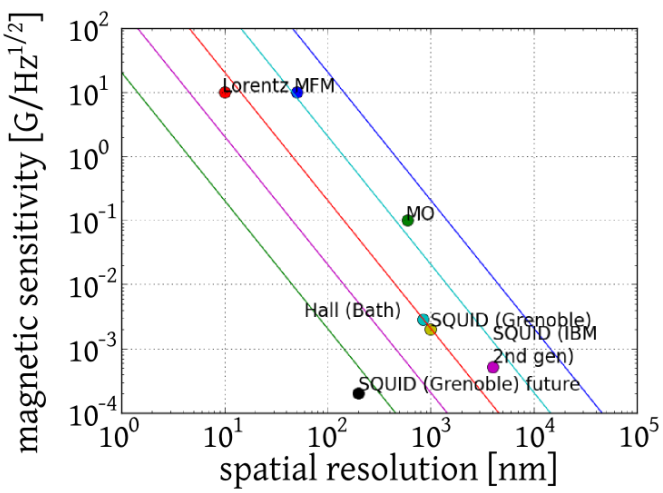

Figure 3.1: Comparison of the different techniques allowing for vortex visualisation. Data taken from [58] and [59].

Bitter decoration: The Bitter decoration technique can be used to visualize vortices attracting magnetic particles because of the field gradient. This technique was the first that made vortices visible (see chapter 1). The main disadvantage is that in order to see the resulting position of

the particles one has to warm up, open the cryostat and look at the sample. Thus only one measurement per cooldown can be obtained.

Differential phase Lorentz microscopy: In Lorentz microscopy [60] one uses the fact that the phase of electrons passing through a vortex is changed with respect to other electrons not affected by the vortex. With this imaging technique it is possible to determine the position of a vortex with a high spatial resolution (∼10 nm) and one can make images at a rate of 30 Hz. The main problems are that the samples have to be very thin (∼100 nm) for electron transmission to be high enough and the magnetic sensitivity is only in the order of 10 $\frac{\mathrm{G}}{\sqrt{\mathrm{Hz}}}$.

Magneto-optical imaging: If a magneto-optic layer is placed on top of the sample the polarisation direction of polarised light is changed in the vicinity of a vortex. The proportionality constant between magnetic field and the change in polarisation per meter in the magneto-optic layer is called Verdet-constant. This technique is famous for making it possible to see vortex avalanches and dynamic behaviour of vortices. This is due to the very high frame rate of 10^8Hz [61].

A practical difficulty is the need of close contact between the sample and the magneto-optic layer. The drawback is the magnetic resolution of 0.1 G. But the spatial resolution is 0.6 microns at best [62].

Magnetic force microscopy: Magnetic force microscopy is closely related to standard atomic force microscopy. The only difference being that the tip is made of a magnetic material which provides a magnetic interaction with the sample surface. The huge advantage compared to other scanning techniques is the high spatial resolution of ∼50 nm. Although early MFM had poor signal to noise ratios for vortices [63], more recent images are much better [64]. The vortex/tip interaction is not negligible and can lead to displacement of vortices. By controlling the height of the MFM tip the displacement of vortices can be turned on and off and thus it can be used to control the vortex position (see figure 3.2). In order to interpret the MFM images quantitatively one requires precise information of the tip magnetization which is difficult to obtain.

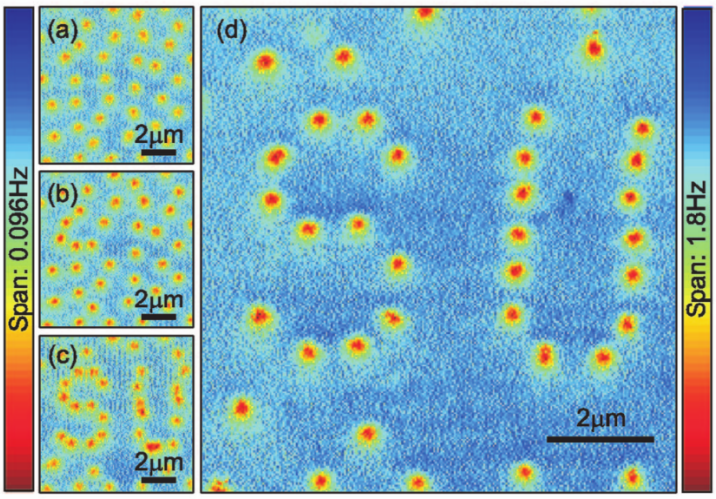

Figure 3.2: Vortices moved into position by an MFM. The height of the tip is used to turn the interaction between tip and vortex on and off, from:[65].

Hall probe microscopy: Another scanning technique is the Hall probe microscopy ([66], [67]). It combines good spatial resolutions (850 nm) with a good magnetic resolution of $\sim 2.9 \times 10^{-3} \frac{\mathrm{G}}{\sqrt{\mathrm{Hz}}}$. In contrast to SQUID microscopy where the field sensitivity goes linearly with the pickup area, Hall probe sensitivity is nearly independent of this area (see [59]). This means that by using SQUID microscopy the experimentator can choose its sensitivity and spatial

resolution according to his/her needs. In the next section we are going to discuss the scanning Hall probe microscope developed in Bath, UK in the group of S.J. Bending.

A more detailed comparison of these techniques and their respective sensitivity, spatial resolution and speed is given in [58] (1999).

In figure 3.1 we summarize the typical magnetic and spatial resolutions of these techniques. We also predict realistic performances of the new SQUID tip mentioned in chapter 2.

In the following sections we focus our attention on the scanning Hall probe and SQUID microscopes. We want first to discuss the latter by studying the developments of the S.J. Bending group.

3.2 Scanning Hall probe microscopy

The scanning Hall probe microscope of the Bending's group is depicted in figure 3.3.

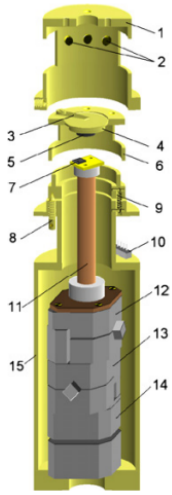

Figure 3.3: Hall probe microscope used in S. J. Bending's group in a ^{3}He cryostat. 1) receptable tube, 2) LED array, 3) Bronze flat spring, 4) Sample holder disk, 5) Sample, 6) Sample holder cup, 7) Hall probe, 8) Alignment screw, 9) Extension bronze spring, 10) Electrical connectors, 11) Piezoscanner tube, 12), 13) Attocube ANPx100 positioners, 14) ANPz100 positioner, 15) Brass microcope hull, from: [68].

Instead of an AFM tip as in our case, they use a STM tip (positioned very close to the Hall probe) for the sample/Hall Probe distance regulation. The two possible combinations STM/Hall probe and AFM/Hall probe are shown in figure 3.4. Three attocube stages are used for coarse movement and a piezo-electric scanner tube for scanning.

The big advantage of using a Hall probe instead of a SQUID is the increased temperature range. With the scanning Hall probe microscope they can access temperatures from 0.3K up to room temperature. As already mentioned the typical spatial and magnetic resolutions are $\sim$ 850 nm (although 50 nm have already been reached with a rather poor noise-equivalent field (0.86 G/$\sqrt{\text{Hz}}$) [69] using a bismuth sensor) and $\sim 2.9 \times 10^{-3} \frac{\text{G}}{\sqrt{\text{Hz}}}$, respectively.

3.3 Scanning SQUID microscopy

For SQUID microscopy we generated a comparison chart (by taking the data from [70], [71]) showing different SQUID configurations mostly used in this decade (only Vu (1993) and Kirtley (1995)

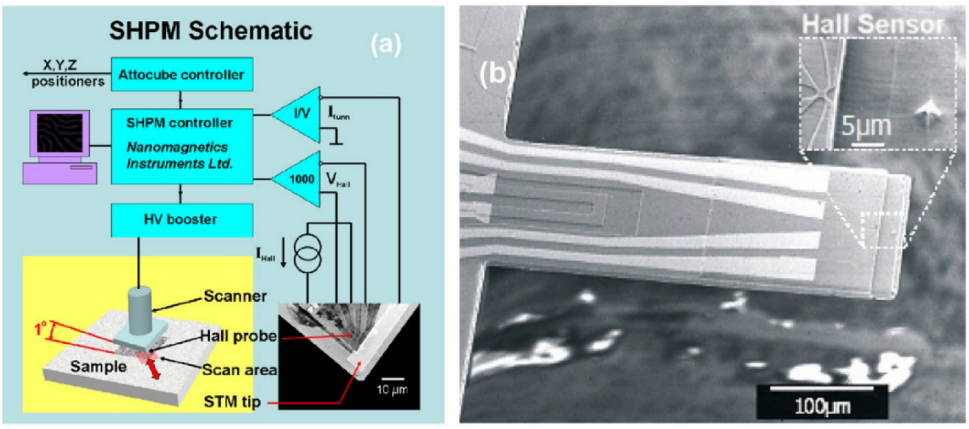

Figure 3.4: (a) Diagram of a typical scanning Hall probe microscope system with STM height control. (b) Optical image of an AFM height control system with an piezoresistor for deflection measurements, from: [68].

are older). As one can see the spatial and magnetic resolution of our present/future SQUID and are close/beyond state of the art.

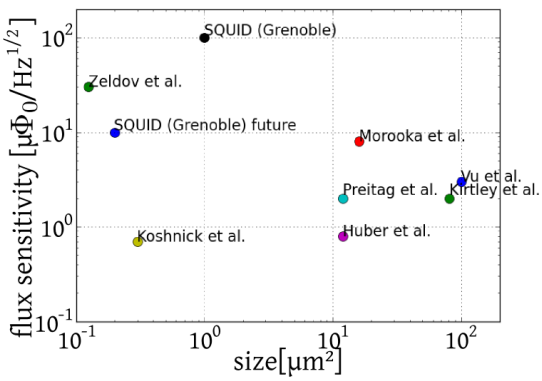

Figure 3.5: Comparison of the spatial and flux resolution of different SQUIDs (mostly from this decade, Vu et al (1993) and Kirtley et al (1995) are older). The spatial resolution of our present 1 μm SQUID is close to the state of the art. The projected resolution of a new SQUID is ~200nm surpassing most competitors. Data taken from [70] and [71].

3.3.1 Stanford group

The biggest difference of the SQUID microscopes used in Kathryn Moler's group at the Center for Probing the Nanoscale (Stanford University) is the SQUID used for measurements. Three aspects are crucial:

temperature range: the SQUID is made out of niobium and can consequently be operated with a ^{4}He-cryostat with much more cooling power than a dilution fridge. This means that the thermally decoupled sample can be heated up to 130 K without the SQUID transiting to the normal state.

shunted SQUID: the SQUID is shunted and non-hysteretic meaning that its working critical current can be set and maintained by a feedback loop using a small current loop - generating a magnetic field - around the SQUID as feedback, nulling the field.

pick up loop: the effective area of the SQUID is modified: a small pick up loop at the border of the SQUID chip is fabricated to reduce the distance between the SQUID and the sample and to improve the spatial resolution.

The SQUID with its pick-up loop is shown in figure 3.6.

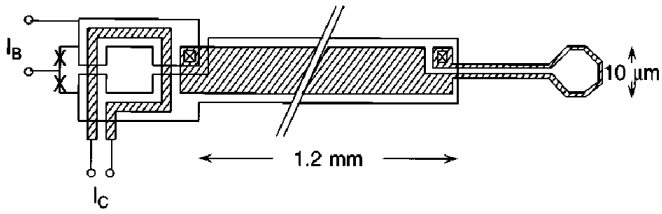

Figure 3.6: Schematics of the SQUID magnetometer with the pick up loop on the right hand side, from [72].

Another difference between the microscopes is that we use a tuning fork as an AFM sensor whereas the Stanford group glides over the sample surface without regulation. The contact is established by capacitance measurements, but the height cannot be controlled.

3.3.2 Weizmann group

Recently (2010), Eli Zeldov's group at the Weizmann Institute of Science presented a new fabrication process for SQUID tips [71] (see figure 3.7). A quartz tube is pulled to a sharp tip, then aluminum is deposited on the tip from two different sides on this tube. The two depositions are not in contact and correspond to our SQUID-arms. In a last step aluminum is also deposited on the apex connecting the first two depositions by two weak links. This way, SQUIDs with an effective diameter of 100nm can be fabricated.

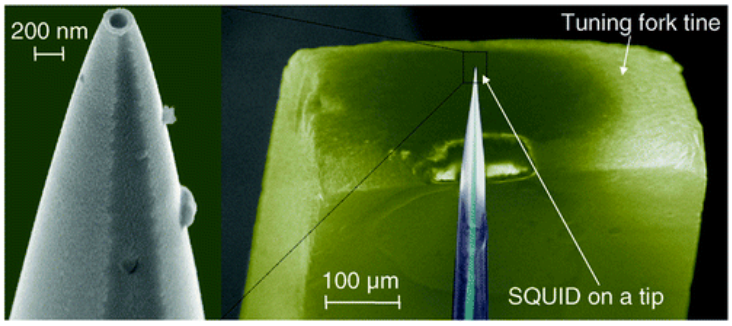

Figure 3.7: Left: SQUID on a tip (refer to text for details of the fabrication process), Right: SQUID on a tip glued on a prong of a tuning fork, from [71].

In contrast to a lithographic process this allows for a smaller SQUID/sample distance as the SQUID is at the apex of a quartz tube. These SQUIDs are non-hysteretic, the critical current modulates in the order of 2.5 µA.

An interesting feature is that the quantum oscillations can be observed up to 0.5 T. This is due to the fact that the evaporated aluminum leads are oriented in field direction making them less sensitive to the field.

The sensitivity is given between $3 \times 10^{-5}\Phi_0/\sqrt{\text{Hz}}$ and $1.8 \times 10^{-6}\Phi_0/\sqrt{\text{Hz}}$.

The group also uses tuning forks with its SQUID-on-a-tip design to make topographic and magnetic imaging.

We estimate it difficult to use this kind of SQUID design for a scanning microscope as the SQUID is unprotected and can easily be damaged during a scan.

3.4 High speed scanning SQUID microscopy

In chapter 2 future improvements of the microscope were discussed. All of these improvements are being worked at the time of writing. In this section, I want to discuss a new measurement scheme I came up with during this thesis that allows for high speed scanning of a flat sample, but is not being actively pursued at the moment.

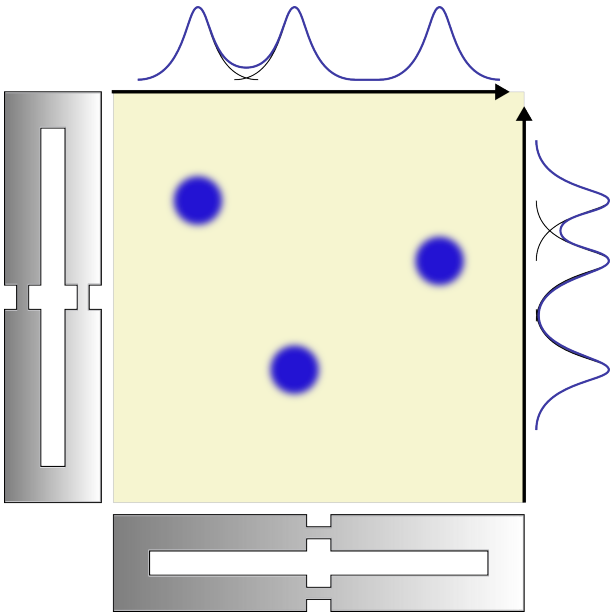

Figure 3.8: New high speed SQUID scanning scheme: By scanning alternately vertically and horizontally with two different SQUIDs it is possible to deduce the position of vortices. The vortex profiles on the right side and on the top correspond to the signal from the vertical and horizontal scan, respectively.

Figure 3.8 shows a new SQUID tip design consisting of two lengthy, orthogonal SQUIDs. As the design suggests each SQUID would have either a high horizontal spatial resolution and a low vertical one or vice versa. If one scans first from left to right and back and then vertically it would be possible to deduce the field distribution above the sample surface by considering the correlation between the vertical and horizontal measurement. This is illustrated in figure 3.8. The correlation would only exist in the case where the time between the vertical and horizontal scan is smaller than the temporal magnetic variation, i.e. vortex movement.

The main advantage of this technique is the improved scanning speed. Depending on the SQUID size (and thus the spatial resolution) it would be possible to scan an area of 50 by 50 microns in the order of seconds. In the case of a lower spatial resolution this time could be increased to video frame rates.

This measurement scheme is very demanding and challenging: It needs a very flat surface and a way to perfectly align the SQUIDs parallel to the surface (maybe by using 3 STM tips). Either the SQUID would have to be protected by photoresist or the approach and scanning procedure would have to be extremely careful. One can imagine to first approach and measure the tunneling current of the three tips simultaneously. Once a threshold is exceeded by one of the tips the approach is stopped and the tilting angle is changed in order to have the same tunneling current at all three tips. Then the alignment and the height of the tip would allow for parallel scanning of very flat surfaces.

4
Rhenium

In this chapter we discuss measurements on Rhenium. Rhenium is a conventional superconductor that can be grown epitaxially on sapphire (α-Al_2O_3). The lattice parameters of rhenium and α-Al_2O_3 are very close with 0.276 nm and 0.277 nm, respectively. In our case the film thickness is 80 nm. Our measurements give an estimate for the pinning forces of the vortices, the absolute value of the temperature dependence of the penetration depth and a rough measure of the second critical field.

4.1 Introduction

The motivation for characterizing rhenium is that it can be grown epitaxially and thus can be used to fabricate very high quality Josephson junctions. Another practical advantage is that rhenium does not oxidize. Supposed two level systems within a junction coupled to a qubit can lead to faster decoherence of the qubit. The aim of current research [73] is to better understand the origin of these two level systems and to suppress their effect. The granularity of evaporated films used to fabricate the SQUIDs and atomic defects in the S-I-S josephson junctions are suspected to be their origin. The defects lead to charge, critical current or flux noise.

This research is done in the context of the ongoing project SuperNanoCharac supported by the NanoScience Foundation (Grenoble, France).

The sample at hand was fabricated using Molecular Beam epitaxy under UHV conditions by B. Gilles and M. Verdier at the SIMAP INPG laboratory. It consists of a 80 nm rhenium film on a sapphire substrate.

The surface rugosity of the rhenium film was already characterized using scanning tunneling microscopy. The measurements were performed by Thomas Dubouchet in the group of Claude Chapelier at the CEA Grenoble. Two topographic images are shown in figure 4.1: In image (a) one can clearly see the atomic terraces. The surface rugosity is over an area of 2 μm by 2 μm is about 5 nm (RMS), see (b). The measurements also found a coherence length of $\xi = 24$ nm.

The following sections summarize the measurements and results obtained with our scanning SQUID microscope.

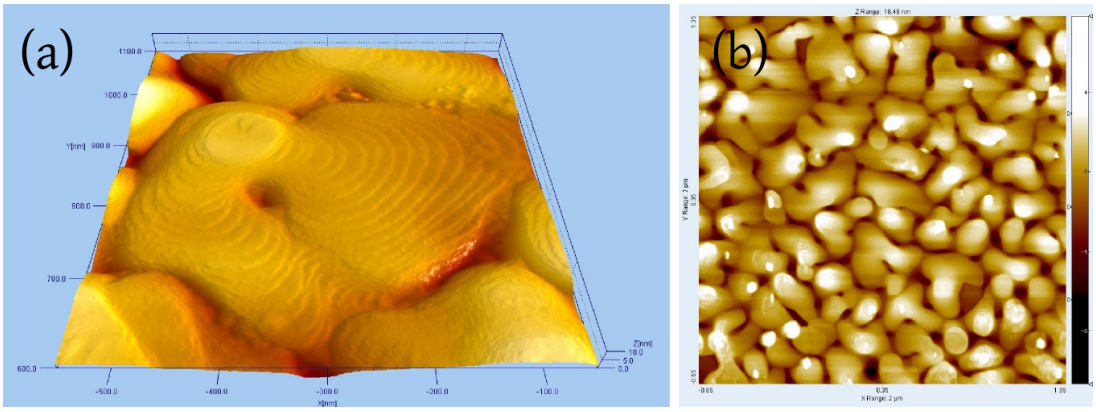

Figure 4.1: Topographic images of a rhenium film. (a) 500 nm by 500 nm (z-scale 10 nm): Notice the atomic resolution (terraces). (b) 2 µm by 2 µm. The size of the topographic features is about 150 nm. The same film was used for scanning SQUID microscopy. Measurements performed by Thomas Dubouchet.

4.2 Vortex penetration

In a type II superconductor vortices enter the sample volume if the applied magnetic field exceeds the first critical field. In superconducting thin films of type I superconductors show a second order transition: the system establishes a vortex state as the cost in energy to pay decreases due to the decreasing interface between the normal vortex core and the superconducting sample volume (see discussion in section 1.3.4). This transition from a type I to a type II behaviour appears when the film thickness decreases below the critical thickness d_c [74] given by

$$d_c \approx \frac{\xi - \lambda}{(1 - 2\kappa^2)^2} \tag{4.1}$$

with k being the Ginzburg-Landau parameter λ/ξ. The lack of bulk measurements for λ makes it impossible to calculate the critical thickness for rhenium, but typically the values are of the order of 1 µm [74].

By using the results of this chapter - notably $\lambda(T = 0) = 79$ nm we can try to evaluate the bulk penetration depth using $\lambda_\perp = \lambda_{eff}^2/d$ (d being the thickness of the film and $\lambda_{eff} = 79$ nm). But this formula is only valid in the $d \ll \lambda_{eff}$ limit, not being the case here (d=80 nm). This leads to a penetration depth of 78 nm, still being larger than $\xi = 24$ nm and thus equation 4.1 cannot be used to obtain the critical thickness.

As the applied magnetic field is increased, more and more vortices enter the sample from the border and thus the vortex density at the border increases. Once a threshold is exceeded the vortex system relaxes by pushing some of the vortices deeper into the sample and thus stabilizing the density at the border. In other words, at a certain "field pressure" the vortices move in an avalanche towards the sample center. For superconductors with strong vortex pinning this behaviour is part of the Bean-model [75], leading to a constant vortex density gradient. The vortex movement can be measured with our scanning SQUID microscope in the following way:

If we position the SQUID above the sample, we can measure the I_c over $H_{applied}$ characteristics of our SQUID. This is normally used to calibrate the SQUID. The sample has to be in the normal state for the calibration.

If however the sample is deeply in the superconducting state ($T \ll T_{SC}$) the sample screens the magnetic field, thus we cannot use the resulting I_c over $H_{applied}$ for calibration since there are jumps in the characteristics. These jumps are due to variations of the vortex density in the vicinity of the SQUID as described above. In figure 4.2 the I_c vs H curves are depicted.

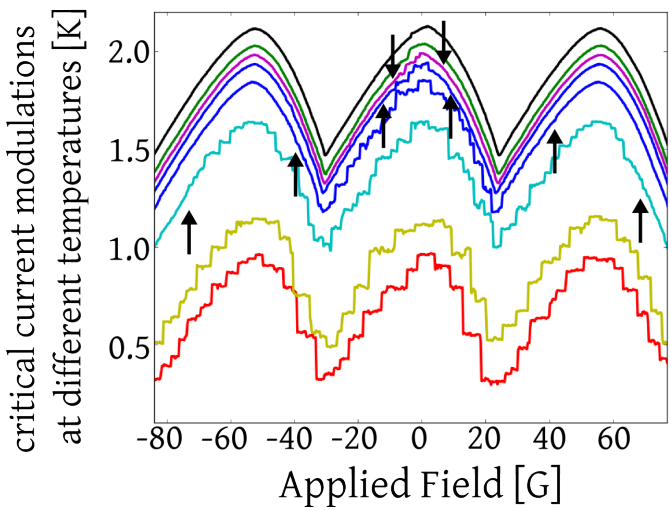

Figure 4.2: Critical current modulations of our SQUID at different temperatures over applied field characteristic. The characteristics were measured at 300 mK, 500 mK, 1 K, 1.2 K, 1.3 K, 1.35 K, 1.4 K and 1.5 K. The jumps in the curves at lower temperatures are due to vortex avalanches, whereas above and close to the critical temperature of the sample we obtain the typical field dependence of the SQUID's critical current.

The closer the sample temperature is to T_{SC}, the smaller are the fields differences that lead to a relaxation of the vortex system because of the decreasing pinning and the increasing vortex interaction. The reason for this is that the coherence length increases beyond the size of the sample defects and thus pinning becomes weaker. Vortex interaction becomes more important at higher temperature, because the penetration depth also increases with temperature. Both effects reduce the "field pressure" needed to trigger an avalanche. Figure 4.3 shows the average field variation needed to trigger avalanche events as a function of temperature.

As the second critical field H_{c2} of the sample decreases when approaching T_{SC}, the field range in which the vortex avalanches appear are more and more constrained, because the screening becomes weaker and weaker and thus the jumps on the $I_c(H)$-curve fade out, making it difficult to determine the field H_{jump} at which the jumps finally disappear. H_{jump} is indicated by arrows in figure 4.2. Because of the fading out we estimate that H_{jump} underestimates H_{c2}. In figure 4.4 $H_{jump}(T)$ are shown and linearly fitted. The fit leads to a critical temperature of 1.35 K±0.05 K. This is slightly off the value measured by STM and results from the underestimating of the second critical field. The discrepancy is quite close to similar measurements performed on an aluminum film by the same technique in our group [76].

4.3 Vortex pinning

We continue by discussing vortex pinning of single vortices in more detail. In contrast to the last section we do not discuss avalanches due to exterior forces (applied magnetic field), but vortex movement due to the fact that the measuring probe (SQUID) is interacting with the vortices. The competition between this SQUID/vortex interaction and the vortex pinning force gives us the possibility to estimate the latter. In order to do so, we first have to model the force acting on a vortex by our SQUID.

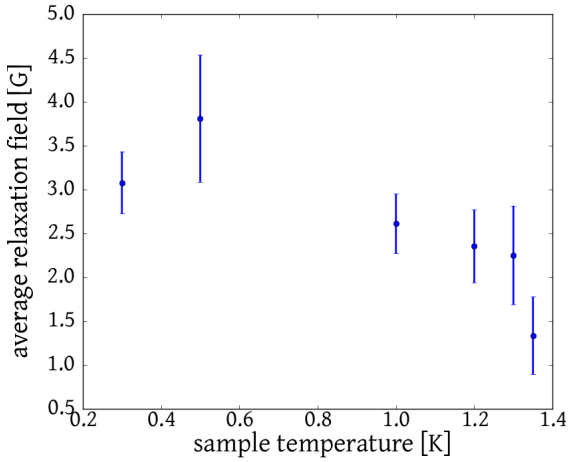

Figure 4.3: Relaxation field vs. temperature. The relaxation field corresponds to the field variation that triggers vortex avalanches. Due to weaker pinning and bigger inter-vortex interaction a smaller field variation is needed with increasing temperature.

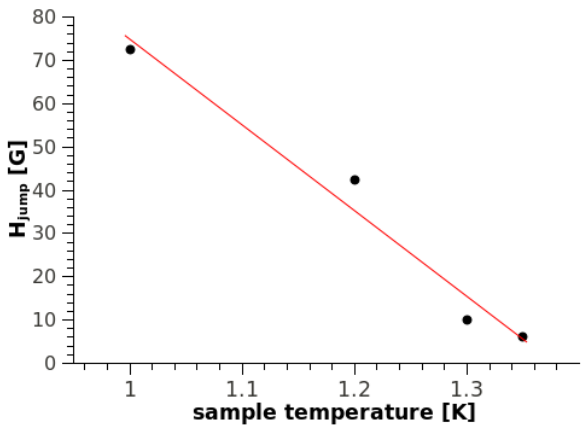

Figure 4.4: The second critical field can be approximated by using the H_{jump} field. Once the latter is exceeded no vortex avalanches are observed thus representing a lower bound for H_{c2}. For more details refer to text.

4.3.1 SQUID/vortex interaction

Loop - Model In this section we develop a crude model for the SQUID/vortex interaction. For this model we consider the SQUID and the vortex as simple current loops acting on each other (see figure 4.5). The current along the square SQUID loop and the vortex is I_{SQUID} and I_{vortex} respectively.

In order to calculate the force on the vortex due to the SQUID, one can make use of the Biot-Savart's law

$$\mathbf{B} = \int \frac{\mu_0}{4\pi} \frac{I\mathbf{dl} \times \mathbf{r}}{|r|^3} \tag{4.2}$$

with $\mathbf{r}/|\mathbf{r}|$ being a unit vector pointing from the wire element $\mathbf{dl}$ to the position of the magnetic field $\mathbf{B}$ being calculated. In conjunction with the Lorentz force, this leads to:

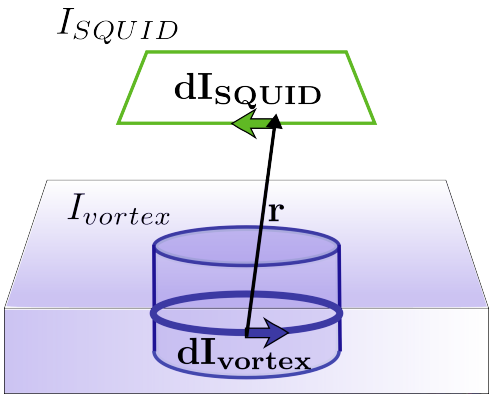

Figure 4.5: Illustration of the model: we consider the force by square SQUID loop on a vortex represented by a current-loop. For details see text.

$$\mathbf{F_{SQUID/vortex}} = -\frac{\mu_0}{4\pi} I_{SQUID} I_{vortex} \oint_{\text{SQUID-loop}} \oint_{\text{vortex-loop}} \frac{\mathbf{dl_{SQUID}} \times \mathbf{r} \times \mathbf{dl_{vortex}}}{|r|^3} \tag{4.3}$$

In order to calculate the resulting force a finite element method integration is used. For this the vortex loop and the SQUID square are divided into finite elements and the integral is calculated by summing up their contributions.

The radius of the vortex loop r_{vortex} is calculated by taking into account the current distribution of a vortex given by

$$J_s = \frac{\Phi_0}{2\pi\mu_0\lambda^3} K_1(r/\lambda) \tag{4.4}$$

with r denoting the distance to the vortex axis and K_1 being the first-order modified Bessel function. Furthermore, we also take into account the cut-off of the screening current at a distance ξ from the vortex core. This yields $r_{vortex} = 125$ nm in the case of $\lambda = 80$ nm.

Results In figure 4.6 the maximal force acting on a vortex while scanning as a function of the SQUID/sample distance is depicted. The vortex radius was chosen 125 nm, the SQUID size 1000 nm, the vortex current 1 mA and the SQUID current 50 µA. The maximal force is attained when one arm of the SQUID is above the vortex and is obtained by using figure 4.6 showing the force acting on a vortex as a function of lateral SQUID position (during the scan).

For the aforementioned parameters we obtain a force acting on the vortex of $F = 3.9 \times 10^{-16}$ N at a SQUID/sample distance of 750 nm.

Limitations The model described above gives us a good order of magnitude estimate of the SQUID/vortex interaction. Especially in the case of thin films d and SQUID/sample distances h with $h \gg d$ a sole current loop can represent a vortex. Nevertheless future numerical simulations should also take into account the current distribution of the vortex and the finite thickness of the SQUID arms.

A model proposed by B. Kalisky [77] calculates the force on a vortex due to a pickup loop by solving the London equations at the surface of a superconductor by using Fourier transforms. In the model the superconductor is considered to be semi-infinite. The screening currents can be calculated by the Maxwell equation $\mathbf{J} = \nabla \times \mathbf{H}$, while the Lorentz force can be determined using

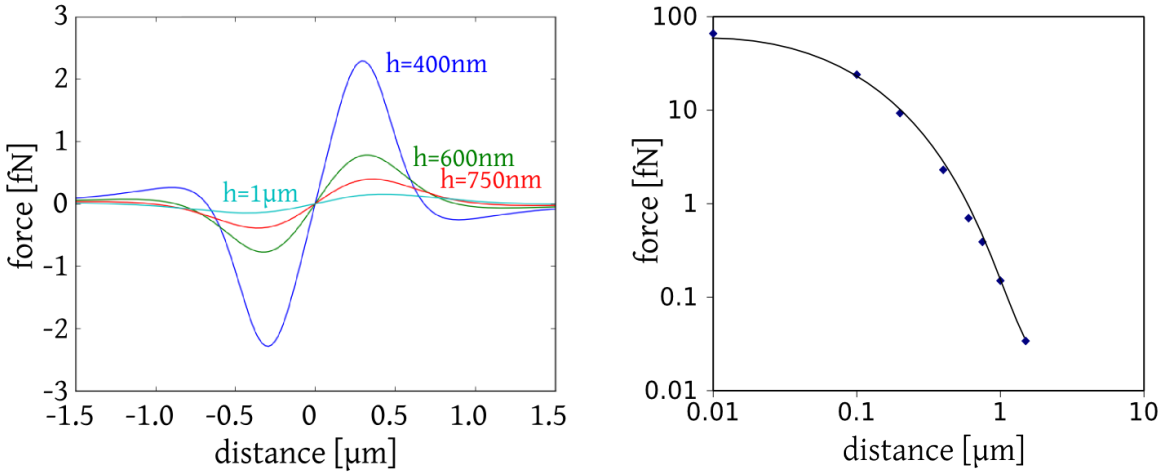

Figure 4.6: Left: SQUID/vortex interaction over the lateral SQUID position. The different curves correspond to different SQUID/sample distances. Right: Maximal force (as obtained by the left figure) over SQUID/sample distance. The solid curve is a guide to the eye.

$$\mathbf{F} = \Phi_0 \int_{-\infty}^{0} \mathbf{J} \times \mathbf{z} dz \tag{4.5}$$

with z being the unit vector parallel to the vortex axis. As the force is integrated along the length of the vortex, the force acting on a thin film vortex is overestimated in this model.

The lateral force on a vortex is given by:

$$F_r(r) = -\frac{\Phi_0 I_{SQUID} r_{SQUID}}{\lambda^2} \int_0^{\infty} dk \frac{k \exp -hk}{q(q+k)} J_1(k r_{SQUID}) J_1(kr) \tag{4.6}$$

with r_{SQUID} and I_{SQUID} denoting the SQUID's radius and current, $q = \sqrt{\lambda^{-2} + k^2}$ and h the height of the SQUID loop above the sample surface.

For our parameters, we obtain a force at a height $h = 750$ nm and thus a pinning force of 6×10^{-15} N, being more than one order of magnitude higher than the value obtained by our simple model[1]. As this model overestimates the force acting on the vortex it can be used as an upper bound in conjunction with our simple model based on two current loops.

4.3.2 Pinning force estimation

To summarize, we have shown that the SQUID/vortex interaction depends on their distance. By changing the height of the SQUID w.r.t. the sample surface we were capable of either interacting with vortices and make them move during a scan (see figure 4.7), or to weaken the interaction so that the vortex position in two successive images stays the same. The critical height was found to be $h = 750$ nm.

For this measurement we have moved to a sample region without strong pinning centers. By numerical simulations we obtain a pinning force of $F = 3.9 \times 10^{-16}$ N.

[1]The source code for this calculation was kindly provided by Beena Kalisky.

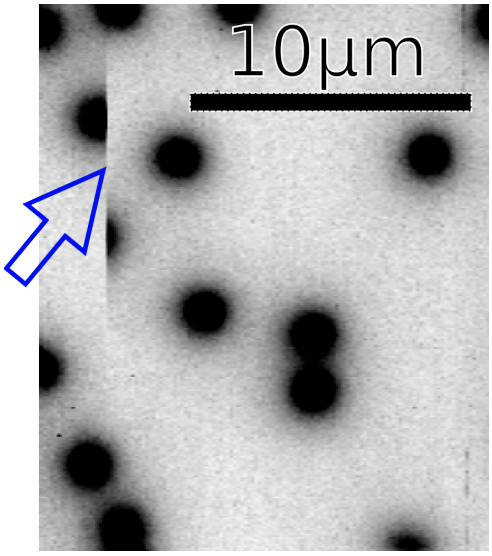

Figure 4.7: Image showing a vortex moving while being scanned (see arrow).

4.3.3 Comparison

Table 4.1 summarizes pinning forces in different materials, measured by different techniques.

Table 4.1: Vortex pinning forces in different materials determined with different techniques

compound	technique	pinning force [pN/µm]	reference
$Ba(Fe_{0.95}Co_{0.05})As_2$	MFM	0.45 - 1.8	[78]
Niobium	current ramp, SQUID detection	370 - 450	[79]
Niobium	MFM	15 - 40	[65]
Rhenium	SSM	0.005	this work

Under the assumption that pinning is a bulk effect, one can normalize the pinning force by the vortex length (film thickness). For our measurements this leads to 0.005 pN/µm. In comparison to other materials used for superconducting devices, the pinning force is by three orders of magnitude weaker. As mentioned before, we measure the minimal pinning force, thus we underestimate the average pinning force.

The SQUID/vortex interaction was not yet observed with the SQUIDs/tips used in our group. The reason for this low pinning is certainly due to the fact that the rhenium film was grown epitaxially and not by evaporation as it is done for niobium films. Thus it is a single crystal, in constrast to polycrystalline niobium which grows as an ensemble of grains with sizes of the order of nanometers which act as good pinning centers.

As we have mentioned above, measuring the vortex pinning in pN/µm implies that the pinning is due to the sample volume and not to the sample surface. With our measurement we cannot corroborate or refute this hypothesis. It should be noted however that the rugosity of the sample was determined to be $\sim$ 5 nm compared to a thickness of 80 nm. This means that the surface contribution should not be neglected in this case. Furthermore, it can be argued that, based on the fact that epitaxial growth should result in less volume defects, the surface contributes significantly to the pinning.

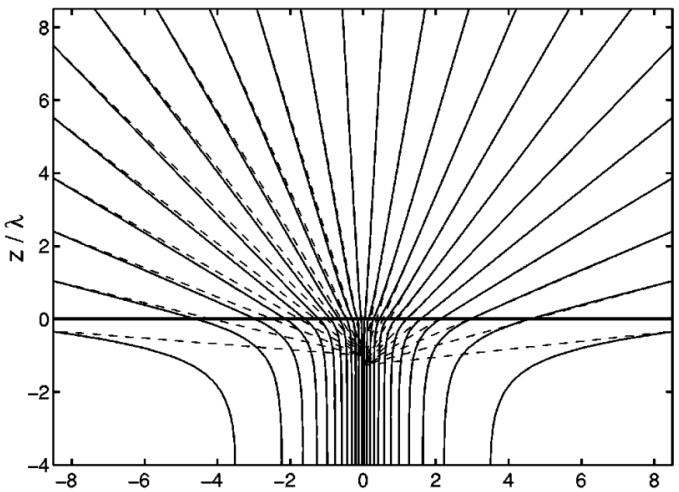

Figure 4.8: Field lines of a vortex spread close to the sample surface. The dashed lines on the left side correspond to a magnetic monopole with the flux $2\Phi_0$ (to compensate the flux in negative z direction) at λ beneath the surface. The dashed lines on the right side correspond to a monopole at $z = -1.27\lambda$ which fits better the numerically calculated field lines, from [91].

4.4 Penetration depth measurements

4.4.1 Introduction

One challenge when characterizing a new superconductor is to determine its two characteristic length scales ξ (coherence length) and λ (penetration depth). For the former there exist the scanning tunnel microscopy technique [80] or estimates using the slope of the H_{c2}-curve in the phase diagram [30]. For the latter, measurements of the variation of λ using a radio-frequency tunnel diode oscillator circuit are common [81]. To obtain absolute values one can use microwave techniques [82], NMR [83] or scattering techniques (muons [84] or neutrons [85]). One general problem of scattering techniques is statistics: one needs a high flux of either muons or neutrons, a big sample and a high vortex density (thus high fields). The vortices have to be arranged in an almost perfect lattice in order to read λ out from the data by subtracting the background.

The penetration depth is the characteristic length scale describing the magnetic properties of a vortex. By measuring the flux distribution above a vortex, one can determine the penetration depth by fitting the cross-section of this flux distribution to a model function. Naturally, this model function depends on λ, but also on the height h at which the flux was measured. In the course of history, several model functions for the magnetic field distribution were proposed.

In 1966, J. Pearl calculated the current distribution of an isotropic vortex deep inside the sample and at the sample surface, noting that the inter-vortex interaction is dominated by their interaction close to the surface [86]. This is due to the opening of the vortex at the surface (see figure 4.8). Once experimental techniques to probe the field distribution of a vortex became available, other models were proposed. J. R. Clem calculated in 1975 the form factor of vortices for neutron scattering purposes using GL theory [87]. Once scanning Hall-probe techniques became available (Hess et al. [88] [89]), more general approaches for calculating the field above a vortex for the anisotropic case and for an arbitrary sample thickness where proposed by V. G. Kogan [90] and E. H. Brandt [91].

We now briefly outline the general approach used to calculate the field above a vortex using its cyclindrical symmetry. The main idea is to calculate the magnetic field in the vacuum by using

the Maxwell equations and to use the London equations for the magnetic field in the interior of the sample. By using the Fourier transform for both fields at the vacuum/sample interface and imposing continuity of the field and its normal derivative, one obtains [92]:

$$h_z(\mathbf{r},z) = \frac{\Phi_0}{(2\pi\lambda_{ab})^2}\int d^2\mathbf{k}\exp(i\mathbf{kr})\frac{\exp(k(d/2-z))}{\alpha(\alpha+k\coth(\alpha d/2)} \tag{4.7}$$

with $\mathbf{k} = (k_x, k_y)$ and $\alpha = \sqrt{k^2+\lambda_{ab}^{-2}}$. λ_{ab} corresponds to the in-plane components of the penetration depth and d denotes the sample thickness. Note, that the sample is centered at $z = 0$, so that the height above the sample plane can be written as $h = z - d/2$. The vortex is situated at the r-axis.

The model supposes $\lambda \gg \xi$. For superconductors which do not fulfill this condition, this approximation leads to a systematic different shape of the field distribution [93]. Thus the model has to be expanded to include also cases in which this approximation is not valid.

In order to use this magnetic field distribution function for our fit, we have to convolute it with the SQUID-loop shape, subtract the background of our measurements and center the vortex at $r = 0$.

In the late 1990s, scanning SQUID microscopy was first used by J.R. Kirtley *et al.* to obtain the penetration depth for anisotropic (ellipsoid) vortices with a penetration depth of λ_{ab} of ~18 µm along the major semi-axis [94]. For this experiment a pick-up loop with a diameter of ~8.5 µm was used. λ was determined using equation 4.7 and fitting it to a vortex profile.

In order to determine λ one has to estimate the SQUID/sample distance h very precisely, because the two are anti-correlated as can be seen by the $\lambda + z$-term in the following equation [89] being a first order approximation of equation 4.7 of the z component of the magnetic field above the center of a vortex:

$$h_z = \frac{\Phi_0}{2\pi}\frac{z+\lambda_{eff}}{[r^2+(z+\lambda_{eff})^2]^{3/2}} \tag{4.8}$$

d is the sample thickness and $\lambda_{eff} = \lambda\coth(d/2\lambda)$ is the effective penetration depth taking into account the sample thickness. In the case of a thin film $d \lesssim \lambda$ the effective penetration depth λ_{eff} is larger than λ because the vortex opening at the two opposite sides of the film overlap. For a sample being much thicker than λ, λ_{eff} equals λ. In the next section we are going to explain one practical solution to determine λ precisely by fitting equation 4.7 with two free parameters z and λ.

4.4.2 Confidence region

Because the importance of a reliable error estimate for the penetration depth, we have put a lot of effort into the determination of its uncertainty. One technical difficulty arises from the fact that the two free parameters appear non-linearly in the fitting function. In order to obtain their uncertainty despite this fact we will introduce the confidence region method.

The quality of a fit can be measured by using χ^2 defined as:

$$\chi^2 = \sum_{i=1}^{N}\left(\frac{\Delta y_i}{\sigma_i}\right)^2 \tag{4.9}$$

with Δy_i being the error between the fit and the i-th data point and σ_i its standard deviation.

Conventionally, functions are fitted by the Levenberg-Marquandt algorithm in order to find the best fitting parameters by minimizing χ^2. To estimate the error bar of each parameter the diagonal

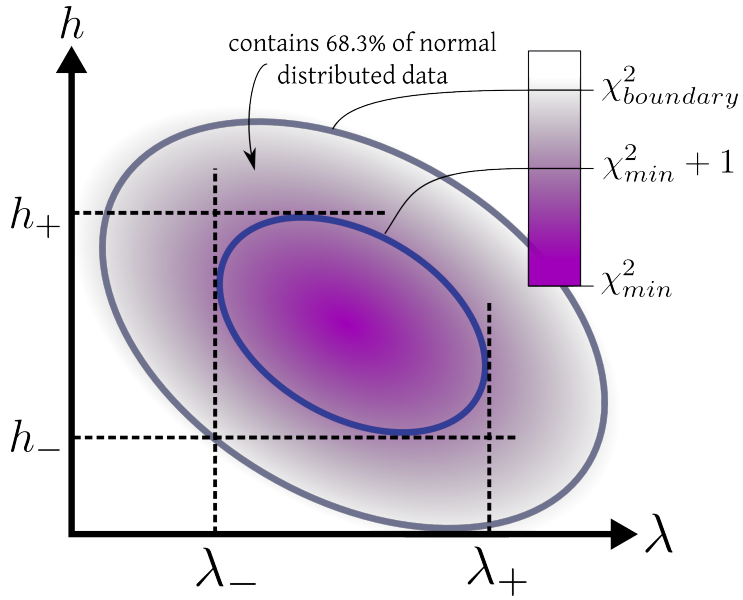

Figure 4.9: Illustration of a confidence region: the color corresponds to $\chi(\lambda, h)$. The minimum is found at the center. The bigger ellipse corresponds to the confidence region with a confidence level of 68.3%. The smaller ellipse corresponds to $\chi^2_{min}+1$ and its projections to the confidence intervals (68.3%) of the parameters. For further details refer to the text.

elements of an estimated covariance matrix are used as the standard deviation vector σ (each component corresponds to one fitting parameter). There are two shortcomings to this method: the covariance matrix is only estimated leading to wrong uncertainties and the fact that correlations between fitting parameters are not taken into account by only considering the diagonal elements. In general, this leads to an underestimation of σ.

A **confidence region** is a region in the parameter space (in our case two-dimensional) in which the probability to find the true parameter values is, i.e. 90% (confidence level). It can be obtained with the help of χ^2: first one has to find the parameter combination (λ_{best}, h_{best}) which minimizes $\chi^2(\lambda_{best}, h_{best}) = \chi^2_{min}$. Then one defines $\chi^2_{boundary} = \chi^2_{min} + k$ that gives the boundary of the confidence region; k depends on the confidence level and on the number of fitting parameters. For a confidence level of 68.3% in our two-dimensional case $k = 2.3$ (see [95] for details).

In order to visualize the confidence region one has to calculate χ^2 over the whole parameter space and plot the contour of $\chi^2_{boundary}$. This is schematically illustrated in figure 4.9. The projection of the confidence region with $k = 1$ on the parameter axes gives the confidence interval for the parameters (68.3% of normal distributed data inside).

4.4.3 Fitting the vortex profiles

As the scanning height and the penetration depth are strongly correlated, the confidence region is extremely narrow and long making the method essentially useless in our case. The correlation can be seen in figure 4.10(b): the color corresponds to the $\chi^2(\lambda, h)$. The dashed line $h(\lambda^*)$ (with $\frac{\partial \chi^2(\lambda^*)}{\partial \lambda} = 0$) represents the valley of $\chi^2(\lambda, h)$.

A remedy for this correlation is to use an additional constraint like the SQUID/sample distance h as a mean to reduce the possible values for λ. The SQUID/sample distance was determined to be 450 nm ± 70 nm. By truncating the confidence region one can obtain useful results for the penetration depth based on the field profile above a vortex. A typical fit of a vortex is shown in figure 4.10(a).

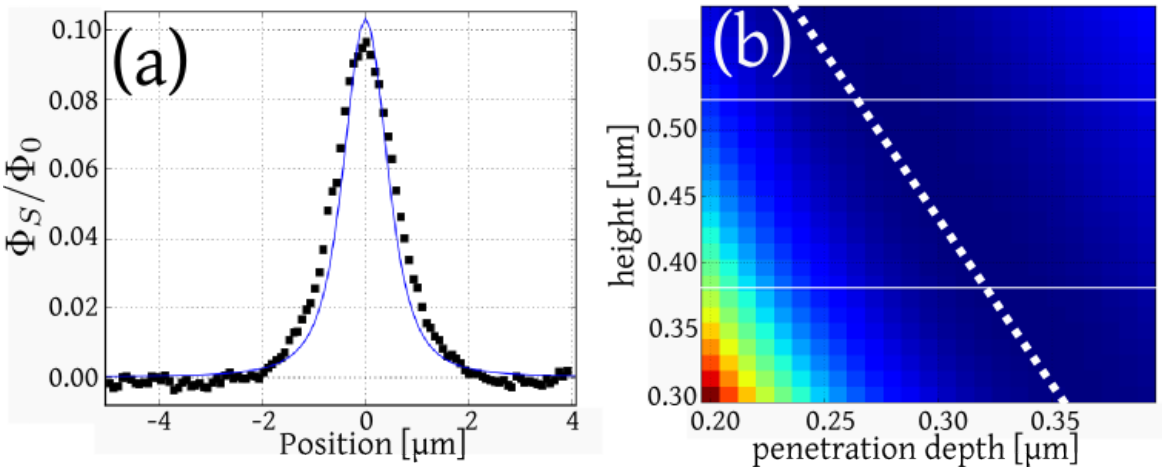

Figure 4.10: (a) typical fit of a vortex profile (vortex at 600 mK with $\lambda = 73.5$ nm, (b) χ^2-plot of the vortex with the highest penetration depth of 308 nm. The dashed white line corresponds to good fit parameter combinations. The region between the two horizontal white lines limit the possible SQUID/sample heights (determined experimentally).

In figure (b) the correlation between h and λ is represented by the dashed line. The two parallel lines contain possible values for the SQUID/sample distance and give us a mean to determine the uncertainty of the penetration depth.

The penetration depth of the rhenium film as a function of temperature is given in figure 4.11.

The first proposed temperature dependence of the penetration depth was given by Gorter and Casimir based on the two- fluid model: $\lambda(T) = \lambda_0(1-(T/T_{SC})^4)^{-1/2}$ [30]. However, this model underestimates the penetration depth. By solving the full BCS equations the exponent of the reduced temperature becomes 2 for an s-wave superconductor [96]. This second model is valid for temperatures above $0.35T_{SC}$.

To fit the two models to our data only λ_0 was used as a free parameter, while T_{SC} was determined by measurements to be 1.6 K. By fitting the theoretical evolution to the measured penetration depth at different temperatures of 32 vortices, we are able to determine λ_0 to be 61 nm $\pm$ 2 nm (for the first model) and $\lambda_0 = 79$ nm$\pm$3 nm for the second model which fits our data better than the Gorter-Casimir model.

The bulk penetration depth of rhenium is not known, but we will give a crude estimate in the following to compare our thin film result with. Rhenium grows in a hexagonal lattice (volume of a unit cell: 29.41 Å^3, two atoms per unit cell[2]). By counting only the outer-most electrons (d-shell), we get 10 electrons per unit cell. If we use

$$\lambda^2 = \frac{m}{\mu_0 n e^2} \tag{4.10}$$

and plug in the free electron mass for m and 10 electrons per volume of the unit cell, we obtain a penetration depth of $\lambda = 13$nm ($\mu_0 = 4\pi \cdot 10^{-7}$, e being the electron mass). With an coherence length of 27nm, this makes rhenium a type I superconductor which becomes type II in a thin film configuration.

[2]data from: *http://webmineral.com/data/Rhenium.shtml*

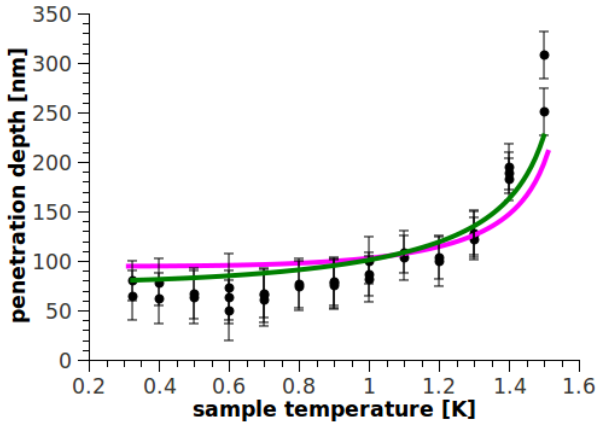

Figure 4.11: Temperature dependence of the penetration depth of the 80 nm thick rhenium film. The pink solid curve is a fit with $\lambda_0(1-(T/T_{SC})^4)^{-1/2}$ which yields $\lambda_0 = 61$ nm. The green curve ($\lambda_0(1-(T/T_{SC})^2)^{-1/2}$) fits the data for a $\lambda_0 = 79$ nm.

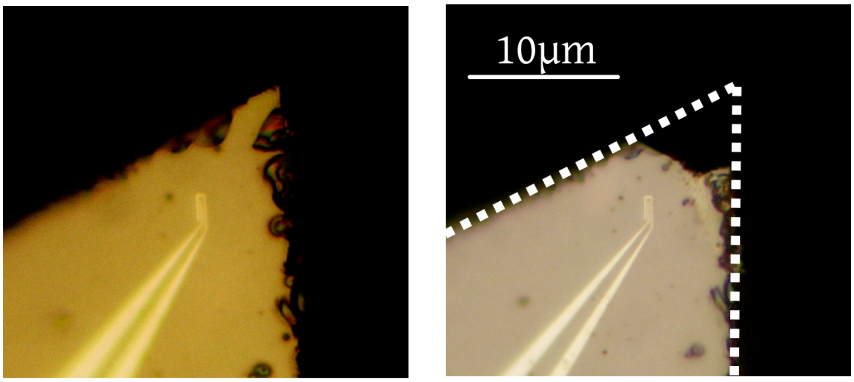

Figure 4.12: Left: the tip before the cool-down. The SQUID/sample distance is estimated to be 750 nm. The SQUID size is 600 microns. Right: the tip after 4 weeks of scanning. The estimated SQUID/sample distance with this tip is 450 nm

4.5 Tip abrasion

As has been discussed in chapter 2 the main goal of our AFM regulation is to make it possible to scan with the same SQUID tip for several weeks. The measurements discussed in this chapter were performed during one month.

In figure 4.12 the states of the tip before and after the measurement are depicted. As one can see the tip is damaged, but the SQUID is still intact. As we have deduced from the evolution of our images the SQUID/sample distance did not change gradually but from one image to the next, indicating that the tip broke off as a result of one mechanical accident.

4.6 Conclusion

In this chapter the SQUID/vortex interaction was discussed. We have given an estimate for the vortex pinning force in a homogeneous sample region and shown that it is at least two order of magnitudes weaker than for niobium samples.

Furthermore, this experiment showed that we are capable of deducing the penetration depth of a

superconductor by fitting the flux profile above a vortex.

Finally, we also showed that it is possible to scan several weeks with our microscope. This is due to the soft regulation developed during this thesis and to the fact that as the SQUID is not positioned at the AFM tip. The SQUID is therefore protected, in contrast to the proposition of a SQUID on a tip (Zeldov group, see chapter 3).

5

Unconventional superconductivity in UCoGe

5.1 Introduction

In chapter 1 we focused our attention on conventional superconductivity satisfying the requirements for understanding the experimental setup described in chapter 2. Now, we will go beyond this scope and give a brief introduction of unconventional superconductivity: its definition, several families of unconventional superconductors and different aspects, in particular superconductivity with magnetic ordering and domain behaviour, that play an important role in the compound UCoGe.

In the second part of this chapter we discuss measurements already performed on UCoGe and finally - after a short summary - present open questions that will be tackled in the next chapter with the help of scanning SQUID microscopy.

For more detailed introductions please refer to Mineev's textbook [97], [98] (group theory) or [99] (microscopic theories).

5.2 Symmetry of the order parameter

We have seen in chapter 1 that in BCS theory the electrons of a Cooper pair have opposite spins and momenta. When the angular momentum L of a Cooper pair is zero, we call this a *s-wave* symmetry in analogy with atomic physics. In the simplest case the gap is constant and the order parameter is then called isotropic. Anisotropy, however, can lead to nodes of the gap function changing the excitation spectrum considerably. The wave function of a Cooper pair has to be anti-symmetric under particle exchange to obey the Pauli principle, thus:

$$g(\mathbf{k})\chi_{12} = -g(-\mathbf{k})\chi_{21} \tag{5.1}$$

with g and χ corresponding to the orbital and spin part of the wavefunction, respectively.

For an angular momentum of $L = 2$ the order parameter has *d-wave* symmetry and thus two positive and two negative lobes with nodes in between them. These nodes considerably change measurements sensitive to infinitely small excitations. Typically this leads to power law behaviour instead

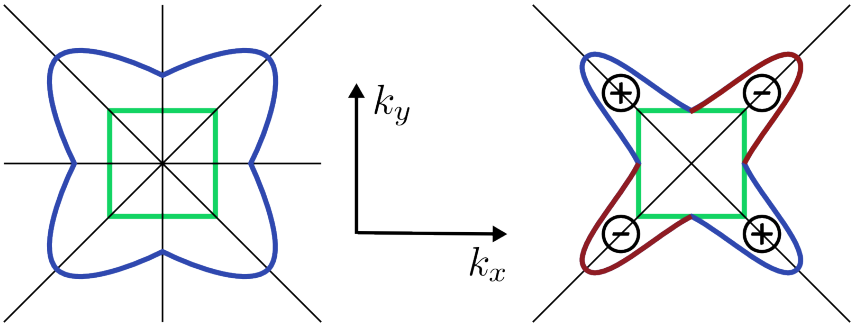

Figure 5.1: The green square represents the Fermi surface (FS). Left: the blue curve corresponds to an anisotropic gap function. As you can see it has the same symmetry as the FS. Right: this time the gap function has d-wave character: four leafs with alternating signs and nodes in between. This is an unconventional superconductor as it is less symmetric than the Fermi surface (notice missing mirror lines).

of exponential ones in heat capacity measurements. Nodes can also appear in anisotropic s-wave superconductors.

As the orbital part of the wave function is even, the spin part has to be odd in order to make the total wave function anti-symmetric. This corresponds to the **singlet state**.

It is theoretically also possible that the electrons of a Cooper pair present equal spin pairing. As a consequence the angular momentum would have to be odd, i.e. $L = 1$. This is called a **triplet state**. In the case of the *p-wave* symmetry the paramagnetic limit does not apply anymore as both electrons have the same spin.

A superconductor is called **unconventional** if the symmetry of its order parameter does not have the full lattice symmetry. In figure 5.1 the Fermi surface and the order parameter for an anisotropic gap function and a d-wave gap function are shown. In both cases nodes of the gap function can exist, but the sign change of the d-wave gap function breaks a supplementary symmetry making it an unconventional superconductor.

One of the two main techniques to distinguish between singlet and triplet superconductivity is to measure the second critical field B_{c2}. If the superconductor obeys the Pauli limit, then the superconductor is singlet, otherwise it is a strong indication for triplet superconductivity.

The second technique is NMR measurements used to measure the Pauli susceptibility of electrons by Knight shift. A singlet-pairing superconductor should have a Pauli susceptibility of zero in all field directions for $T \to 0$, as all electrons at the Fermi level are paired anti-parallel and cannot be polarized. However, in the triplet case the behaviour would be dependent on the field direction making NMR a technique capable to distinguish between singlet and triplet superconductivity.

Note however, that no canonical definition of unconventional superconducitivity exists and that non-phonon mediated superconductivity is also called unconventional in literature.

5.3 Different families of unconventional superconductors

After the success of the BCS theory, superconductivity was considered understood. This changed by the discoveries of heavy fermion superconductors [100], high T_c cuprates [101] and other materials that fall into the class of unconventional superconductors. The following will present some families of unconventional superconducting.

Some **alloys** have very interesting superconducting properties for technical applications: Nb_3Sn

is used for high field magnets [102], some *Chevrel-phases*[1] and *borocarbides*[2] show coexistance of antiferromagnetism and superconductivity. In 2001 it was discovered that MgB_2 becomes superconducting at $\sim$ 40K [105]. It was the first example of a multi-band superconductor.

In 1979, Steglich *et al* discovered that $CeCu_2Si_2$ becomes superconducting beneath 0.5K [100]. The effective mass in this material is $\sim$ 100 times bigger than the free electron mass, hence the name **heavy fermion system**. We will discuss heavy fermions in more detail later on.

W.A. Little postulated in 1964 the possibility of synthesizing **organic** materials with high superconducting transition temperatures [106]. Bechgaard salts and tetramethyl-tetraselenafulvalen [107] were the first examples. Nowadays, superconductivity is also confirmed in fullerenes [108], nanotubes [109], diamond and other carbon compounds.

Before the discovery of superconductivity in LaBaCu0 ($T_{SC} \sim 25$ K) by Bednorz and Müller in 1986 [101], **oxides** were not believed to be candidates for high transition temperatures. Paul Chu *et al* found YBaCu0 with a T_{SC} of 93K (above the boiling temperature of nitrogen) [110]. Producing wires out of these ceramics proved to be difficult and thus they are only rarely used in practical applications.

In 2008 a new class of high temperature superconductors was found by H. Hosono [111]: **iron pnictides**. Up to now, several iron pnictides are known with transition temperatures up to 55K. It was very surprising to find superconductivity in an iron compound, because of its magnetic properties.

The mechanisms leading to superconductivity in most of these superconductors are not yet understood, but magnetic fluctuations seem to play a major role.

5.4 Heavy fermions

In 1979 Steglich *et al* discovered bulk superconductivity in $CeCu_2Si_2$ [100]. The effective mass of the $4f$ electrons is about 100 times larger than the free electron mass due to electron-electron interaction taken into account via the effective mass of quasi-particles (*Fermi liquid theory*).

As a consequence of this increased effective mass the Fermi velocity of the quasi-particles is reduced dramatically. As we have shown in chapter 1 it is important for the phonon mediated Cooper pairing that the electrons move quickly through the lattice to minimize Coulomb repulsion. For a conventional superconductor with s-wave pairing ($L = 0$, $S = 0$) the Coulomb repulsion prevails over phonon coupling. This leads to the conclusion that heavy fermion system superconductivity is unconventional [112] in the sense that another mechanism is responsible for the pairing.

The properties of heavy fermion compounds are due to partly filled $4f$ or $5f$ shells like in the case of cerium or uranium that behave as local magnetic moments. The non negligible tail of their radial probability distribution and the fact of their energy is close to the Fermi energy leads to interactions with the conduction electrons.

At low temperatures a competition between two interactions is taking place: The RKKY interaction between the local moments via the conduction electrons favours long-range order, whereas the spins of the conduction electrons screen the local moments thus leading to short-range order (Kondo effect).

The characteristic energy scale of the Kondo interaction is

$$k_B T_{Kondo} \propto \exp(-\frac{1}{N(E_F)J}) \tag{5.2}$$

[1]Chevrel phases are compounds consisting of molybdenum in the general form $M_x Mo_6 X_8$ (with M being a metal and X a chalkogenid (sulphur, selenium, tellurium)[103]

[2]borocarbides: RM_2B_2C (R represents a rare earth element, M stands for nickel or palladium)[104]

$N(E_F)$ being the density of state at the Fermi level and J the coupling between the spins of the conduction electrons and the local moment. The long-range RKKY interaction's energy can be written as

$$k_B T_{RKKY} = J^2 N(E_F) \frac{\cos(k_F r)}{(k_F r)^3} \tag{5.3}$$

with k_F being the Fermi wave vector defining the oscillations. Because of the oscillating term, antiferromagnetic or ferromagnetic order can be established by this interaction, depending on the distance between two local moment sites.

The competition between RKKY and Kondo interaction was first described by Doniach [113] and can be analysed by quantum phase transitions (QPT): At the so-called quantum critical point (QCP) the system can be driven between one magnetic and one non-magnetic ground state by applying pressure, magnetic field or by chemical doping even at $T \to 0$. These non-thermal phase transitions exist in the zero temperature limit due to the fact that the thermal fluctuations can be neglected in comparison to quantum fluctuations. Close to the QCP new collective states like unconventional superconductivity can appear. After the discovery of the superfluid ^{3}He phases a constructive interplay between magnetism and superconductivity was put forward in the form of magnetic fluctuations [114].

The distance between neighboring f-electron states is crucial for their magnetic order (hence pressure and chemical doping can be used as parameters for tuning the system to a QPT). For the $5f$-states of uranium the different magnetic behaviours as a function of the distance between the uranium atoms d_{U-U} in the crystal were first worked out by Hill [115]: For distances below 3.4 Å the compound is paramagnetic and often also superconducting. The fact that superconductivity appears in these samples is due to the delocalisation of the $5f$ electrons (due to overlap). Because of this delocalisation the local magnetic moment at the uranium site vanishes, strengthening superconductivity. For distances above 3.6 Å the local moments establish a long-range order.

Samples with d_{U-U} in between 3.4 and 3.6 Å (*Hill's limit*) are candidates for coexisting superconductivity and ferromagnetism. We will see later that UCoGe has a inter-uranium distance close to 3.5 Å at ambient pressure. Since 2000, four uranium based compounds were discovered which show coexistence of SC and FM: UGe_2, URhGe, UCoGe and UIr.

The coexistence is surprising because, before the discovery of these compounds, ferromagnetism and superconductivity were considered antagonistic: In $Er_{1-x}Ho_xRh_4B_4$ systems the ferromagnetic transition temperature is around 8.7K and at 1K a spatially alternating ferromagnetic ordering appears [116]. The period of the domain structure is smaller than the coherence length and thus it does not destroy superconductivity. Below 0.8K it becomes energetically favourable to minimize domain walls, thus the period gets larger and superconductivity is destroyed (see figure 5.2). In these compounds superconductivity and ferromagnetism are generally in competition, even though a small doping-range exists where their interplay is constructive [116].

For the aforementioned Chevrel phases the ferromagnetic transition temperature is lower than T_{SC}. In the borocarbides the superconducting transition temperature can be increased by applying an external field that compensates the internal magnetic field (Jaccarino-Peter effect [117]), clearly showing the competition between magnetism and superconductivity.

Two extreme scenarios for ferromagnetism exist. In the first model, localised moments of electrons around their atom are responsible for ferromagnetism. In the other model however, the delocalized conduction electrons are responsible for the so-called **itinerant ferromagnetism**. We will show later on that experimental results indicate itinerant ferromagnetism in the case of UCoGe.

Another important consideration is that conventional superconductivity is insensitive to non-magnetic defects and sensitive to magnetic ones, whereas unconventional superconductivity needs a free

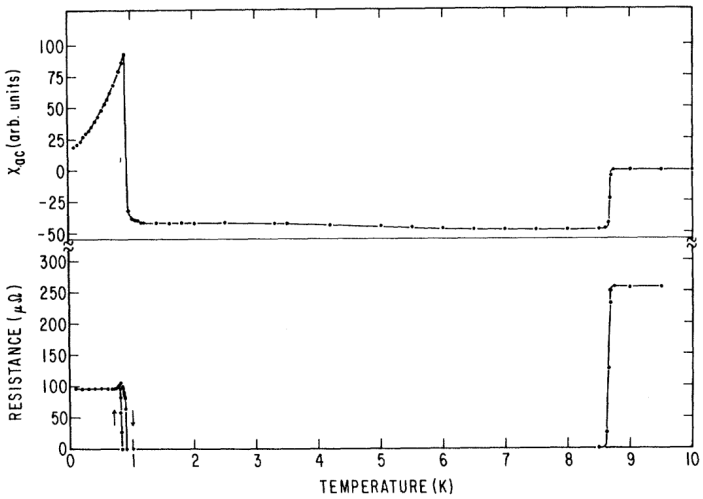

Figure 5.2: Resistance vs. temperature for $ErRh_4B_4$: The compound becomes superconducting at 8.7K. Between 8.7K and 0.8K superconductivity and spatially alternating ferromagnetic order coexist, below 0.8K superconductivity is destroyed by the increased ferromagnetic domain size, from [116].

mean path that is considerably larger than the coherence length ξ (*clean limit*). This explains the difficulty to obtain conclusive results when samples of the highest quality are not yet available.

5.5 Behaviour of magnetic domains in a ferromagnetic superconductor

This section gives a brief summary of reference [118]. The question considered is: how do domains change in a superconducting ferromagnet between the SC/FM and the FM state?

Fauré *et al* consider a thin film superconductor with a high perpendicular magnetic anisotropy. The domains are modelled as stripes of width l (see figure 5.3). The magnetization in each domain is homogeneous and the domain boundary is much smaller than the domain size.

The **domain boundary width** w will be used to minimize the free energy of the system. The width can be determined by minimizing two energy contributions: exchange energy and anisotropy energy. The exchange energy increases when two neighboring moments are not parallel, thus the system tries to increase the domain size to achieve small angles between adjacent moments. The corresponding energy can be written as

$$E_{exchange} = \frac{\Theta}{2aw} \tag{5.4}$$

with a being the inter-atomic distance and Θ the absolute value of the exchange energy between two parallel neigbours.

However, the anisotropy energy[3] prefers to switch directions quickly leading to a narrow domain boundary:

$$E_{anisotropy} = \frac{Kw}{2a^3} \tag{5.5}$$

Once we have deduced the effective domain boundary width $\tilde{w}$ we can calculate the total energy cost of domain boundaries. In order to infere the domain size in the **normal state** one has also to take

[3]origin: interaction between magnetic electron orbits and the electric field of the surrounding ions.

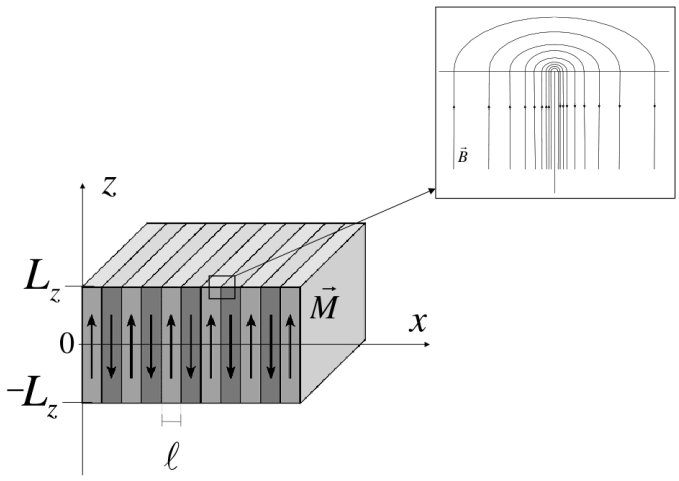

Figure 5.3: Ferromagnetic film with stripe-like domains. The film thickness is $2L_z$. The inset shows the magnetic field distribution close to a domain wall, from [118].

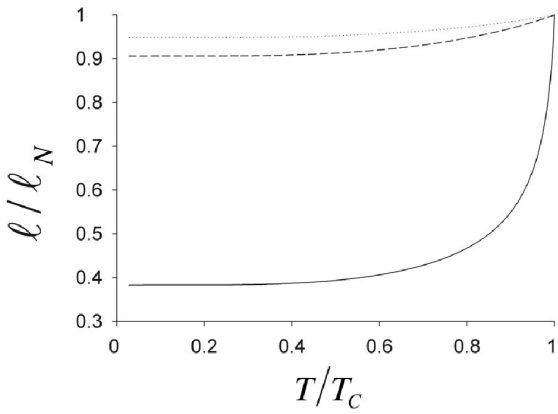

Figure 5.4: The predicted domain size change as a function of temperature for different parameters ($l_N/\lambda(0)$ and $\lambda(0)/w$). For the solid line (0.5 and 100), for the dotted line(0.1 and 100) and for the dashed line (0.1 and 200) were used, from [118].

into account the magnetic energy that prefers small domains in order to minimize demagnetization stray fields. Minimizing the sum of the two energies (boundary and magnetic) leads to the optimal domain size $l_N \propto \sqrt{\tilde{w} L_z}$ ($2L_z$ being the thickness of the film).

For the **superconducting state** we have to consider three energy contributions: magnetic energy (in the ferromagnetic sample and outside), domain energy and superconducting energy (kinetic energy of the supercurrents). In order to calculate the field distribution inside and outside the sample one needs the London equations in the sample volume, the Laplace equations in the vacuum and the continuity condition at the interface. One result is that the magnetic field is screened inside a domain, but not at the domain boundary.

In the general case this problem cannot be solved analytically. Numerical results (for different values of λ, l_N and w) can be seen in figure 5.4.

For the moment we only considered the orbital effect and neglected the spin properties of the Cooper pairs, but the paramagnetic effect is important for temperatures close to T_{SC}. In the case of a **singlet** state the domains become smaller and if the domain wall width is smaller than the coherence length, SC first appears at the domain boundaries.

For **triplet** superconductivity two different order parameters exist for the up and down domains. This leads to two vanishing order parameters at the domain wall, thus increasing the domain wall energy. The increase of the domain wall energy would lead to a larger domain structure, but the corresponding energy is very small compared to the other energy contributions involved and as a consequence it should have no impact on the domain structure.

To summarize, at temperature significantly lower than the T_{SC} the domain structure should become more dense in the singlet and triplet case.

One problem of the above derivation is that the free energy minimization only considers the **equilibrium** and consequently finds the global minimum free energy solution. If the system has to pass over a local maximum to get there, for example because of domain boundary pinning, this approach is too simplistic.

Another aspect not discussed in this model is the behaviour at the **sample boundary** and the dynamics of the domain size change: if domains become smaller, how do new domains enter the sample?

5.6 UCoGe

5.6.1 Introduction

As explained above for the example of $Er_{1_x}Ho_xRh_4B_4$ compounds superconductivity and ferromagnetism are in general antagonistic properties. Recently, however, several uranium based compounds UGe_2, URhGe, UCoGe and UIr were discovered in which SC and FM coexist [119] [120] [121] [122]. Only in URhGe and UCoGe SC and FM coexist at ambient pressure, thus these are candidates for scanning SQUID microscopy.

The coexistence of SC and FM of UCoGe was discovered in 2007 by Huy and de Visser [121]. The crystal structure (TiNiSi, space group P_{nma} is the same as URhGe) is shown in figure 5.5. The lattice parameters are $a = 6.845$ Å, $b = 4.206$ Å and $c = 7.222$ Å. Along the a axis the neighboring uranium atoms form a zig-zag chain. The inter-uranium distance is close to 3.5 Å being in the Hill limit.

This compound becomes ferromagnetic at $\sim$ 2.5 K and superconducting at $\sim$ 0.5 K at ambient pressure (depending on the sample quality). This is the highest T_{SC} among the four uranium based ferromagnetic SC. In the following I want to summarize the results obtained until now on polycristalline and single-cristalline samples.

5.6.2 Sample quality

The measurements discussed in the following where first obtained on poly-crystals; later on single-crystals became available. As in all unconventional superconductors the sample quality is crucial. It was shown that the quality of the samples can be increased from a residual resistance ratio (RRR) of $\sim$ 5 to $\sim$ 30 by annealing which leads to a sharp ferromagnetic transition [124].

By doping UCoGe with Si [125], germanium sites are occupied by silicon and a negative chemical pressure is applied. FM and SC are suppressed at germanium concentration of 12%. Measurements of the electrical resistivity, magnetization and ac-susceptibility have been performed making it possible to establish a temperature-composition diagram (see figure 5.6). We will interpret the data in section 5.6.4. It should also be noted that by increasing the Si concentration more and more non-magnetic defects are introduced.

For more information on sample preparation refer to [121],[124] or chapter 6.

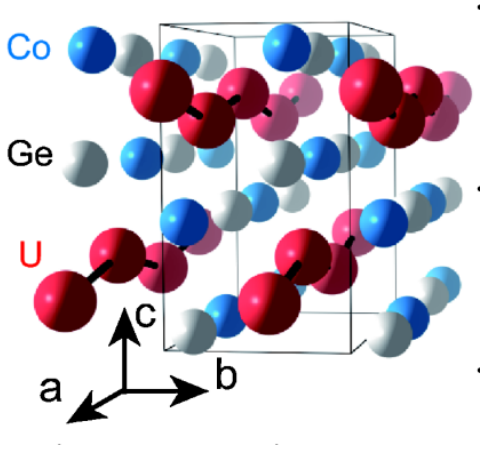

Figure 5.5: Crystal structure of UCoGe (TiNiSi, space group P_{nma}). The uranium atoms along the a axis form a zig-zag chain. The distance between uranium atoms is 3.5 Å (Hill limit), from [123].

5.6.3 Ferromagnetism

In figure 5.8 the first magnetization measurements (in a field of 100 G) of a poly-crystalline UCoGe sample are shown: The magnetic moment is only $0.03\mu_B$ for $T \to 0$. The Curie temperature T_{FM} can be estimated 3K using the Arrott plot (see inset) [121]. The magnetisation for UCoGe is along the c axis (the same as for URhGe).

Several experimental results classify UCoGe as a **weak itinerant ferromagnet** [126]:

1. The Curie-Weiss effective moment is $p_{eff} = 1.7\mu_B$. This can be deduced by the Curie constant C of the Curie-Weiss law ($\chi = \frac{C}{T-\theta_p}$). The magnetic moment of the poly-crystal ($0.03\mu_B$) and of single-crystals ($0.07\mu_B$ [127]) is much smaller than p_{eff} indicating weak itinerant magnetism.
2. The aforementioned magnetization measurements on a single-crystal also show that the magnetisation vs. temperature dependence obeys the equation $M^2(T) = M_0^2(1-(T/T^*)^2)$ (for $T^* \sim T_{FM}$ and $M_0 = 0.07\mu_B$). This dependence was worked out by Lonzarich and Taillefer for weak itinerant ferromagnets [128].
3. The magnetic entropy S_{mag} that can be obtained by specific heat measurements is much smaller than the value expected for a local moment system with spin 1/2 [129].
4. Up to applied fields of 15 T [130], the magnetisation of UCoGe does not saturate. This is a sign that local moments do not dominate the magnetic properties.

Electrical resistivity measurements on the poly-crystalline and mono-crystalline samples (see figure 5.7) showing a broad hump at about 3K (corresponding to the ferromagnetic transition) confirm the Curie temperatures.

The resistivity above T_{FM} is proportional to $T^{5/3}$. This indicates scattering at critical FM spin fluctuations [124], thus UCoGe is close to magnetic long-range order. This is also confirmed by recent NMR measurements (see section 5.6.5). Below T_{FM} the resistivity is $\propto T^2$ because of scattering at magnons.

It should be noted, that V. Sechovsky *et al* ([131], [132]) reported ferromagnetic spin fluctuations at zero field (in contrast to ferromagnetic order) and FM only in magnetic field. It was suggested being due to sample quality issues [129].

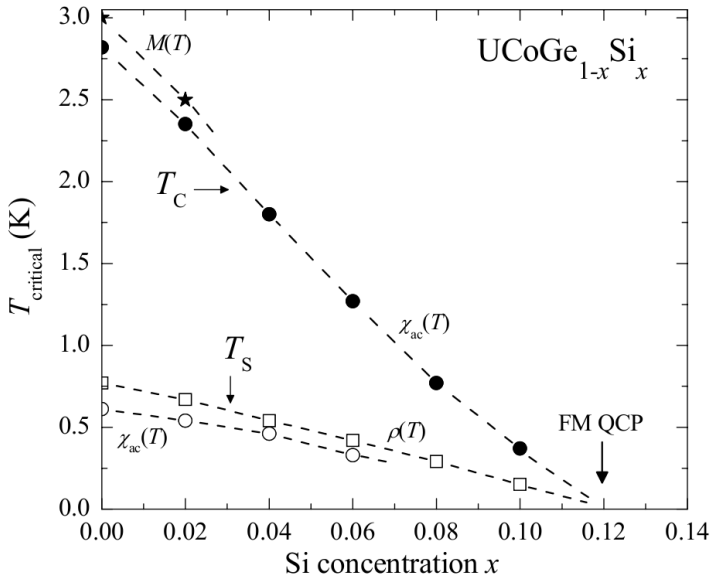

Figure 5.6: Temperature-composition diagram of $UCoGe_{1-x}Si_x$: The ferromagnetic and superconducting transition temperatures were obtained by magnetization, resistivity and ac-susceptibility measurements, from [125].

5.6.4 Superconductivity coexisting with ferromagnetic order

The ferromagnetic and superconducting transitions can also be observed in ac-susceptibility measurements (see figure 5.8(b)). The 60% - 70% of ideal screening is achieved at low temperatures (the ideal screening is $\chi_S = -1/(1-N)$, $N = 0.08$ being the demagnetization factor). The two different curves differ in their SC onset temperature. This means that superconductivity is **sensitive to sample quality**, typical for unconventional superconductivity.

Variations of the linear thermal expansion coefficient α close to T_{SC} and T_{FM} prove that SC and FM are **bulk properties** [133] and do coexist as the variation of α for the FM transition is much larger than for the SC transition (meaning that the magnetic order is not expelled from the sample volume). Furthermore α shows a pronounced anisotropy (largest length change along b axis).

Muon spin relaxation and rotation measurements indicate that ferromagnetism and SC are both bulk properties and **coexist locally** in UCoGe unlike in former ferromagnetic compounds in which the SC and FM were contained in different sub-systems[134].

By doping UCoGe with Si ($UCoGe_{1-x}Si_x$) [135] FM and SC get suppressed at a silicon concentration of $x \sim$12%. From the temperature-composition diagram it can be concluded that SC is confined to the ferromagnetic state. As with increased Si concentration non-magnetic defects are introduced and the fact that the Curie temperature and T_{SC} are correlated can be interpreted as **SC and FM being cooperative** and carried by the same electrons, being scattered by the same defects.

Dc magnetization measurements and ac magnetic susceptibility indicate itinerant ferromagnetism and the absence of the Meissner state, meaning that the internal magnetization - playing the role of an applied field - impede a state in which the magnetic flux is expelled completely from the sample, instead a **spontaneous vortex state** is adopted [136]. This self-induced vortex state is also a possible scenario put forward by Ohta *et al*. Their nuclear quadrupole resonance (NQR) measurements indicate FM to be a bulk property and the SC state to be inhomogenous [123].

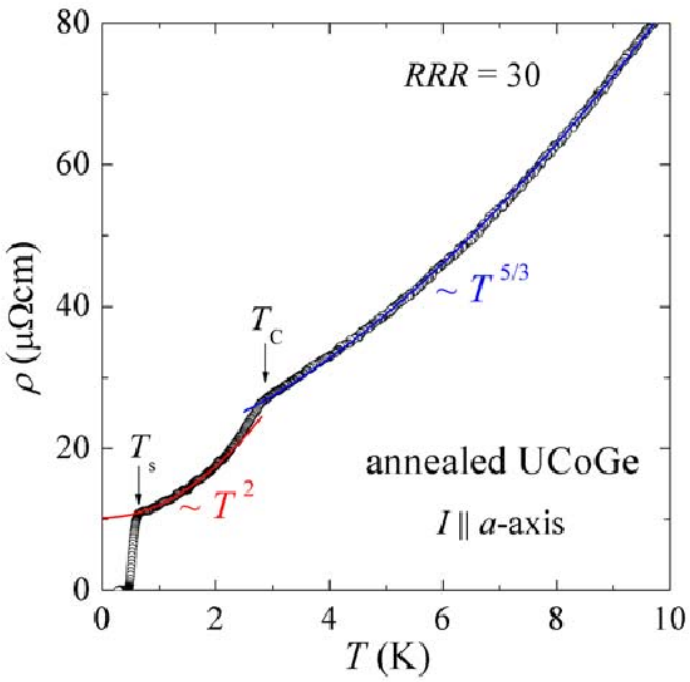

Figure 5.7: Resistivity over temperature of a single-crystal of UCoGe. The current flows along the a axis. The superconducting onset temperature and the Curie temperature are 0.65 K and 2.8 K respectively. Below T_{FM} the resistivity follows a square law, above it is $\propto T^{5/3}$, from [124].

5.6.5 Order Parameter

Upper critical field B_{c2} measurements [127] give a strong indication of triplet superconductivity as the critical field at low temperatures is higher than the Pauli paramagnetic limit (refer to section 1.4.1). The large anisotropy of the critical field, suggests axial symmetry of the order parameter (with point nodes along the c axis) if p-wave superconductivity is realized in the system.

The H_{c2} vs. T measurement has been confirmed by D. Aoki [137]. In the experiment the critical fields are even higher, probably due to better alignment of the applied field. The critical fields for each axis are depicted in figure 5.9. The main points are: a large value of the critical field for $\mathbf{B} \parallel \mathbf{a}, \mathbf{b}$, a large anisotropy of about 10 compared to the other field directions and the upturn with decreasing temperature. Again, this indicates triplet SC. They also find an S-shaped H_{c2}^{b} curve that indicate an enhancement of SC by an increased effective mass close to a field-induced ferromagnetic instability (ferromagnetic quantum criticality) [137].

Recently, direction dependent NMR experiments on a single crystal were performed in the normal state [138]. The authors suggest that FM fluctuations along the c axis - observed by Knight shift and nuclear spin-lattice relaxation rate measurements - are responsible for spin-triplet pairing.

5.6.6 Pressure Phase Diagram

Two **pressure-phase diagrams** have been established [139], [140] using resistivity and ac susceptibility measurements. The phase diagram of [140] is depicted in figure 5.10. Notice, that superconductivity is still existant above the critical pressure p_c of ferromagnetism.

Theoretical considerations in analogy to the superfluid phases of ^{3}He suggest two superconducting phases realized by triplet pairing states [142].

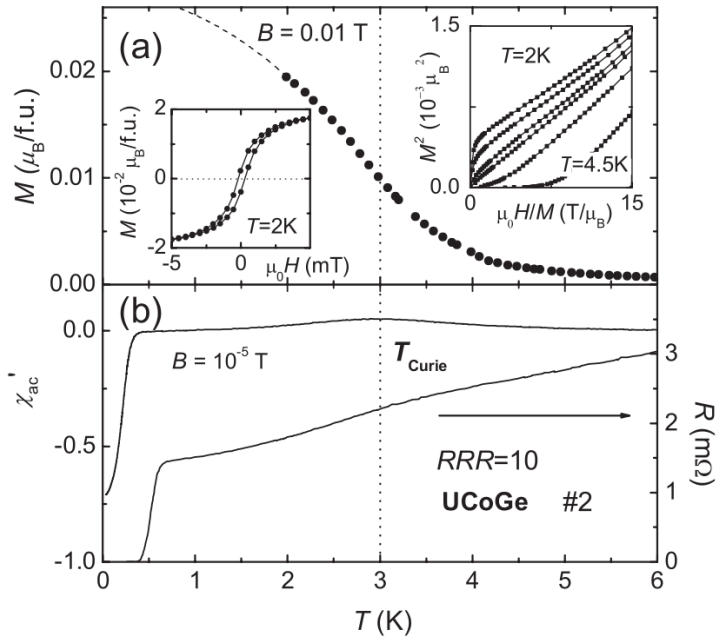

Figure 5.8: Magnetization and ac-susceptibility measurements on polycrystalline UCoGe, from [121].

As we cannot apply pressure on the sample with our experimental setup, only the ambient pressure region can be probed with our scanning SQUID microscope.

5.6.7 Estimates for coherence length and penetration depth

By measuring the **upper critical field** B_{c2} in dependence of temperature the coherence length and the mean free path were estimated to be 12 nm and 90 nm respectively [127]. Furthermore the penetration depth was estimated to be $\sim$ 1 micrometer [125].

5.6.8 Other aspects

The fact that the linear term in the electronic specific heat is 0.057 J/molK^2 (eight times the mass of the free electron) leads to the conclusion that the electrons are correlated. The low specific heat in comparison to other heavy fermion compound is due to a small pocket Fermi surface [143].

Two-band SC was put forward as one possiblity to explain the upward curvature of the critical field measurements [127]. This scenario is in line with calculations made for orthorhombic itinerant ferromagnetic superconductors [144] [145].

Polarized neutron diffraction experiments find that the ordered moments in low magnetic fields are located at the U site (at B=3 T the moment is about 0.1μ_B). At higher field (12 T) this moment goes up (to 0.3μ_B) and even induces a substantial moment at the Co atoms (0.2μ_B at 12 T anti-parallel to U moment) [146].

5.6.9 Conclusion

To summarize the above measurements we can state that UCoGe is a

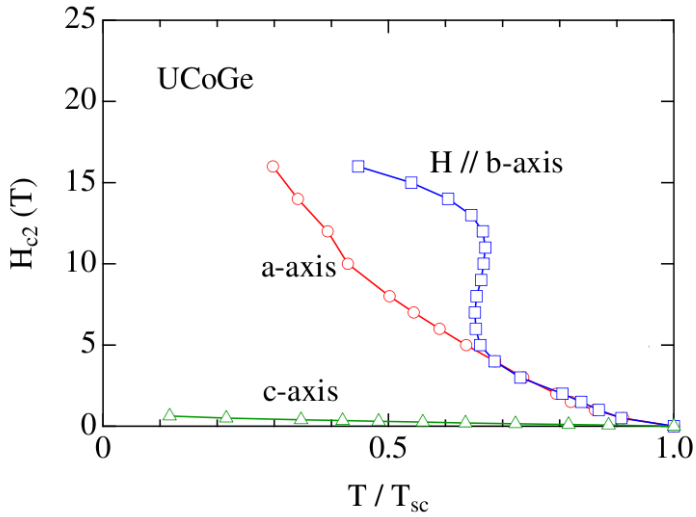

Figure 5.9: Upper critical field vs. temperature for the three different axes. T_{SC} is normalized by the superconducting transition temperature at zero field, from [137].

ferromagnetic superconductor with a ferromagnetic transition at about 2.5 K and a superconducting transition temperature of $\sim$ 0.5 K. Both can vary significantly with sample quality. The ferromagnetic and superconducting states are bulk properties and from Si doping it can be infered that the SC/FM interplay is constructive.

weak itinerant ferromagnet with a small magnetic moment of about $0.07\mu_B$. The itineracy is due to the $5f$-electrons of uranium.

triplet superconductor indicated by the critical magnetic field B_{c2} exceeding the Pauli limit and having an upturn with decreasing temperature. This was also confirmed by NMR measurements.

heavy fermion compound with an electronic specific heat of 0.057 J/molK^2. This means that the effective electron mass corresponds to 8 times the mass of a free electron. This low effective mass is due to a small pocket Fermi surface.

Another important point learned from the above measurements is that the sample quality is of utmost important in order to capture the underlying physics correctly.

5.6.10 Open Questions

The measurements made up to now have been either probing macroscopic properties (thermal expansion, electrical resistivity, ac-susceptibility, etc.) or local properties in reciprocal space (μSR, neutron diffraction). However the magnetic domains in real space and their behaviour as a function of applied magnetic field or temperature, in particular at the transition between superconducting and normal state, are unexplored.

In order to confirm the hypothesis of a spontaneous vortex state it would also be important to visualize vortices and their spatial distribution. It would also respond to the question if the superconducting state nucleates first at domain boundaries or in the center of domains. This would be another independent method to confirm the symmetry of the order parameter, notably if it is a singlet or triplet state. For the moment only crude estimates of the coherence length and the penetration depth were made, direct experimental data via STM measurements or scanning SQUID microscopy could shed light on these points. Even though most groups conjecture spontaneous magnetization in zero field, this question is not yet answered completely.

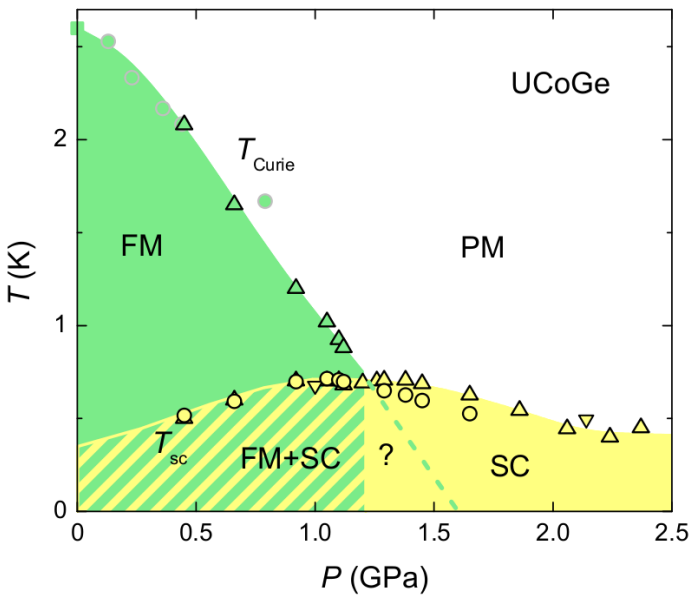

Figure 5.10: Pressure-temperature phase diagram of a polycrystalline UCoGe sample. The upward triangles, downward triangles and circles correspond to the susceptibility in a piston cylinder cell, susceptibility in a diamond anvil cell and resistivity measurements. Grey circles are from reference [141], from [140].

In the next chapter we will present the results on UCoGe obtained by scanning SQUID microscopy and thus image - for the first time - the domain structure in the sample. We will present the behaviour of this domain structure at different applied magnetic fields and temperatures and discuss the result with respect to the theoretical predictions presented in this section.

6 Measurements on UCoGe

6.1 Introduction

In this chapter we discuss measurements done on UCoGe samples grown by Dai Aoki at the CEA Grenoble. These samples have been studied with different techniques. Some results have already been mentioned in the last chapter.

First, we present the sample fabrication and preparation and then move on to the experimental results of heat capacity measurements showing transition characteristics comparable to other samples in literature, magnetization measurements performed by Carley Paulsen (Institut Néel) in combination with our scanning SQUID microscopy measurements. The question of a spontaneous vortex state and finally the response of domain walls to the superconducting transition is addressed as well.

The motivation of this work is to image the field distribution above UCoGe on a local scale. This allows for a better understanding of the compound by linking already obtained measurements in momentum space or on the whole sample volume to local magnetic images. It will thus be possible to see how an applied magnetic field or the temperature (above or below T_{SC}) affect the domain structure.

6.2 Sample fabrication and preparation

The samples used for the measurements presented in this chapter were all fabricated by Dai Aoki at the CEA Grenoble.

The high-quality samples were grown in a tetra-arc furnace using the Czochralski method. Uranium, cobalt and germanium were melted under purified argon atmosphere. By melting the polycrystalline ingot several times a homogeneous phase was obtained. By using a seed crystal single crystals were pulled. The pulling rate used was 15 mm/hour [143].

The single crystals were annealed under ultra high vacuum at a temperature just below the melting point for 12 hours and 20 hours in a horizontal radio frequency and an electrical furnace, respectively. An image of a single crystal is shown in figure 6.1. The single crystals were cut into small samples.

The sample studied in this work is 340 μm high, 290 μm large and in average 1.11 mm long. Its mass

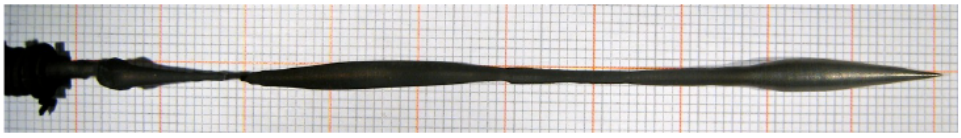

Figure 6.1: Single UCoGe crystal, from [143].

is 1.325 mg (all the lengths have been determined with an optical microscope). This corresponds to a nominal density of 12.1 g/cm^3.

The theoretical value can be obtained as follows: UCoGe has a TiNiSi structure with 4 U, 4 Co and 4 Ge atoms in the elementary cell. This leads to a mass per unit cell of $m_{cell} = 4 \times (238.03\text{u} + 58.933\text{u} + 75.64\text{u})$ with $\text{u} = 1.660538 \times 10^{-27}$ kg. The volume of the unit cell $V_{cell} = abc$ with $a = 0.6845$ nm, $b = 0.4206$ nm and $c = 0.7222$ nm leads to the theoretical density of 11.8 g/cm^3. This corresponds to the experimental value of 12.1 g/cm^3 within the uncertainty of our estimates of the sample dimensions.

The sample was prepared for near field microscopy by polishing with diamond paste.

6.3 Interpretation of the critical current images

6.3.1 Introduction

Images taken by our microscope represent the critical current of the SQUID as a function of the x,y position of the scanner. The critical current is a periodic function of the flux penetrating the SQUID loop. The flux corresponds to a magnetic field and the period of the SQUID characteristics is 16.8 G for a 1.1 µm SQUID (as used for this experiment).

As a consequence of the periodicity we can obtain the same critical current for magnetic field variations larger than 16.8 G. The field variation above the ferromagnetic domains of UCoGe is several times larger than this period leading to a non-univoque representation of the experimental images. Therefore, we use simulations to ease the interpretation of the experimental images.

If we suppose to know the field distribution close to the sample surface, this information can be used to derive the field distribution at the height h of our SQUID and thus ultimately lead to simulated critical current images (using the known I_c vs. Φ_{app} curves), like the ones obtained by our microscope. The numerical calculations have several merits: First, we can foresee if certain features will be observable with our microscope. Second, by comparing experimental data with the results of the calculations it makes quantitative claims for physical quantities like magnetization and the penetration depth feasible. And third, it helps the experimentator to interpret measured images.

We start by deducing solutions the the Laplace equation for boundary conditions representing the geometry of our experimental setup. The solutions are used to numerically calculate the flux at a distance corresponding to the distance between sample and SQUID supposing a known field distribution at the sample surface.

We do not present the inverse case in which we try to calculate the field at the sample surface by propagating the field in the opposite direction, nor do we use techniques like the one proposed by Landweber - to reconstruct the field distribution at the sample surface - as these approaches did not lead to better results in our case and one has to be careful interpreting their results due to semi-convergence [147]. For a good review on different image reconstruction techniques see reference [148].

The measurements on UCoGe with scanning SQUID microscopy have been performed in three con-

figurations depicted in figures 6.3.1 and 6.3. We imaged the **ab**-plane and the **ac**-plane of the sample and in the latter case oriented the applied field along the **b** or **c**-direction.

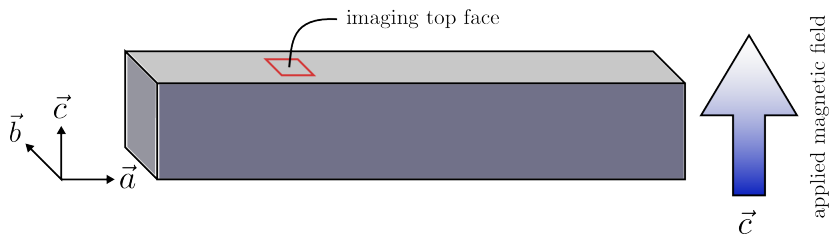

Figure 6.2: A schematic view of the crystallographic axes, the direction of the applied field and the plan that was imaged. It applies to all scanned images of the **ab**-plane.

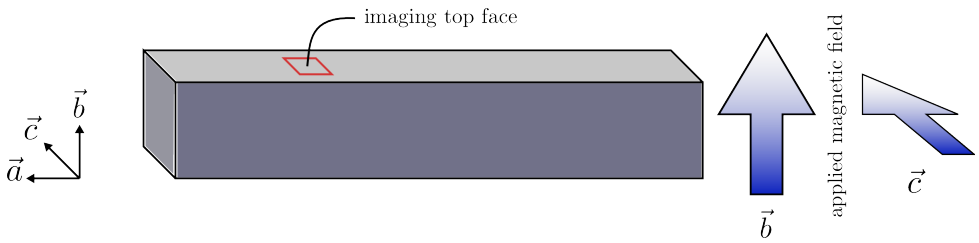

Figure 6.3: The configurations used when the **ac**-plane was scanned: either the field was applied perpendicular to the scanned face or in-plane.

6.3.2 Laplace equation

Now, we deduce the Laplace equation that will be solved analytically and numerically in the next sections.

Magnetostatics is described by the following two laws:

$$\nabla \times \mathbf{B} = \mu_0 \mathbf{j} \qquad \text{(Ampere's law)} \tag{6.1}$$

$$\nabla \cdot \mathbf{B} = 0 \qquad \text{(Absence of magnetic monopoles)} \tag{6.2}$$

In a currentless vacuum ($\nabla \times \mathbf{B} = 0$) the magnetic field can be written as the gradient of a magnetic scalar potential:

$$\mathbf{B} = -\nabla \Phi \tag{6.3}$$

and in combination with equation 6.2 this becomes the famous **Laplace equation**:

$$\nabla^2 \Phi = 0 \tag{6.4}$$

To solve the Laplace equation (6.4) we use a separation *ansatz*:

$$\Phi(x,y,z) = X(x) \cdot Y(y) \cdot Z(z) \tag{6.5}$$

plugging it in leads to (not considering the trivial solution $\Phi = 0$ everywhere):

$$\underbrace{\frac{1}{X}\partial_x^2 X}_{-k_x^2} + \underbrace{\frac{1}{Y}\partial_y^2 Y}_{-k_y^2} + \underbrace{\frac{1}{Z}\partial_z^2 Z}_{k^2} = 0 \tag{6.6}$$

As each of these terms is independent of the others, each one has to be constant. So we can transform the partial differential equation to three ordinary ones:

$$\frac{1}{X}\partial_x^2 X = -k_x^2 \qquad \frac{1}{Y}\partial_y^2 Y = -k_y^2 \qquad \frac{1}{Z}\partial_z^2 Z = k^2 \tag{6.7}$$

with $k_x^2 + k_y^2 = k^2$. The solutions of these three equations are:

$$\begin{aligned} X &= \exp(\pm i k_x x) \\ Y &= \exp(\pm i k_y y) \\ Z &= \exp(\pm k z) = \exp(\pm\sqrt{k_x^2 + k_y^2} z) \end{aligned} \tag{6.8}$$

All the linear combinations of $\Phi = X \cdot Y \cdot Z$ are solutions of equation 6.4.

To solve a concrete problem, one first needs to define **boundary conditions**. With our SQUID scanning microscope we are scanning a flat surface with magnetic features and we measure the field distribution at a certain height h from the surface. In order to interpret and validate our images, our goal is to define reasonable boundary conditions at the sample surface and compare them with the measured images. The other boundary condition is that at infinite distances the field falls off to zero:

$$B_z(x, y, z = 0) = \left(-\nabla\Phi(x, y, z = 0)\right)_z \tag{6.9}$$

$$\lim_{\|\mathbf{r}\|\to\infty} B_z(\mathbf{r}) = 0 \tag{6.10}$$

with $\mathbf{r} = (x, y, z)$. In the first equation we constrain ourselves to the z-component, because we are using a squid parallel aligned to the surface. Because of the second boundary condition we only have to consider the decaying exponential of the Z solution.

Remark: The exponential terms in equations 6.8 fall off more quickly, the higher the corresponding k-value is. As a consequence high frequency boundary conditions will be smoothed out more quickly with increasing distance than big features as low k values correspond to large features in real space. This is schematically illustrated in figure 6.4.

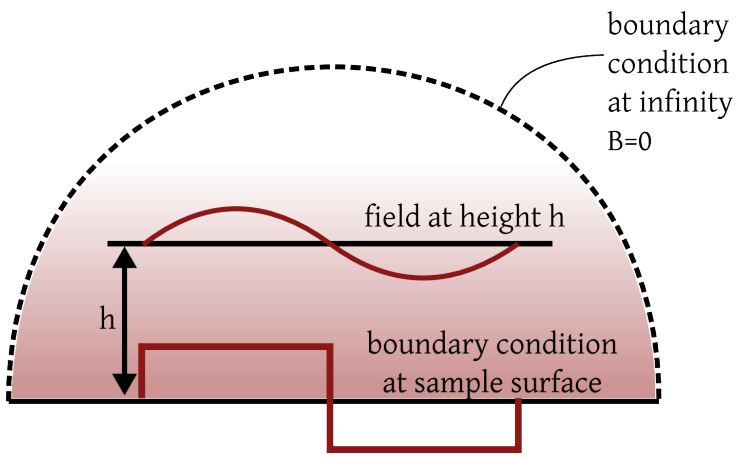

Figure 6.4: Solving the Laplace equation for a step like field at the sample surface. Notice how the high frequency contributions are lost at a height h.

6.3.3 Numerical calculations

By looking at equations 6.8, it becomes clear that the boundary condition at the sample surface can be expressed by the two wave vectors k_x and k_y. The wave vectors can be obtained by using a 2D **Fourier transform** of the boundary conditions. For discrete images ($N \times M$ pixels) we need the discrete 2d Fourier transform, defined as:

$$\tilde{f}(u,v) = \frac{1}{NM} \sum_{x=0}^{N-1} \sum_{y=0}^{M-1} f(x,y) \exp(-2\pi i(xk_x/N + yk_y/M)) \tag{6.11}$$

We then obtain the z-component of the field by simply multiplying the Fourier transformed boundary condition with the propagation term in z-direction of equation 6.8:

$$\tilde{B_z}(k_x,k_y,z) = \underbrace{\tilde{B_z}(k_x,k_y,0)}_{\substack{\text{Fourier transform} \\ \text{of "surface image"}}} \cdot \underbrace{\exp(-\sqrt{k_x^2+k_y^2} \cdot z)}_{\text{propagation term}} \tag{6.12}$$

In order to get $B_z(x,y,z)$ (direct space) we retransform $\tilde{B_z}(k_x,k_y,z)$ using the inverse Fourier transform, defined as:

$$f(x,y) = \sum_{k_x=0}^{N-1} \sum_{k_y=0}^{M-1} \tilde{f}(k_x,k_y) \exp(2\pi i(xk_x/N + yk_y/M)) \tag{6.13}$$

6.3.4 Magnetic domains

In this section we will apply simulations to discuss imaging of magnetic domains. These simulations will help us to interpret and quantitatively analyse the images made above a sample surface with magnetic field variations exceeding the period of critical current of the used SQUID (16.8 G) with a 1.2 μm^2 area.

In the following the simulations are discussed step-by-step:

1. **Defining boundary conditions at sample surface:** We start by defining the magnetic field close to the sample surface like the one expected at the surface of an Ising-like ferromagnet. The black and white spots in figure 6.5(a) correspond to a magnetic field of ± 22.5 G. The image was created by putting circles of different size, position and magnetization randomly on the sample surface.
2. **Calculating the field distribution at a height h from the surface:** Once the domains are generated, we Fourier transform the image and multiply it with the term describing the evolution of the z-component of the magnetic field in z-direction (equation 6.8). This is depicted in figure 6.5(b): as can be noticed the domain boundaries become smoother.
3. **Convolve with the SQUID shape:** The next step is to convolute the image at a height h with the shape of our SQUID loop. This corresponds physically to the fact that we have to integrate the field over the SQUID area to get the flux penetrating the SQUID loop. The image again becomes smoother than the previous one (figure 6.5(c)).
4. **Calculating the resulting critical current:** The last step consists in relating the flux penetrating the SQUID to the corresponding critical current (figure 6.5(d)). The effect of the periodicity of the I_c over B curve can be seen: when the boundary between two neighboring domains is crossed, the critical current goes up and down several times.

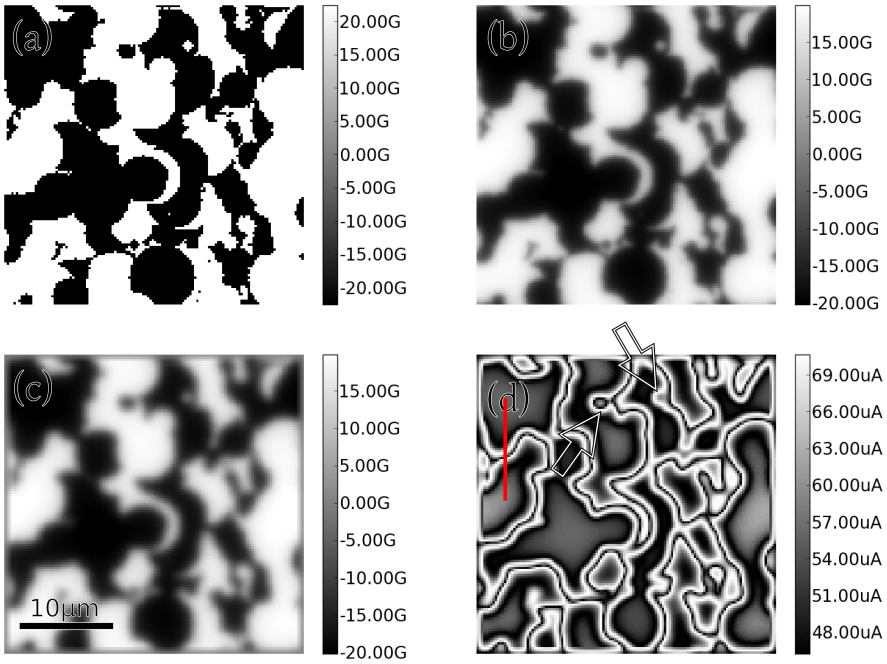

Figure 6.5: Simulation of magnetic domains: (a) the field close to the surface is generated by distributing randomly circles with opposite fields. (b) we calculate the resulting field at a height h corresponding to the height of the SQUID above the surface. (c) the image from (b) is convoluted to account for the shape of the SQUID loop. (d) the critical current at each pixel is calculated by using a typical SQUID characteristic. The two arrows indicate originally separate domains that have merged due to the spatial resolution of the SQUID.

The magnetic field at the sample surface of a given material can be estimated by comparing the simulated images to the measured ones. By counting the number of ups and downs n from the center of one domain to another (see figure 6.6 for the profile of the red line shown in figure 6.5(d)). One period corresponds to 16.8 G, thus it is possible to determine the magnetic field difference of two opposite domains at the sample surface. This method is be used to compare our images to the magnetization measurements of C. Paulsen.

In the following we give several arguments for UCoGe having a small domain wall width (∼Å). We also argue that the domains do not reconstruct extensively close to the sample surface. Consequently, our measurements of the surface give information about the domain structure behaviour in the sample.

The numerical calculations are in good agreement with the actual measured images. This means that the ferromagnetic state can be considered uniaxial (**Ising ferromagnetism**) with sharp domain boundaries $w \ll 1$ μm as we would else see large differences in the images: In figure 6.7(bottom) we show the critical current profile when crossing domain boundaries of different width. Comparing the simulations with the experimental data is in line with a domain wall size of less than 1 μm. In the top panel the distance of the two peaks of the critical current for each simulated domain wall size is depicted. The finite size of the SQUID is responsible for the saturation for small domain wall widths.

The width of a domain wall is the result of a competition between the exchange energy and the anisotropy energy [149]. The exchange energy between two neighboring spins can be written as

$$w_{ij} = -2JS^2 \cos\phi_{ij} \tag{6.14}$$

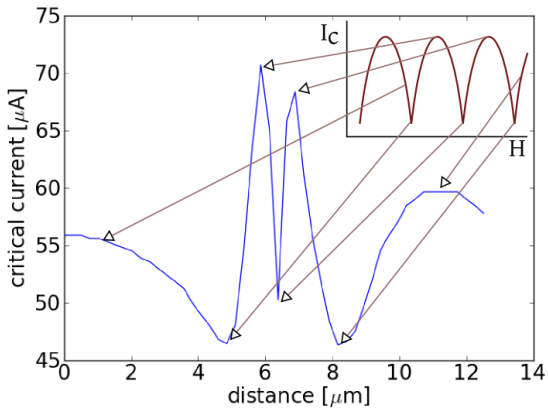

Figure 6.6: Critical current evolution along the red line (d) in figure 6.5. Several arches of the SQUID characteristics are crossed, leading to the non-linear behaviour. The reason for the two minima (and two maxima) are not being equal stems from the insufficient spatial sampling. The inset is an illustration of the SQUID characteristic.

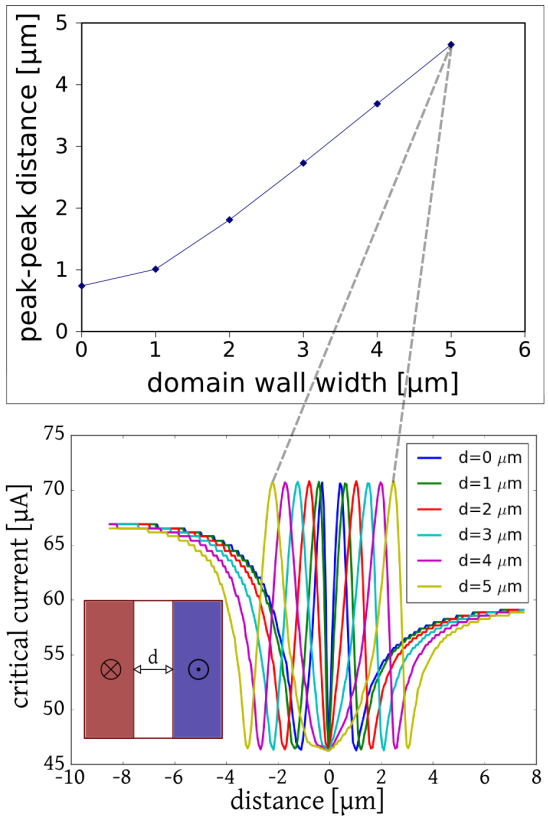

Figure 6.7: Bottom: Simulation of the critical current profile when crossing domain walls of different width. Top: The peak-peak distance of the critical current over the domain wall width. The limited spatial resolution of the SQUID is responsible for the saturation for small domain wall widths. The scanning height was taken to be 400 nm.

with the exchange integral J, the total spin quantum number S of the involved atoms and the angle of the spin magnetic moments between the two atoms ϕ_{ij}. J is related to the Curie temperature by $J = nkT_{FM}$ and n is a numerical factor depending on the lattice structure and S. It is 0.15 for $S = 1$

and a b.c.c. lattice. By expanding the exchange energy for small angles we obtain $w_{ij} = JS^2\phi_{ij}$ making it clear that small rotations of the magnetic moments, and thus large domain walls, are energetically favourable.

However, when the spins are not aligned along the easy axis this will cost anisotropy energy. Thus the system will try to turn the magnetization in as few atomic layers N as possible. The anisotropy energy can be written as:

$$\gamma_a = K/Na \tag{6.15}$$

a being the lattice parameter, K the anisotropy constant.

Minimizing the sum of these two energies with respect to N yields:

$$N = \sqrt{\frac{JS^2\pi^2}{Ka^3}} \tag{6.16}$$

Using the $a = 3.5$, $J = 0.15 \cdot 2.5 \cdot 1.38 \cdot 10^{-23}$, $S = 1$ and the anisotropy constant of iron $K = 4.2 \cdot 10^4$ yields a domain wall thickness $\delta = Na$ of ~ 5.3 Å. Because of the f-electrons in Uranium K should be even higher in UCoGe. Uranium compounds with K as high as 10^{10} are known [150]. It is commonly believed that $N = 1$ [151] in UCoGe.

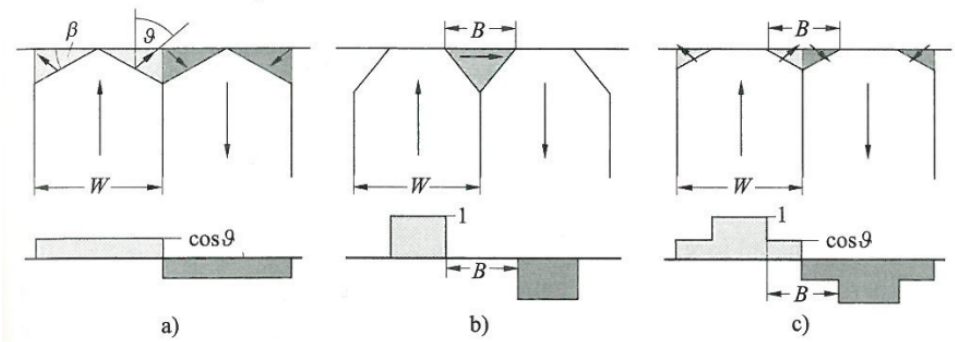

Figure 6.8: Different kinds of closure domains applicable to plates with uniaxial anisotropy. Below each model the surface charge profile is indicated, from [152].

Now that we established that the domain wall width is small and thus the Ising model is realized by UCoGe, we also want to show that the reconstruction in the form of closure domains (see figure 6.8) or domain branching (see figure 6.9) does not take place or at least does not perturb our measurements.

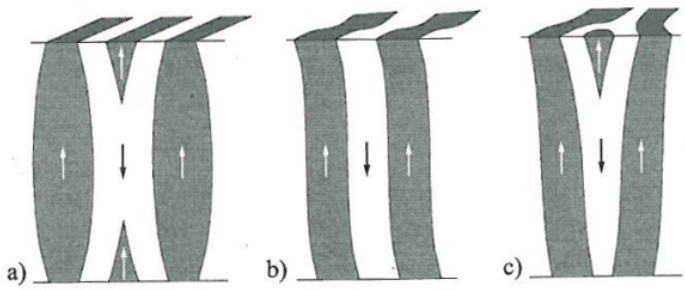

Figure 6.9: Planar two-dimensional (a) and three-dimensional (b) domain branching and refinement in two-phase systems, from [152].

The field distribution due to a superconducting vortex can be approximated by a magnetic monopole buried 1 µm beneath the surface. The deeper the monopole is buried, the lower the spatial resolution $\propto h + d$ of our SQUID microscopy will be (d being the depth of the monopole and h the height

of the SQUID). Thus closure domains of several μm would make it impossible for us to obtain sharp domain structure images, even more so as the stray field would not be perpendicular to the SQUID.

The smaller domain structure due to branching would lead to a cancelling out of the magnetic field contributions at a height of our SQUID (several hundred nanometers). This scenario could be simulated by a domain wall without magnetization. In figure 6.7 the results for different domain wall widths are shown. Within our spatial resolution no domain wall broadening becomes apparent. The magnetic field close to the sample surface of the domains is consistent with bulk measurements performed by C. Paulsen yielding a magnetic field associated with the spontaneous magnetization of $B = 4\pi M_s = 52$ G inside the sample, further corrobating the fact that the domain reconstruction at the surface is rather weak. Our estimate is that the domain reconstruction happens at a depth of about 100 nm or less.

Note, that the magnetic sensitivity of the SQUID depends on the slope of the I_c vs. Φ_{app} curve. Close to the maximum critical current the sensitivity is reduced due to the flat slope in comparison to the minimal critical current region. As a consequence, the sensitivity is not constant throughout an image, making it more difficult to detect domain size changes. We estimate the spatial resolution to be about 2 μm in this case.

As a consequence of the non-monotonic behaviour of the critical current as a function of flux penetrating the SQUID and the background in form of magnetic domains, we cannot compare images by simply subtracting the values of corresponding pixels. Therefore we cannot take advantage of the high magnetic resolution per pixel of around $5.4 \cdot 10^{-3} \Phi_0$/pixel. We estimate the magnetic resolution in this case to be around 1 G/pixel.

6.3.5 Images at different heights

In figure 6.10 images of the **ab**-plane are shown (T=250 mK). These images have been taken in parallel planes above the sample at different heights: 400 nm, 1.4 μm, 2.4 μm and 4.4 μm. In the first image one crosses several critical current minima and maxima when going from the center of one domain to the next, whereas in the last image (d) this is not the case. This clearly corrobates our interpretation of observing domains in UCoGe, as no gradient or other effects can be seen. Furthermore, we see that the regions of fast critical current variations in image (a) correspond to the domain boundaries.

6.4 Specific heat

Specific heat measurements by Dai Aoki and Klaus Hasselbach (see figure 6.11) clearly show that our sample is comparable to samples considered to be of good quality with a RRR of 19. This means that the whole sample becomes ferromagnetic. Other samples in literature with less pronounced peaks are either polycrystals or do not attain high RRR values as these were the first UCoGe samples, since the discovery the annealing procedures were steadily improved.

6.5 Susceptibility

Ac-Susceptibility measurements on the studied UCoGe compound clearly detect the superconducting transition. The onset of the SC transition is at about 450 mK and the screening at low temperatures reaches more than 80%. The fact that the long tail of χ' at low temperatures is not seen in other superconducting samples indicates that the ferromagnetic domain structure plays an important role in the measurement. It is possible that domains of different sizes start to screen the field at different

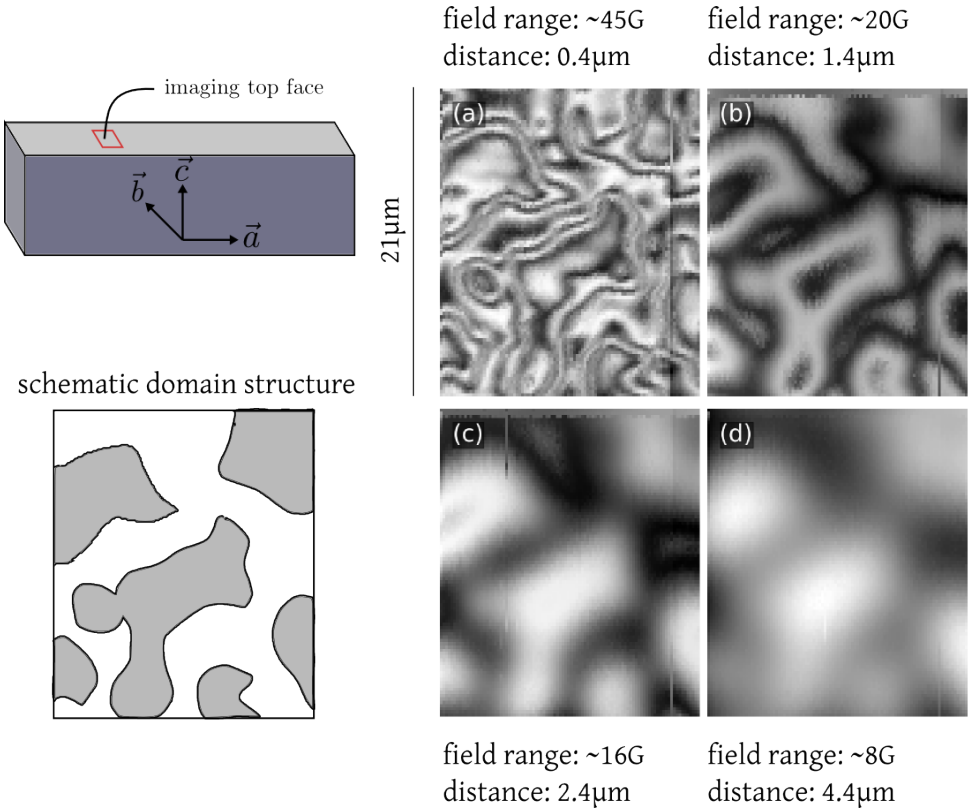

Figure 6.10: Imaging **ab**-plane at different heights (T=250 mK, zero field cooled, no applied field): (a) AFM mode (SQUID/sample distance 400 nm), (b) distance increased by 1 µm, (c) by 2 µm, (d) by 4 µm. These images were taken 40 µm from the border. As the critical current modulation in images (c) and (d) is small enough to stay on one branch of the SQUID characteristic. Therefore, it can be concluded that no background field gradient is present.

temperatures. In other words, the domain size distribution is responsible for the long tail of the susceptibility measurements.

6.6 Magnetic field measurements

6.6.1 Ferromagnetic transition

When scanning the surface of the UCoGe sample with our scanning SQUID microscope we observe a *spontaneous* ferromagnetic transition (in earth magnetic field). This transition occurs when imaging the **ab** as well as when scanning the **ac**-plane (see figures 6.13, 6.14 and 6.15, 6.16).

In both cases we see already a precursor of magnetic ordering at temperatures above the ferromagnetic transition temperature (Curie temperature) of ~ 2.5 K. We do not observe any qualitative or quantitative difference when measuring the magnetic transition at the sample border and the sample center, as can be seen by the measurements done on the **ac**-plane (see figures 6.15, 6.16).

By counting the minima and maxima of the critical current when passing from one domain center to the center of an adjacent domain, it is possible to estimate the magnetic field difference at the sample surface $2B_s$. We estimate $2B_s$ above the domains to be 45 G $\pm$ 5 G in **c**-direction (for the scans imaging the **ab**-plane) and 16 G $\pm$ 3 G for the magnetization in **b** direction. As an example let us take a closer look at the red line of figure 6.13(h): Between the two ends of this line we cross

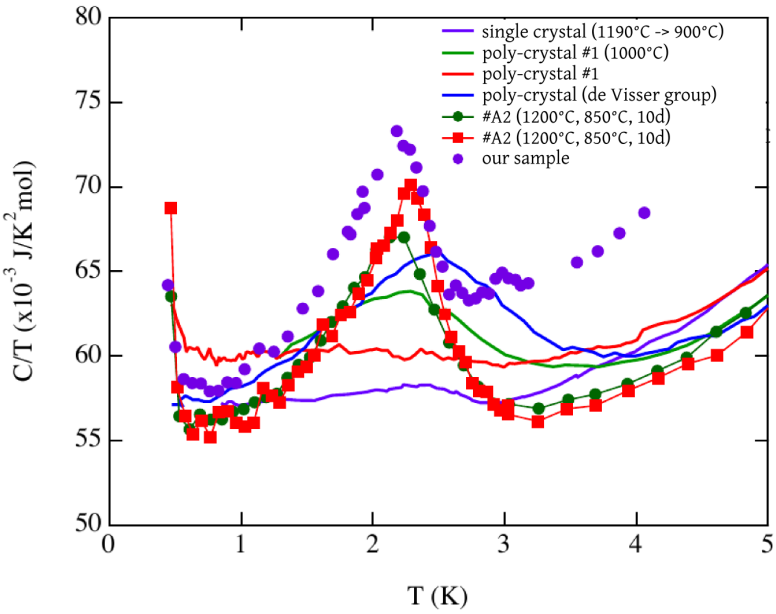

Figure 6.11: Comparison of the specific heat measurements on our sample and samples from literature. Adapted from an figure from D. Aoki.

3 maxima and 3 minima yielding a magnetic field difference B_s of $2.5 \cdot 16.8$ G= 42 G. By analyzing the profile more closely we find the 45 G mentioned above.

These images were taken after a simple cooling down, without field shaking or other techniques that would help to push the system into its equilibrium state. Thus the domains tend to look complicated and they do not minimize their interfaces. As a consequence, we do have a wide domain size distribution: The smallest resolvable domains have a size of about 2 µm and their sizes go up to 20 µm for the largest domains.

By measuring the evolution of the magnetic field difference B_s between two adjacent domains we can plot B_s over temperature (see figure 6.17).

Our local measurements can be compared to bulk magnetization measurements performed by C. Paulsen (see figure 6.18) who finds an internal field of $B = 4\pi M = 52$G.

The magnetization measurements under field, clearly show the ferromagnetic transition. When decreasing the sample temperature the magnetization increases, until the superconducting transition temperature is reached, where the setting in of screening currents reduce the magnetization by their diamagnetic contribution.

In order to compare the field above a domain (SQUID microscopy) with the field inside a mono-domain (bulk measurements) we have to take into account the demagnetization field. C. Paulsen obtained a demagnetization factor of $N \sim 4$ by susceptibility measurements leading to a field above the mono-domain of $B = (4\pi - N)M = 35$ G. For this deduction we supposed an ellipsoid geometry of the sample (demagnetization factor) and a homogeneous magnetization which can account for the difference between the two different measurements.

Another way to compare the two measurements is to calculate the internal field corresponding to the field $B_{ext} = 22.5$ G above a domain of our SQUID measurements. The local measurements show a domain size of about ~10 µm, whereas the sample thickness is ~ 340 µm. In the case of an ideal Ising magnet the domain traverses the whole sample. We can thus suppose the domain to be a long rod with a radius $r = 5$ µm and a length $l = 340$ µm. In this case ($r \ll l$) the internal field $B_i = B_{ext} \cdot 2 = 45$ G leading to a good agreement with C. Paulsen's measurements.

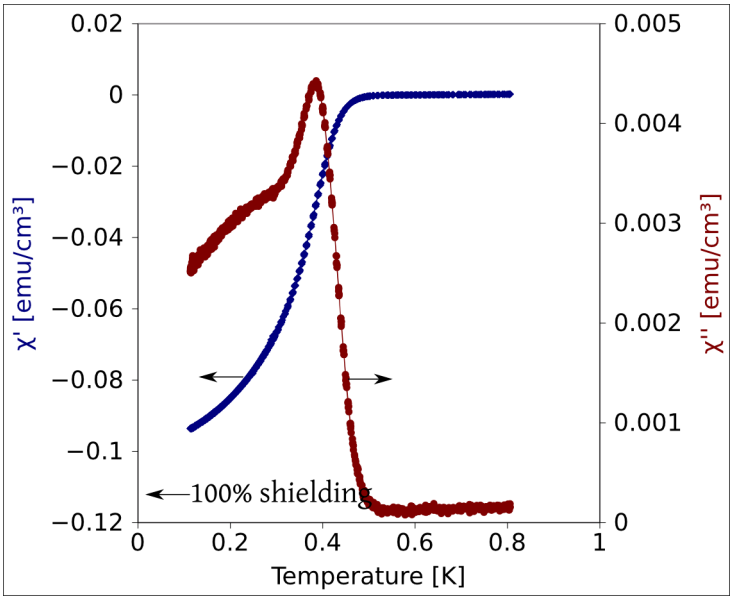

Figure 6.12: ac-susceptibility measurements show that the diamagnetic screening reaches about 85% of a perfect diamagnet. Data from C. Paulsen.

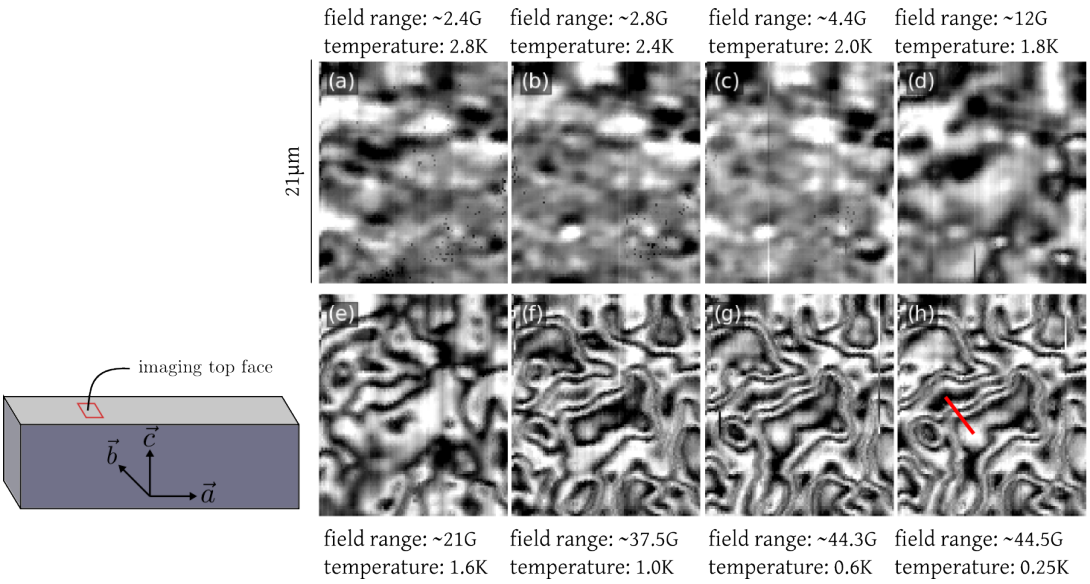

Figure 6.13: Ferromagnetic transition (ZFC, imaging **ab**-plane): These images were taken close to the sample border situated 20 µm from the top of the image. (a) already at 2.8 K a precursor of magnetic ordering can be observed, (b) 2.4 K, (c) 2.0 K, (d) at 1.8 K bigger magnetic structures become visible, (e) we clearly see domains at 1.6 K, (f) 1.0 K, (g) 0.6 K (above the superconducting transition) the biggest domain in the center images has a maximal length of about 20 µm. (h) we do not observe any movement of the domain boundaries beneath the superconducting transition (0.25 K) with our spatial resolution being about 2 µm.

6.6.2 Diamagnetic screening

When cooling the sample below T_{SC} in zero field and applying a field subsequently a superconductor will screen the field, at least partially. By warming it up above the superconducting transition temperature the field can penetrate the sample completely. An observable difference between images

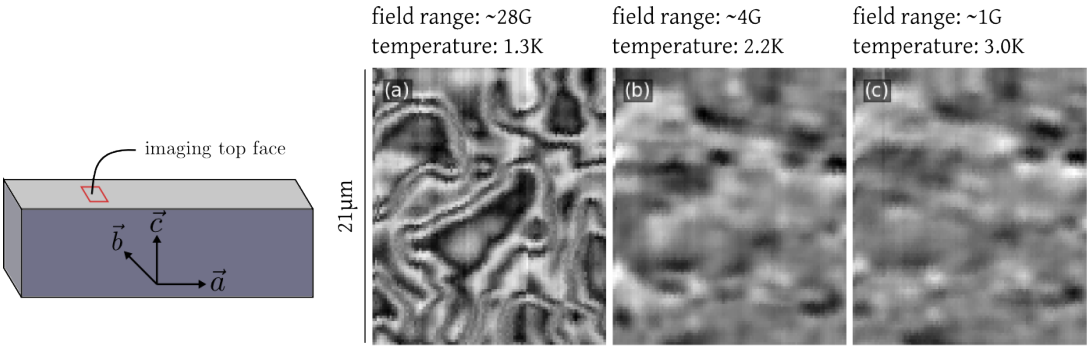

Figure 6.14: Ferromagnetic transition (ZFC and warming up, imaging **ab**-plane): The sample border is situated 20 µm above the images. (a) at 1.3 K we clearly see domains, (b) 2.2 K, (c) 3.0 K. In the last two images only magnetic fluctuations similar to the ones seen when cooling down in figure 6.13 are seen.

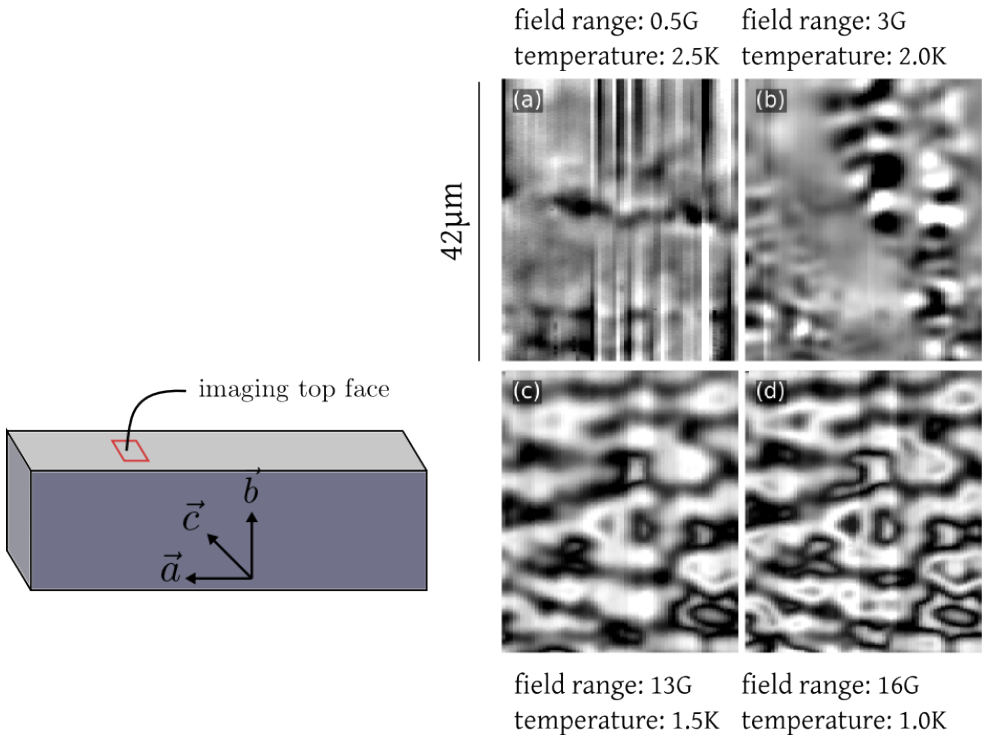

Figure 6.15: Temperature dependence of the forming FM state (ZFC, imaging **ac**-plane): These data were obtained 40 µm from the **sample border**. (a) in the center of the image there is a magnetic signal (2.5 K), (b) this magnetic signal disappears at 2.0 K, (c) 1.5 K: domains appear everywhere in the sample, (d) at 1.0 K (and below): the domain structure does not change further as temperature is lowered.

made in the two different states would confirm screening. The difference could appear as a change in the shape of the domains or by an homogeneous shift throughout the domains.

We have done this kind of measurement for both experimental configurations (scanning **ab** and **ac** plane):

When scanning the **ab** face (see figure 6.19) the sample is cooled in the earth magnetic field down to 220 mK and afterwards 20 G are applied. When warming up to 500 mK a shift of flux throughout the image (change of color) can be seen. This means that at 220 mK the applied field has been -at least partially- screened and when the sample becomes normal conducting the screened field can

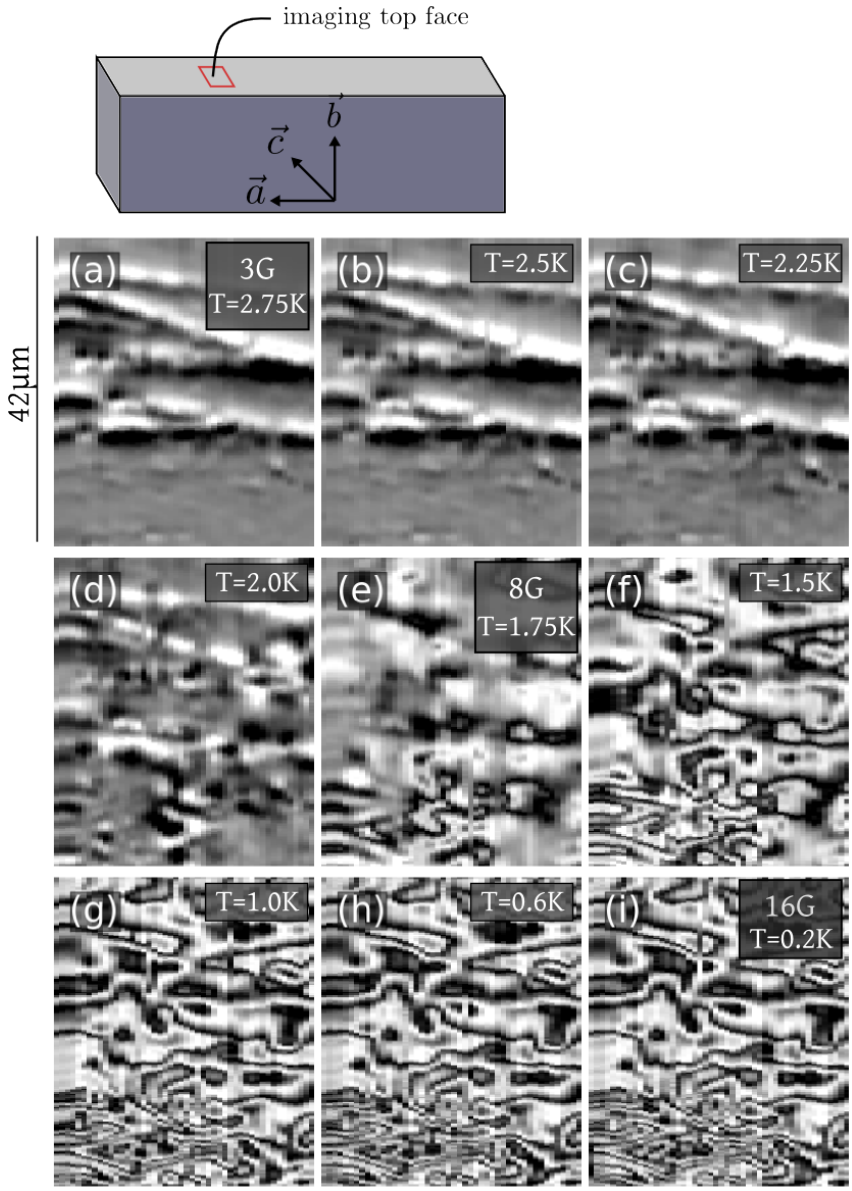

Figure 6.16: Temperature dependence of the forming FM state (ZFC, imaging **ac**-plane): This image series was taken in the sample **center**. In the first three images (a) at 2.75 K the field range is about 3 G, (b) 2.5 K, (c) 2.25 K scratches (horizontal lines) dominate at this scanning site. The defects are reproducible and move less than our spatial resolution of about 2 µm. (d) at 2.0 K the magnetic signal due to domain creation becomes of the same order as the defect signal, (e) at 1.75 K the field range is about 8 G, (f) 1.5 K, (g) at 1.0 K we see that the domains in the region of the defects are bigger than at the bottom (h) 0.6 K (above the superconducting transition) (i) no change in domain size observable at 0.2 K (below T_{SC}). The estimated field difference above two neighbouring domains is $\sim$ 16 G.

enter into the sample and thus changes the flux measured by the SQUID.

In the second case (see figure 6.20) we cool down to 200 mK and apply a field of 50 G in **b**-direction. When we warm up and the sample goes to the normal state, the field penetrates into the sample, so we see a color change in the image. The penetrating field has also an effect on the domain structure, as the average domain size becomes bigger. The effect has not been observed in the first case, which could be due to the higher applied field of 50 G in the latter case.

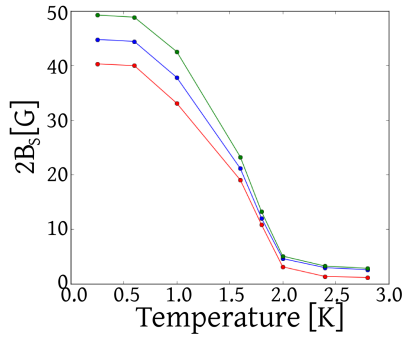

Figure 6.17: Magnetic field difference $2B_s$ associated with the spontaneous magnetization $B_s = 4\pi M_s$ above two neighboring domains in the **c**-direction as determined by images at different temperatures (see figure 6.13). The green curve corresponds to the upper, red to the lower and blue to the best estimate.

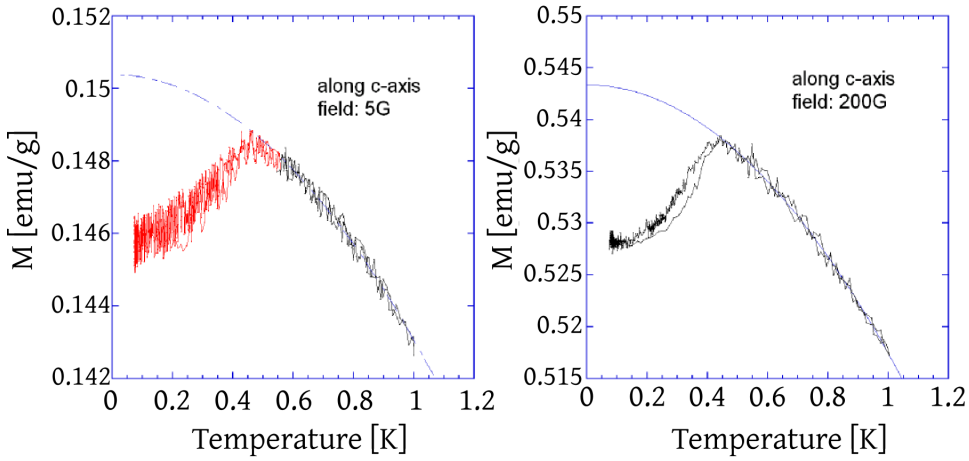

Figure 6.18: Bulk magnetization measurements clearly show a rising magnetization with decreasing temperature until the superconducting transition where diamagnetic screening reduces the magnetization by 3%.

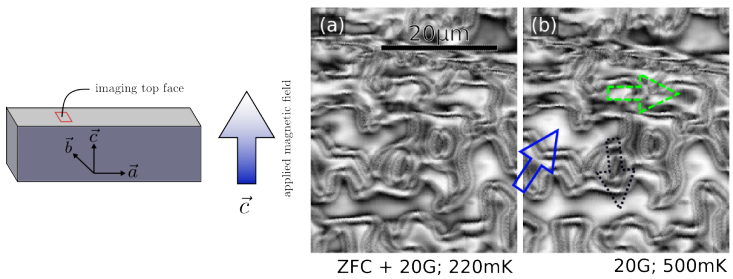

Figure 6.19: Imaging **ab**-plane: (a) ZFC and applied 20 G (in **c**-direction) at 220 mK, (b) T = 500 mK. A field shift can be seen throughout the sample when warming up, thus diamagnetic screening has taken place.

6.6.3 Meissner effect

The magnetization measurements performed by C. Paulsen clearly show a rising magnetization with decreasing temperature below T_{FM} and a dip below T_{SC} due to the field expulsion (Meissner effect). As can be observed from the data this effect is very small (only 3% of the magnetization).

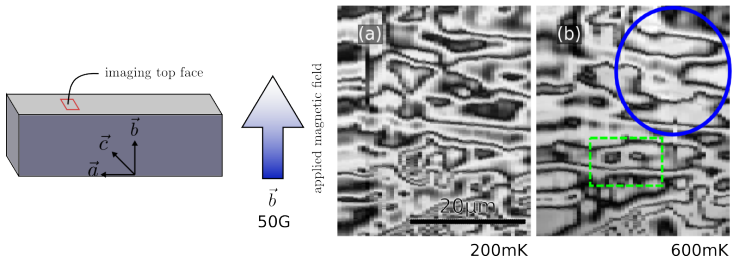

Figure 6.20: Imaging **ac**-direction: (a) ZFC and applied 50 G in **b**-direction at 200 mK (below T_{SC}), (b) after warming up to 600 mK (above T_{SC}) field penetrates into the sample leading to a modification of the domain structure clearly showing diamagnetic screening.

To observe the Meissner effect on the local scale we performed scanning SQUID imaging above and below T_{SC}. As in the last section we have been trying on both sides (**ab** and **ac** plane) to visualize the Meissner effect:

In the **ab**-plane (see figure 6.21) we apply 5 G above the superconducting transition temperature and field cool to 200 mK. We do not see any difference between these images (images are taken in the sample center). If the Meissner expulsion is only partial and not complete, the fact that no significant difference between the two images is detected, can be explained by a lack of magnetic resolution in presence of a strong magnetic background of the ferromagnetic domains.

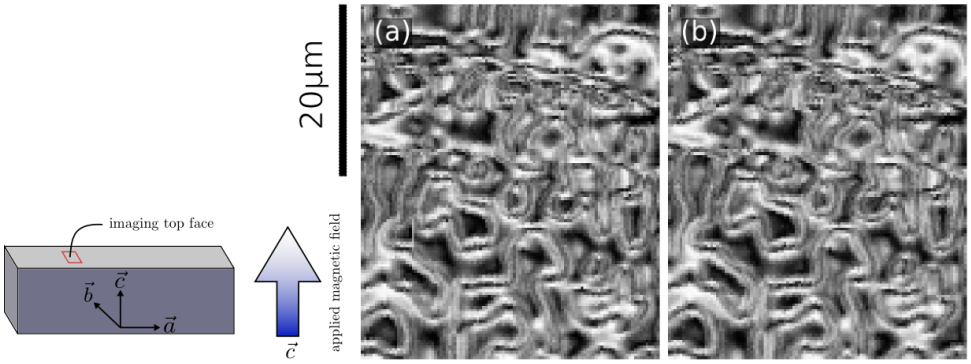

Figure 6.21: Search for Meissner expulsion: (a) at 550 mK we apply 5 G, (b) we cooled down to 200 mK in field. Both images were taken in the **ab**-plane at the center of the sample. There is no significant difference between both images. A difference needed to change from the highest to the lowest critical current would be 8 G. The magnetic resolution of the SQUID is about 0.05 G compared to a signal due to the domain structure of ± 22.5 G. We estimate that a change of about 1G is detectable, meaning that the field expulsion is weaker.

The same procedure is followed for the **ac**-plane. The sample is field cooled in 10 G, but now we do two different experiments: once the field is applied along the crystallographic **b**-direction and once in the **c**-direction (see figures 6.22, 6.23.

In both cases no significant difference is observed in the limits of our spatial and magnetic resolution of about 2 µm and 1 G: Neither the domain walls, nor the field inside the sample have changed. When field is applied along the **c**-axis this is easily understood: The field component that will be measured by our SQUID is perpendicular to the applied field, so one should only see a difference due to non-superconducting regions. The apparent absence of normal state regions indicates the good homogeneity of the sample on the local level. In the case where the field was applied perpendicular to the SQUID we assume that the partial Meissner effect is too weak to be visible, hidden by the complicated background in the form of domains.

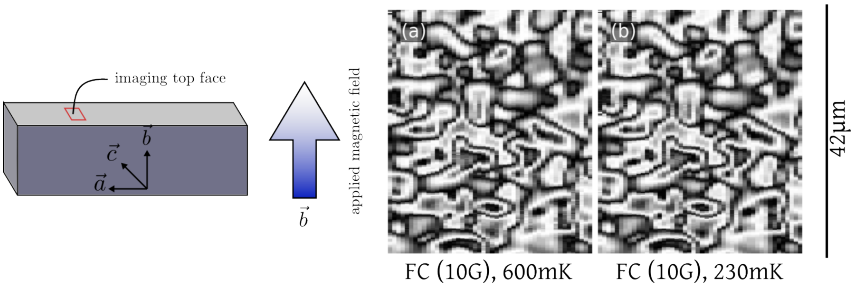

Figure 6.22: Search for Meissner effect on the **ac**-plane at the same position as figure 6.23. Images have a size of 30 µm × 42 µm and were taken at the sample center. Field cooled: (a) 600 mK and 10 G in **b**-direction, (b) after cooling below T_{SC} no difference is visible: Neither the domain walls have moved, nor has the internal field been expelled by Meissner screening.

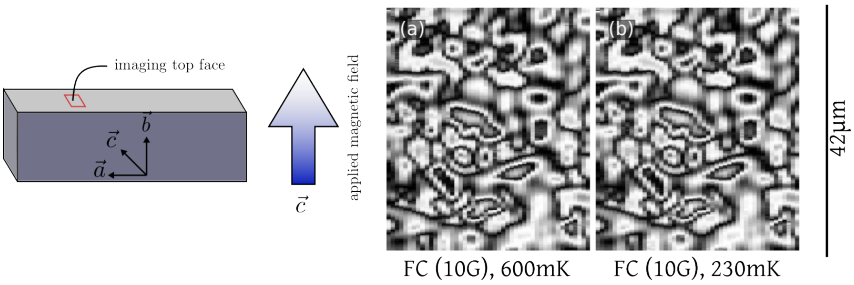

Figure 6.23: Search for Meissner effect on the **ac**-plane at the same position as figure 6.22. Images have a size of 30 µm × 42 µm and were taken at the sample center. Field cooled: (a) 10 G in **c**-direction are applied at a temperature of 600 mK, (b) no significant changes after cooling down below the superconducting transition temperature: no Meissner effect.

However, when we magnetically image the ab-plane at the sample border and cool the sample from 550 mK (above T_{SC}) in field (20 G) to the FM/SC state, we see modifications of the domain structure (see figure 6.37 (c) and (d) on page 110). These modifications can be attributed to Meissner expulsion. The fact that we do not observe any domain structure change at the sample center, but at the sample border indicates that the flux can be pinned in the sample center, e.g. by domain boundaries, while at the sample border the distance of vortices to cover to escape is shorter and thus the flux can be expelled.

6.6.4 Hysteresis

In figure 6.24 the hysteresis loop of the sample as measured by C. Paulsen is depicted. The The hysteresis loop closes itself below 200G, even though no saturation can be obtained for fields up to several teslas due to the itinerant ferromagnetism of UCoGe: As the field is increased the electrons carrying the magnetism are more and more polarized, as their moments cannot be easily quenched like local moments.

In order to obtain the first critical field one can look at the onset of non-linear behaviour of the virgin curve. Through careful examination of the data it can be concluded that no linear range for small applied fields exist, consistent with other measurements [123]. This would indicate that vortices are always present in zero field, suggesting a spontaneous vortex state.

To observe how UCoGe behaves microscopically when the field is increased, we have magnetically imaged the surface for different fields, after having cooled the sample without applied field. The

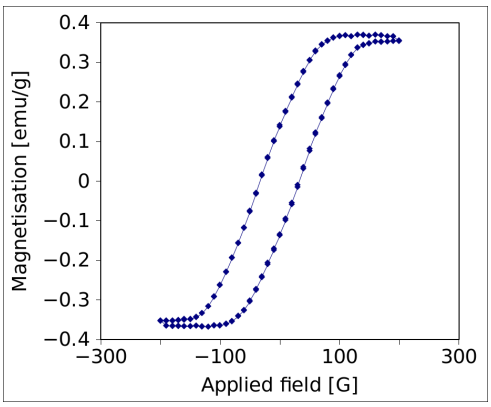

Figure 6.24: Hysteresis loop measured by C. Paulsen. This loop was used to choose a criterion for sample saturation: Above 200 G and below -200 G the sample is considered saturated for our local hysteresis measurements.

whole hysteresis loop was perused using a field of 200 G to saturate the sample.

One important issue is that once the critical field of our Al-SQUID is exceeded, we lose the capability of taking images. As a consequence, we cannot take images above the field of saturation.

Hysteresis, at border, imaging the ab-plane, field applied in c direction The sample is zero field cooled below T_{SC} and the field is increased until the SQUID stops working, the sample is saturated by setting the field to 200 G and the field is reduced below the critical field of the superconducting SQUID. Images are acquired at decreasing fields down to 0 G.

In figure 6.25 (a) the flux distribution above the **ab**-plane of the zero field cooled sample close to the sample border is shown (the dashed line at the top of each image represents the sample border). The sample's domain structure and stray field in the vacuum is clearly visible. The latter is a sign of magnetic field coming out of the **ac**-plane of the sample due to the roughness of the sample surface on the perpendicular face. When increasing the field up to 50 G (d) domain growth and merging can clearly be seen (as indicated by the rectangle). These domains get considerably bigger when the field is further increased up to 70 G (e). Outside the sample regions appear where the critical field of the Al-SQUID is locally exceeded leading to false measurements (see arrow). These false measurements regions dominate the image at 85 G (f) clearly indicating that the applied magnetic field is partially screened and thus stronger around the sample than directly above the sample.

Once the SQUID's critical field is exceeded, the sample is being saturated by applying 200 G. Images are taken at decreasing fields down to zero field. Due to the sample saturation the SQUIDs critical field is already exceeded in an applied field of 70 G (g). In (h) a diagonal line not visible before appears and horizontal ripples are observed. When the field is further decreased, vertical domains appear and grow. Image (j) is made at the same field as (i), but at an additional distance of 2 µm. At that distance high frequency information is lost, but the denser domain structure 50 µm away from the border is visible. In (l) no external magnetic field is applied and the domain structure is bigger than at the very beginning (a) due to the remanent field and the different histories. When warming up the sample above T_{SC} (m) the domain structure is modified and a slight field shift of less than 8 G occurs, again indicating field screening in the superconducting state.

Hysteresis, at the sample center, imaging ab-plane, field applied in c direction The same protocol as before was used at the sample center (see figure 6.26): the sample is zero field cooled and the field increased until 70 G while taking images, the sample is saturated with 200 G and images are acquired while decreasing the field to zero. The domain size increases with increasing

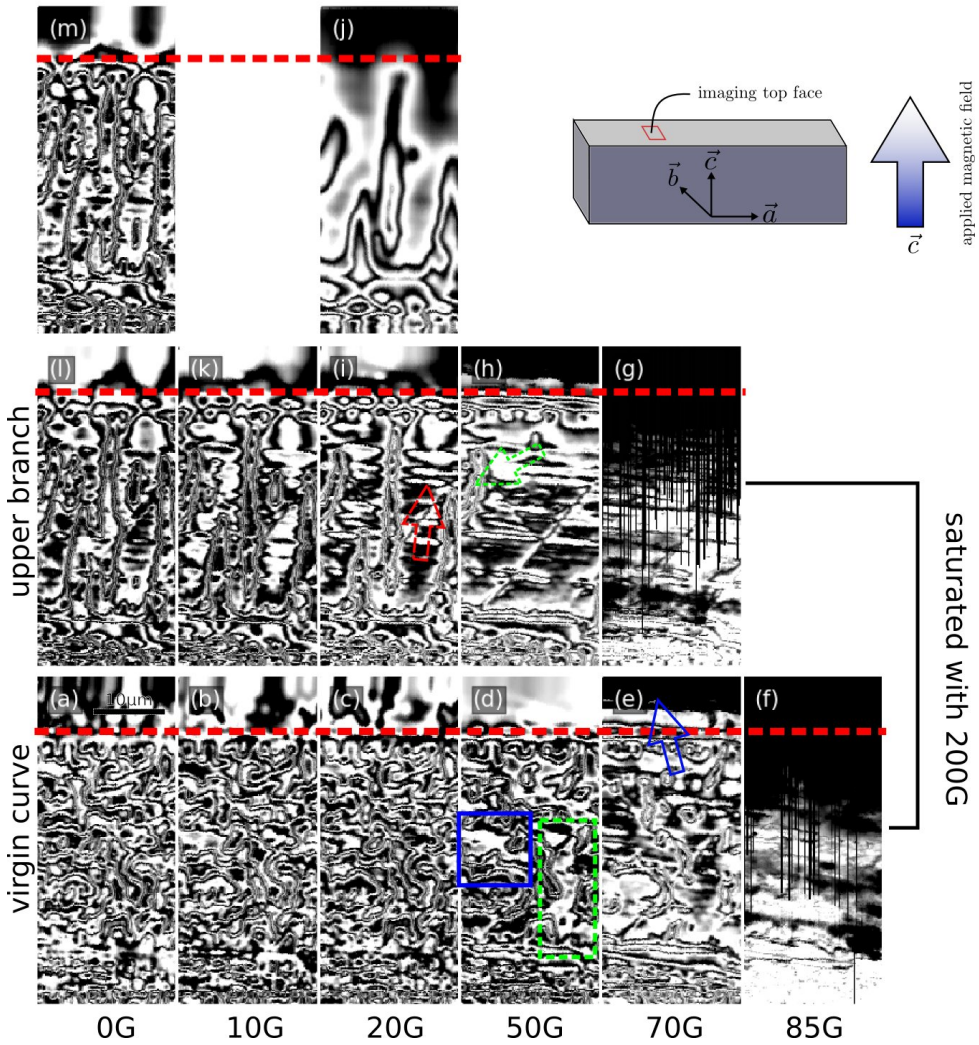

Figure 6.25: Field dependence of the domain structure in the **ab**-plane (T=250 mK). The dashed line corresponds to the sample border. In the first six images (a)-(f) the applied magnetic field is increased (following the virgin curve) from 0 G, 10 G, 20 G, 50 G, 70 G to 85 G. The vertical black lines in (f) and (g) correspond to fields higher than the critical field of the SQUID. After (f) the applied magnetic field is increased to 200G in order to saturate the sample and reduced to 70 G (g). (h) 50 G, (i) 20 G, (j) 20 G with additional 2 µm distance between SQUID and sample, (k) 10 G, (l) 0 G, (m) sample heated above T_{SC} (600 mK). When decreasing the field, we obtain first horizontal ripples and then vertical "fingers". When warming up (m) the domain structure and the internal field changes

applied field (a) - (d) and vertical regions with horizontal ripples grow when the field is reduced as the mono-domain breaks up along the **b**-axis.

The same procedure was followed for negative fields (see figure 6.27): The behaviour is similar. The first image of each series was made after zero field cooling (from the paramagnetic state, heating up above 3 K) the sample to the virgin state. As can be seen by comparing this ZFC image with figure 6.26(a), the domain structure is different. This shows that there are no preponderant nucleation sites as the ferromagnetic state forms.

Hysteresis, at the sample border, imaging ac-direction, field applied in b direction In the last two paragraphs we have seen how the magnetic domains behave in the **ab**-plane when applying

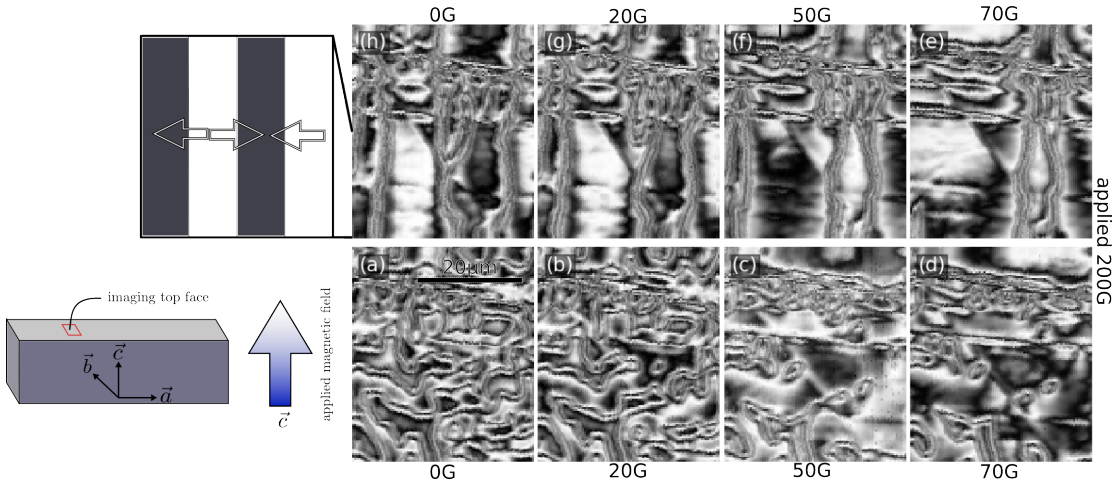

Figure 6.26: Hysteresis images (**ab**-plane, ZFC, T=200 mK) at the sample center. The applied fields (**c**) are given at top/bottom of the images. (a): After zero field cooling the obtained domain structure is different then in fig. 6.27 (a) - (d): the domain size becomes bigger as in fig. 6.27, but the domain structure differs from the other case. (e) - (h): when decreasing to the field to 0 G, the same behaviour as in 6.27 can be seen.

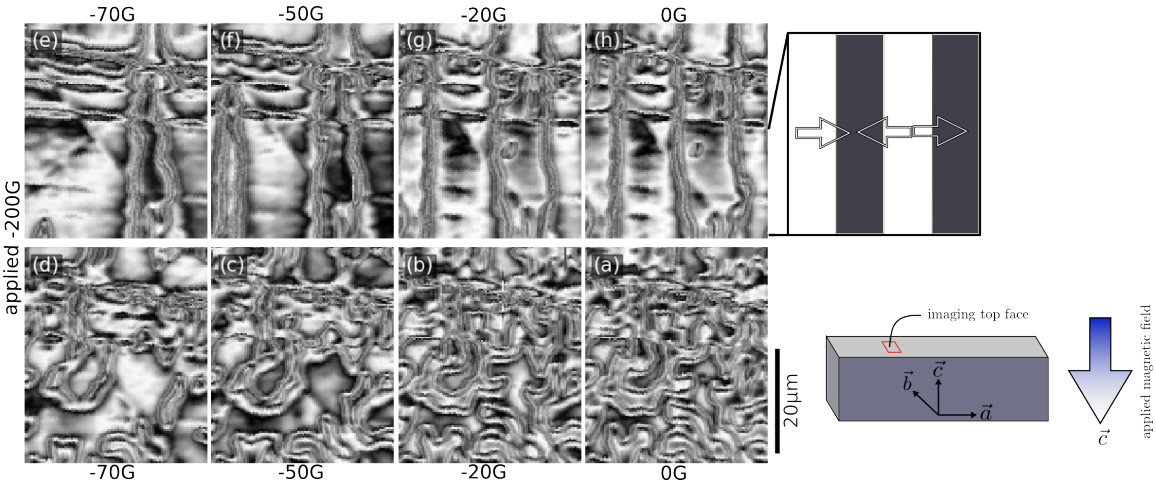

Figure 6.27: Hysteresis images (**ab**-plane, ZFC, T=200mK) at the sample center. The applied fields (**c**) are given at top/bottom of the images. (a) - (d): the domain size becomes bigger, (e) after saturation of the sample horizontal and vertical domains appear (compare with "fingers" at the sample border). The width of adjacent domains becomes similar at 0G (h)

a field along the easy axis of the uniaxial compound. Now, we will look at the **ac**-plane and apply a magnetic field in **b**-direction.

As can be seen in figure 6.28 larger domains are obtained when the field is increased. Once the sample is saturated, an almost homogeneous monodomain and the nucleation of a domain boundary that may grow during the scanning can be observed (d). The zoom in (e) shows the formation of a circular magnetic configuration. We suppose that the local moments turn into easy axis (**ac**-plane). The field range in these images (d) and (e) is about 1 G.

Compared to the field difference between two neighoring domains in **b**-direction of 16G this is very weak indicating that the signal comes from underneath the surface or that the magnetization turns only in a small volume at the surface. However, without information about the **a** and **c**-component of the magnetic field outside the sample, the interpretation of this phenomenon is rather difficult.

The domain boundary movement is expected in ferromagnets in a meta-stable state which occurs typically at sample inhomogeneities like a sample border where nucleation of opposite domains kicks in when the applied field is not high enough to stabilize a mono-domain and the stray field energy gets minimized.

Relaxation times of several hours are not unusual for ferromagnets at low temperatures. In reference [153] magnetization measurements over time of Mn_{12}, a molecular magnet of spin 10 which shows thermally assisted relaxation, are presented. At a sample temperature of 1.5 K the magnetization decreases about 0.7% in 19 hours. The relaxation time can be modelled with the Arrhenius law

$$\tau = \tau_0 \exp -E_a/k_B T \tag{6.17}$$

with τ_0 being the attempt rate to escape from a potential well, and E_a the activation energy needed to escape the potential well. At low temperatures the thermal excitation will decrease the escape rate and thus the system representing the local moments will stay in its current state.

In the case of UCoGe the relaxation of the magnetization may be due to switching of local moments from the **b**-direction to the easy axis (**c**-direction).

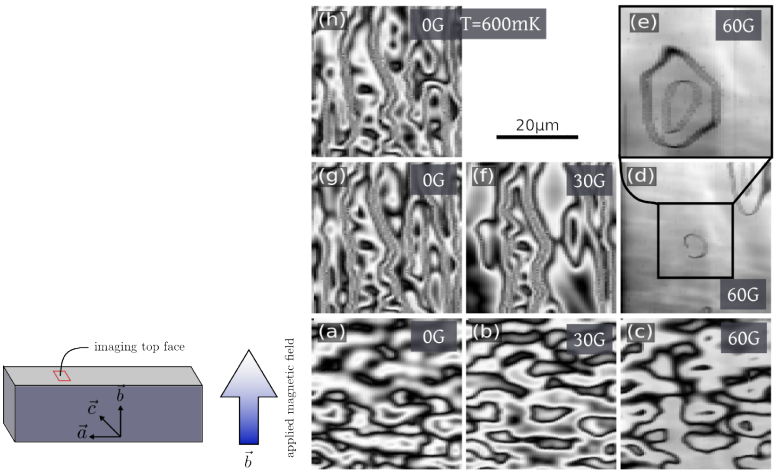

Figure 6.28: Hysteresis images (**ac**-direction, ZFC, T=200 mK) 40 µm from sample border. The magnetic field is applied in **b**-direction. (a) 0 G: the domain structure is rather horizontal, (b) 30 G, (c) 60 G, (d) the sample is saturated with 200G and then the applied field is decreased to 60 G: the sample becomes almost monodomain (field range: 1 G). (e) zoom on the marked region (field range: 1 G). The magnetic configuration evolves in time, (f) 30 G: after the break up of the monodomain state, the domain structure becomes vertical, (g) 0 G, (h) T=600 mK: changes in the domain structure.

When the applied field is reduced, domains aligned along the **c**-axis appear (g). When warming the sample up above the superconducting transition, the domain structure is modified by a changed field distribution which can be attributed to the vanished screening currents. Nevertheless, we cannot exclude other mechanisms for the small domain modification observed.

In figure 6.29 another example of the domain structure evolution in time is shown. This images series was taken after zero field cooling the sample to 230 mK, saturating it with -200 G, increasing the field to -60 G. An evolution of the field distribution is clearly seen between (a) and (b). This evolution took place during 13 hours. Between (b) and (c) 1 hour passed, the domain structure change is less important, but still clearly visible.

We also tried twice to observe this instability of the domain structure in the sample center, but over a timescale of 2 hours we could not detect any change.

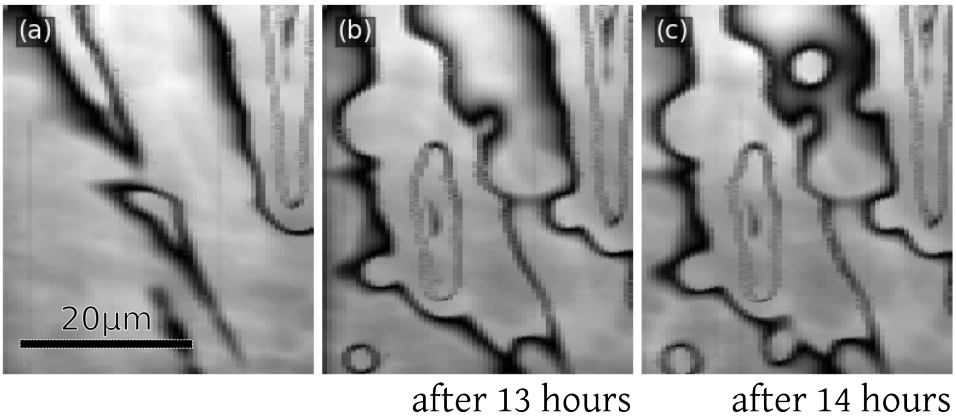

Figure 6.29: Image showing the evolution of the domain structure over time in the same configuration as figure 6.28. The sample was ZFC down to 230 mK, then saturated with -200 G. These images were taken at a field of -60 G. Time passed between (a) and (b): 13 hours, between (b) and (c): 1 hour. It is clearly visible that the domain structure changes considerably after 13 hours and that the evolution continues afterwards. The field range in all three images is 1 G.

Hysteresis, at the sample center, imaging ac-plane, field applied in b direction Now, we will be perusing the whole hysteresis loop at the sample center with an applied field perpendicular to the scanned surface (6.30):

The sample is zero field cooled to 600 mK (sample is in the normal state) and a field of 60 G is applied (a). A quite homogenous field distribution above the sample can be observed. The circular lines can come from a rotation of the magnetization parallel to the **b**-axis towards the **c**-axis. Then the sample is saturated with 200 G and the field is reduced to 60 G (b). This means that we leave the virgin branch for the upper hysteresis branch, the sample magnetization is even more homogeneous than in (a). After this no field is applied (c) and a dense domain structure is observed. By applying -60 G these domains become bigger (d) and by saturating again a homogenous state (e) is reached. At zero applied field the domain structure is different from the one on the upper hysteresis branch (c). When applying 60 G the domain structure becomes almost mono-domain again.

The domain structure at the remanent states (c) and (f) are different but are characterized by domain sizes of the order of 4 µm, the magnetization due to these domains is only ± 10G about a half of the magnetization along the **c**-axis.

6.6.5 Conclusion

In this section we have shown the different magnetic measurements of UCoGe for two different geometries (**ab**-plane and **ac**-plane).

We have shown that UCoGe can be considered a perfect Ising magnet with local moments aligned along the **c**-direction. After having programmed the random domain structure to better understand the experimental images, I realized that for an Ising magnet several topological different domain structure families can be distinguished (see figure 6.31):

Periodic lattices: In analogy with the n-fold axial symmetry (with $n = 2, 3, 4, 6$) in crystallography for points, we will generalize n to the case of domain structures. Note, that e.g. $n = 4$ does not mean that the system can be rotated by 90 degrees and is superimposes exactly the initial state. In (b) this is illustrated: By turning the domain structure by 90 degrees, we do not obtain an identical structure, but by sheering the initial state can be recreated.

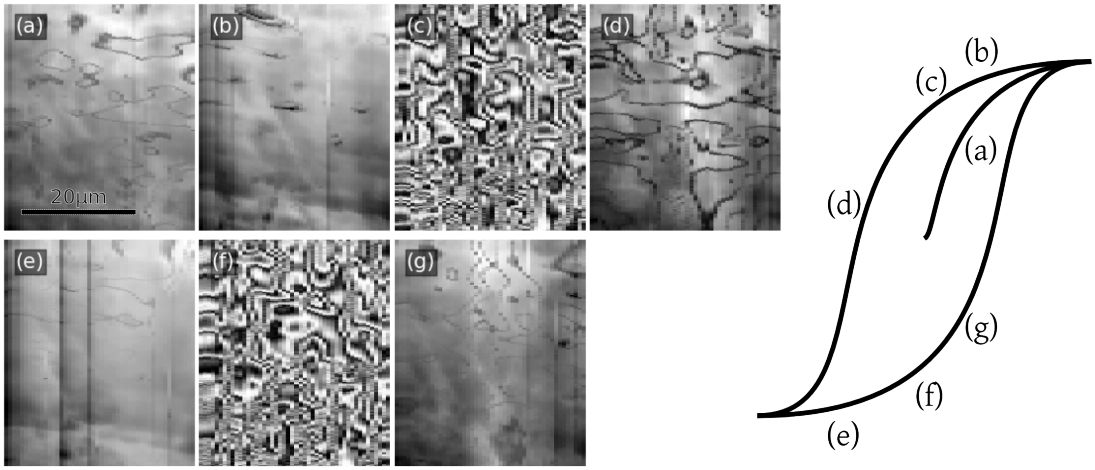

Figure 6.30: Hysteresis images (**ac**-direction, ZFC, T=600mK, field applied in **b**-direction) at the sample center: (a) 60 G, (b) saturated sample with 200 G and then went to 60 G, (c) 0 G, (d) -60 G: more domains than in (a), (e) -200 G to -60 G, (f) 0 G, (g) 60 G: the domain boundaries are not at the same position after one cycle than in (a): this means that the sample is rather homogeneous and does not trap boundaries.

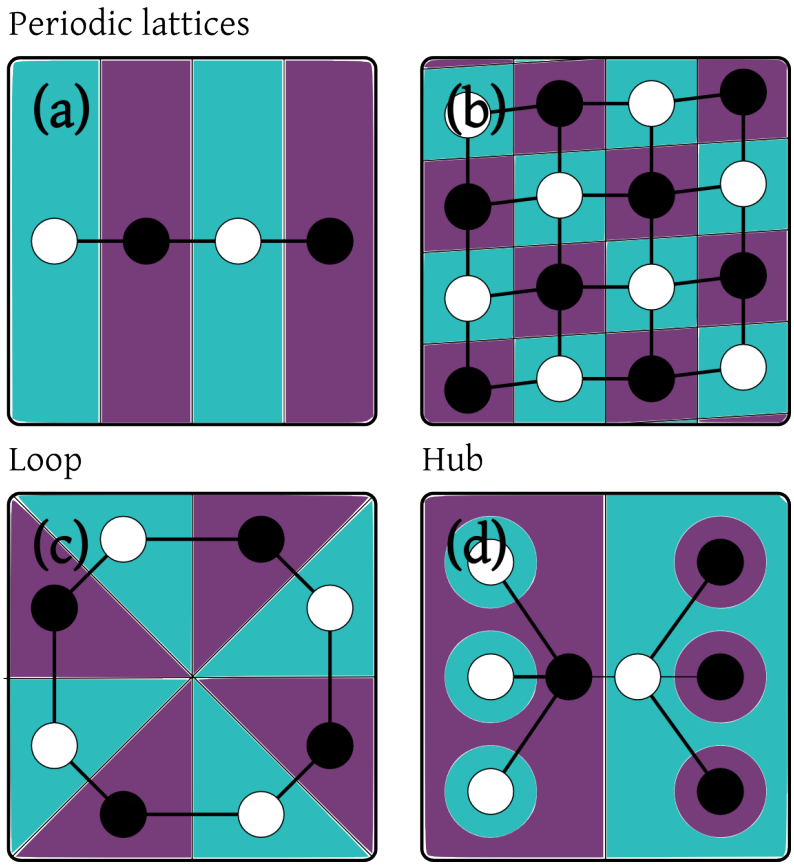

Figure 6.31: Different possible domain structures for an ideal Ising magnet. (a) The stripes represent the up and down domains, whereas the topological configuration is represented by the black and white circles. (b) A sheered square lattice. (c) A domain structure in which the domains all touch in a central point. (d) Islands of up domains embedded in a large down domain and vice versa.

The $n = 2$ case is depicted in (a). The stripes represent the ↑ and ↓-domains in real space, whereas the black and white circles represent the topological configuration. It is not possible with two different domains to create a triangular domain structure, as domains of the same magnetization would create stripes again. In the case of $n = 4$ (b) and $n = 6$ (not depicted), square and hexagonal lattices can be imagined.

Note, that the $n = 2$ case is used by Fauré and Buzdin for their free energy calculations that describe the variation of the domain size when crossing the superconducting transition temperature, while $n = 4$ is presumably realized at the sample center after the applied saturation field has been turn off (compare with figures 6.27 and 6.26). The structure grows of reversed domains nucleating at the sample border in the form of "fingers".

Loop: One can also imagine the domains to form a cake-like distribution, that would correspond topographically to a loop. In this case the domains touch in a central point in the sample. This case has not been observed.

Hub: Domains of the same magnetization can be isolated from each other by embedding them into a larger reversed domain. This situation is depicted in (d) and is realized in UCoGe when zero field cooling (virgin state). A more realistic representation of the same topographical configuration, corresponding to the experimental images, is shown in figure 6.32.

This list is not exhaustive as we have not considered more complex topologies, mixing of above examples and domain structures analogue to the Penrose lattice.

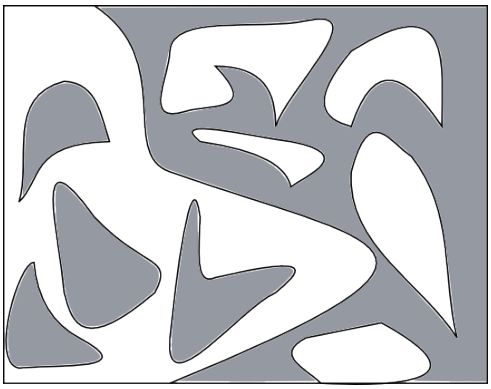

Figure 6.32: Illustration if the domain structure in the case of an Ising ferromagnet with a complicated domain structure. The only way to have isolated domains without using ordered geometries like stripes or a checkerboard with alternating domain magnetization is a configuration with islands of ↑-domains in a ↓-domain or vice versa.

We have shown the spontaneous magnetization of the sample by forming domains. We observed magnetic domains of different sizes ($\sim$ 10 μm). The magnetic field difference as determined by counting the number of minima and maxima of the critical current passed from one domain center to the next gives a value of ± 22.5 G. We compared this value with the magnetization measurements performed by C. Paulsen by either calculating the internal field (45 G for the local measurement and 52 G for the bulk measurement) or the external field (22.5 G and 35 G, respectively). Both measurements are in good agreement.

The fact that domains are also found in the **ac**-plane (with a magnetic field difference $2B_s$ of 16G) is probably due to the above mentioned domain reconstruction close to the surface and stray fields of domains magnetized along the c-axis. Furthermore, the roughness and overall convex shape of the surface due to polishing could be the origin of the complicated flux distribution on the **ac**-face.

Once UCoGe is cooled in zero field below its superconducting transition temperature and applied field is screened as can be clearly seen in the field shifts when warming up (**diamagnetic screening**).

These microscopic measurements are corrobated by bulk measurements of the ac-susceptibility, showing a nearly perfect diamagnetic behaviour.

In contrast the **Meissner expulsion** when first applying a magnetic field and cooling down the sample below T_{SC} afterwards does not yield any differences with the imaging technique having a spatial resolution of about 2 µm and a estimated magnetic sensitivity of 1 G. The nominal sensitivity is about 0.05 G/px but due to the high signals of the ferromagnetic domains, small changes are difficult to detect.

From bulk measurements the Meissner effect is expected to be of the order of several percent of the magnetization, thus the fact that the local scanning SQUID measurements with a magnetic resolution of about 3% of the magnetization cannot observe the field expulsion is in line with the bulk measurements.

The order parameter of adjacent domains with equal spin pairing is different, because the Cooper pairs of ↑ and ↓ domains are formed by two electrons with spin up and down, respectively. Consequently, both order parameters have to vanish at the domain boundary.

As we did not find descriptions in literature how the weak Meissner expulsion can be explained when taking into account the triplet nature of the superconductivity in UCoGe we considered two scenarios:

The first scenario is illustrated in figure 6.33. Below the superconducting transition temperature the internal field is expelled out of each domain, but due to cancellation of the expelled field inside the sample, Meissner effect is only measurable for the outer domains and thus very weak (around 3%, see figure 6.18). By taking an average domain size of 10μm the bulk field expulsion can be estimated to be $1 - \frac{1/2 \cdot ((290-20)\times(1110-20)\mu\mathrm{m}^2)}{290\times1110\mu\mathrm{m}^2} \approx 4\%$ (the factor 1/2 stems from the fact that only half of the field is expelled outside the sample).

While this scenario explains why no flux change at the domain boundary is observed (with a magnetic resolution of 2 G) it is not in line with local measurements above the domains themselves which do not show any flux change.

The second scenario is a spontaneous vortex state: When cooling down the sample below T_{SC} the applied field will be concentrated in vortices and all the vortices will remain pinned in the domains. The limited spatial resolution of our SQUID will not allow to make a difference between flux and flux tubes in the case of a high vortex density combined with a large penetration depth. This will be discussed in more detail in the next section.

In the case of localized magnetism it would furthermore be difficult to imagine a mechanism involving superconductivity which can account for a change in the internal field. In the case of the itinerant ferromagnetism in UCoGe this seems more plausible as the same electrons are responsible for the magnetic and the superconducting properties. At the moment the superconducting pairing mechanism is not known in detail, so we will not further speculate on this matter.

We have also performed local measurements of the domain structure while perusing the **hysteresis** loop. The general behaviour of the domains corresponds to the expected behaviour: when increasing the applied field, domains grow. The compound can be "saturated" by applying 200G. When the upper hysteresis branch is followed from high fields to zero fields, domains reverse and grow. This behaviour is similar for negative and positive applied fields and for the two geometries measured (**ab** and **ac**-plane).

However, two interesting features can be noticed: First, the reversed domains when scanning the **ab**-plane are narrow domains with their largest dimension along the **b**-direction. Once these domains are established and the field further reduced they get wider to the cost of the original domains. The second interesting feature is the relaxation time for the reversed domains at the border, which is of the order of hours. This is probably due to the low thermal energy of the system at temperatures

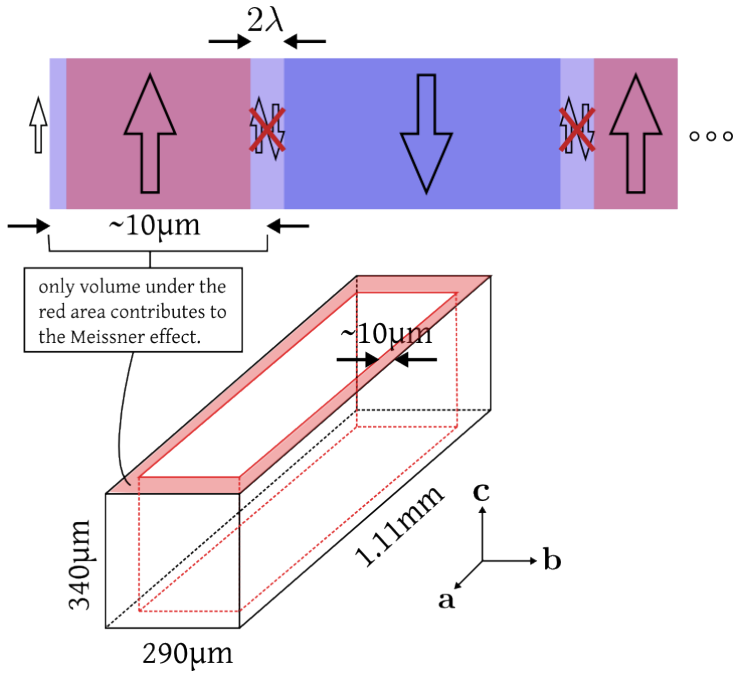

Figure 6.33: Illustration of a simple scenario explaining the weak Meissner expulsion. As the internal field is expelled during the superconducting transition fields of opposite domains in the inside of the sample cancel out. Only the domains at the border are accessible to macroscopic measurements. In the case of our sample with an average domain size of 10 µm this would lead to a Meissner effect of the order of 4% of the magnetization. This value is consistent with the measured 3%. However, local measurements do not find any indication of a reduced magnetization of the domains.

around 200 mK.

6.7 Vortex lattice

6.7.1 Introduction

As UCoGe is a superconducting ferromagnet the question arises whether the spontaneous magnetization creates a spontaneous vortex state. During the imaging of the magnetic configuration along the hysteresis loop, we could not resolve vortices, even when the domain structure was almost homogenous. Furthermore, even scans on the **ac**-plane with a lower magnetization did not put forth any vortices.

We want to estimate the experimental conditions needed to address the question of the existence of a spontaneous vortex state (SVS). The first condition for a SVS is that the superconductor cannot shield the magnetic field ($H_{c1} < M_s$). This is corrobated by the fact that bulk magnetization measurements do not show any sign of the first critical field (see figure 6.34). Normally, the slope of the magnetization decreases linearly until H_{c1} is reached and then the penetrating field is responsible for an upturn. In the case of UCoGe no such linear regime is found.

If the superconductor could shield the magnetization of each domain SQUID microscopy would have observed huge changes in the magnetic surface state upon warming up or cooling down through T_{SC}.

As we do not observe strong flux reorganisation on each domain, H_{c1} must be smaller than the magnetization and superconductivity has to form a SVS, compressing the flux into flux tubes carrying

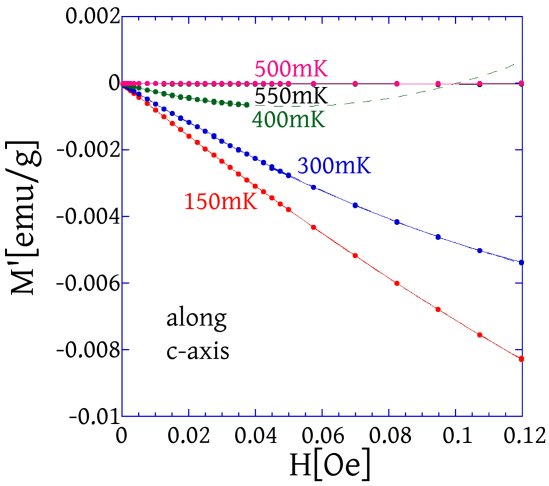

Figure 6.34: Search for H_{c1}. Normally, close to the beginning of the virgin hysteresis curve a linear regime can be found attributed to the Meissner state. In the case of UCoGe no linear regime exists, indicating that H_{c1} must be smaller than $4\pi M_s$. Measurements performed by C. Paulsen.

each a Φ_0 of flux.

In the following we will address vortex imaging in UCoGe in more detail using numerical calculations developed in collaboration with J. Kirtley. As a result, we will show that the spatial and magnetic resolution needed is not attained by our microscope. Typically, fields much higher than 100 G are needed to obtain a **vortex lattice**. This is because the inter-vortex distance has to be small enough in order to make inter-vortex interaction dominate over vortex pinning. On the other hand, it will not be possible to resolve the field modulations created by the lattice when the lattice parameter a becomes much smaller than the SQUID size r.

In the following we will simulate the resulting images of our microscope when scanning over a perfect and a disordered vortex lattice.

6.7.2 Perfect vortex lattice

As the sample thickness of our sample $d = 340$ µm is much larger than λ, we will calculate the field above a vortex using the following formula [91]:

$$h_z = \frac{\Phi_0}{2\pi\lambda^2}\int_0^\infty dk \frac{kJ_0(kr)}{k^2+\lambda^{-2}} \frac{\sqrt{k^2+\lambda^{-2}}}{k+\sqrt{k^2+\lambda^{-2}}} \exp(-kz) \tag{6.18}$$

we can create a perfect hexagonal vortex lattice by superposing the individual vortex field distributions. Then we can simulate the corresponding critical current images taken by our SQUID and compare the amplitude of the critical current modulations against our sensitivity.

We use equation 6.18 instead of 4.7 because it is more convenient in this case (for programming purposes).

In figure 6.35 the field distribution (a) and the flux through the SQUID (b) is depicted (both at a height of 0.4 µm) for the case of a vortex lattice in an external field of 22.5 G (corresponding to the field due to the magnetization of UCoGe along the **c**-direction at 200 mK as observed by domain imaging), a penetration depth of 0.1 µm. The penetration depth was taken one order of magnitude

smaller than predicted above and the resulting field distribution will be compared to a the one corresponding to a λ of 1 µm. Field modulation is 5.32 G resulting in a flux modulation measured by the 1- µm-SQUID of $137.5 \times 10^{-4}\Phi_0$.

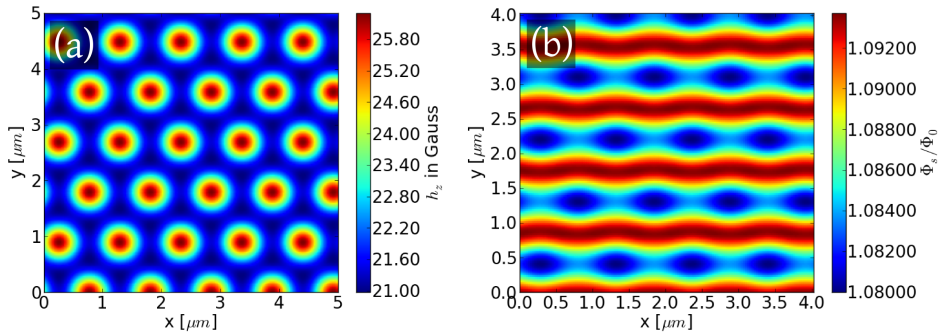

Figure 6.35: (a) field distribution above a vortex lattice with lattice parameter $a = 1.06$ µm (corresponding to 22.5 G) and $\lambda = 100$ nm at a height of 400 nm. (b) resulting flux distribution through a 1 micron SQUID. Note that the modulation is only 137.5 $\times 10^{-4}\Phi_0$

In table 6.1 we have summarized the field and flux modulations for different penetration depths (0.1 and 1.0 microns) and SQUID sizes (0.5 and 1.0 microns). The reason for the flux modulations of the 0.5 µm SQUID are smaller than the modulations for the 1.0 µm SQUID is due to the decreased signal ($\propto$ SQUID area). However by reducing the SQUID/sample distance the vortex lattice with a lattice constant of a=1.06 µm is easier to observe with the smaller SQUID as it can better probe the minima and maxima in the field distribution, while the bigger SQUID is averaging over both.

The experimental conditions are met by the case of a 1-micron-SQUID and a penetration depth of 1 µm. The flux modulation is about $3.5 \times 10^{-4}\Phi_0$ thus of the same order as the sensitivity per second as determined in chapter 2: This means that the vortex lattice would not be seen by our microscope without further effort: Either by increasing the integration time to several seconds per pixel, leading to scanning times in the order of weeks and $1/f$-noise, or increasing the magnetic and/or spatial resolution of the SQUID as discussed in the outlooks of chapter 2.

Table 6.1: The field and flux modulations at a height of 0.4 microns for different penetration depth and SQUID sizes. The applied magnetic field in all cases is 22.5G.

λ [μm]	SQUID size [µm]	field modulation Δh_z [G]	flux modulation [$\Phi_0 \times 10^{-4}$]
0.1	1.0	5.32	137.5
1.0	1.0	0.14	3.45
0.1	0.5	5.32	354
1.0	0.5	0.14	9.12

6.7.3 Disordered vortex lattice

The next idea is that the vortex state can be disordered due to the small field of 22.5 G, the inhomogenous field of the domains and the fact that the penetration depth is only about one order of magnitude smaller than the average domain size.

As a consequence we calculated the field distribution for a disordered lattice. First a perfect lattice was generated, then we changed the position of the vortices with a standard deviation of $10\% \cdot a$ (a denoting the lattice constant) (see figure 6.36(a)).

Examples of the flux penetrating two different SQUIDs (0.5 and 1.0 microns) for an applied field of 22.5 G and at a height of 400 nm are depicted in figure 6.36 (b) and (c). Even when analyzing the original field distribution (a) the vortices are hard to distinguish. This gets even harder with the finite resolution of the SQUID.

Furthermore, we generated a field distribution image for a lattice in which we removed 5% of the vortices randomly. The resulting field image is shown in figure 6.36(d). In this case the field variation is dominated by the interstices in the vortex lattice and sole vortices cannot be resolved.

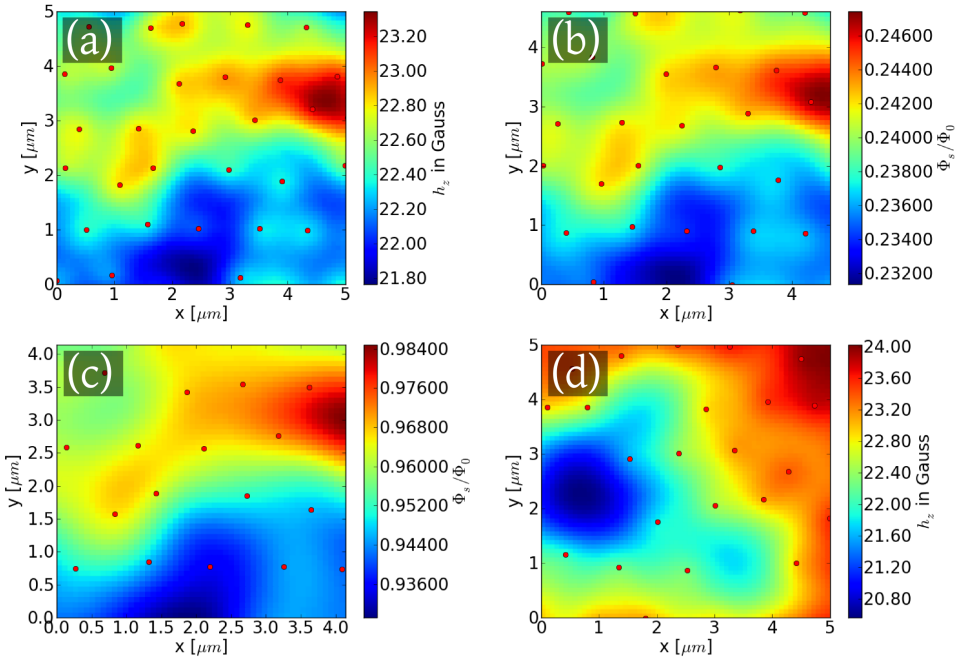

Figure 6.36: Disordered vortex lattice (height from sample surface is 400 nm, the applied field is 22.5 G). (a) the field distribution of a vortex lattice with a vortex displacement from the ideal position of 10% of the lattice constant. (b) the corresponding 0.5-micron-SQUID image. (c) the corresponding 1.0-micron-SQUID image. (d) the field distribution for a vortex lattice with 5% interstice. The dots corresponds to the position of the vortex core. The interstices dominate the field variation and sole vortices cannot be resolved.

It is important to note that the background in these simulations is perfectly flat, in contrast to the situation in UCoGe where the background is complex due to the magnetic domains. This inhomogenous background further increases the difficulties to observe a vortex lattice with these specific properties (a, λ).

It is as well difficult to image an isolated vortex in UCoGe, as could be supposed in the case of local disorder of the lattice. This is due to the fact that the disorder is dominating the magnetic flux.

6.8 Behaviour of domain walls

As we have seen in the previous chapter theoretical predictions for superconducting ferromagnets state that the domain structure should become smaller when the sample undergoes the superconducting transition. UCoGe is with URhGe the only uranium based superconducting ferromagnet that exhibits coexistence of ferromagnetism and superconductivity at ambient pressure making its study by our microscope feasible. We have tried several ways to detect a clear difference between the SC and the normal state.

First, we tried simply to field cool the sample and to analyse the differences in images taken before and after the superconducting transition. As was discussed before, we did not succeed in finding any significant difference. Second, we zero field cooled the sample and applied a field in the superconducting state taking an image. When warming up the sample we were capable to see differences in the sample, but only when the images where taken close to the sample border. This protocol was the *only one* that allowed us to observe changes of the domain size.

The fact that the domain sizes change close to the sample border is an indication that the domain reconstruction was due to changes in the local field due to setting in of screening currents leading to domain reconstruction at the border. The sample edge is also a region where magnetic instabilities are expected what may amplify the effect of the screening currents. The domain structure in the center of the sample was found to be stable during imaging above the **ab** and **ac**-planes.

6.8.1 Field cooled

When we were discussing the Meissner effect in section 6.6.3 we have already seen (see figures 6.21, 6.23, 6.22), that field cooling the sample does not affect the domain structure and consequently the domain size at the center of the sample. These field cooling experiments were done for 5 G and 10 G for the **ab**-plane and the **ac**-plane, respectively. In the latter case the field was applied along the **c** or along the **b** axis.

According to the theoretical prediction the domain size should change. We would then expect some domains to move in order to fill the gaps left by the shrinking domains. Even a 1% domain size change would lead to the generation of new domains at the sample border. Another solution for domain size shrinking would be the splitting of domains. Neither is observed.

Here we want to discuss another deficiency of the theoretical model put forward by Fauré and Buzdin [118]: In their model all domain stripes have the same width l_N in the normal state and shrink to the width l in the superconducting state. This model based on free energy calculations naturally cannot predict how the domain size will change. But as only domain size changes of a factor of two can be realized by splitting, domain wall movements seem more adapted. However, intuitively breaking up of domains seems more realistic considering domain wall pinning.

6.8.2 Border

As was explained already we tried to find an temperature dependence (SC state/N state) of the domain size. The only way we could observe a change was by zero field cooling the sample, applying a field below T_{SC}, taking an image and comparing this with an image taken after warming up above the superconducting transition temperature.

In figure 6.37 the sample was zero field cooled to 200 mK. The dashed line corresponds to the sample border. Once at 200 mK we apply a field of 20 G in the **c**-direction. You can see that the color in the image (b) changes and that some domain boundaries move. Then we warm the sample up above the superconducting transition temperature (c). Here we marked the domains that break up into several smaller ones (see circles). When we cool the sample down again (d), at least one domain (rectangle) merges with a neigboring one. This may be due to flux expulsion at the sample border as discussed in section 6.6.3.

Another example of this domain size change is depicted in figure 6.38. When comparing the image at $T < T_{SC}$ (a) with the one at $T > T_{SC}$ (b) we see that two big domains break up into smaller ones (see added curves). These images were taken 30 μm from the sample border.

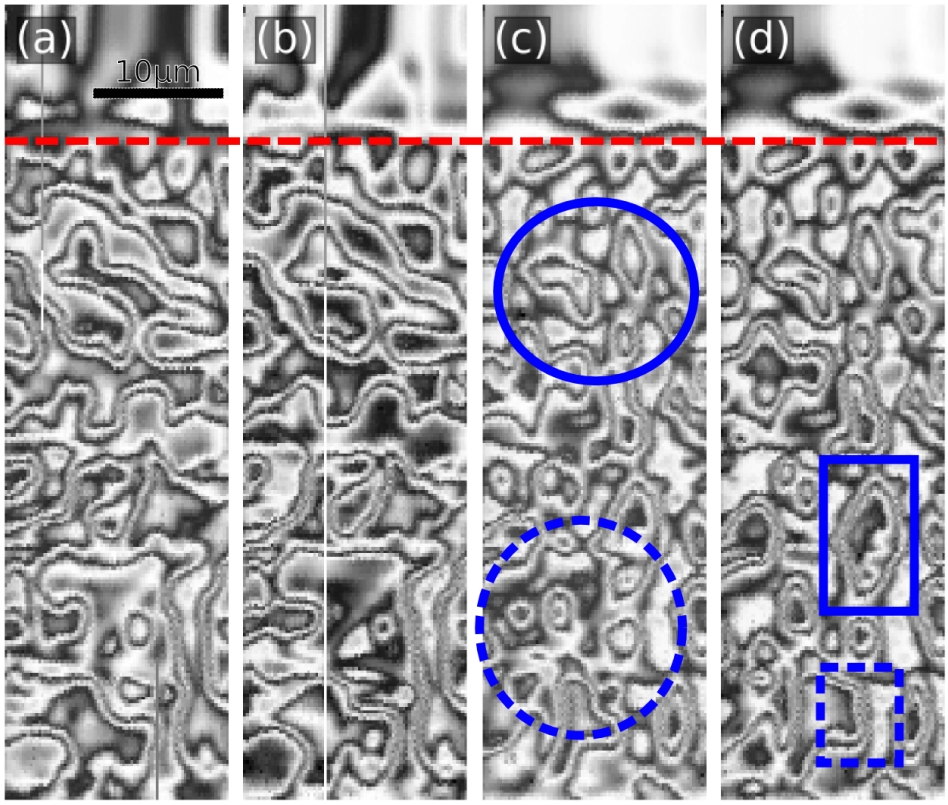

200mK, ZFC 200mK, 20G 550mK, 20G 200mK, 20G

Figure 6.37: Imaging **ab**-plane: (a) ZFC to 200 mK, (b) applied 20 G in **c**-direction, (c) warming up above T_{SC} to 550 mK. One can clearly see that the average domain size decreases. The circles mark regions where one big domain has broken up into several smaller ones. (d) cooling down to 200 mK again: the in-field domains become bigger due to screening.

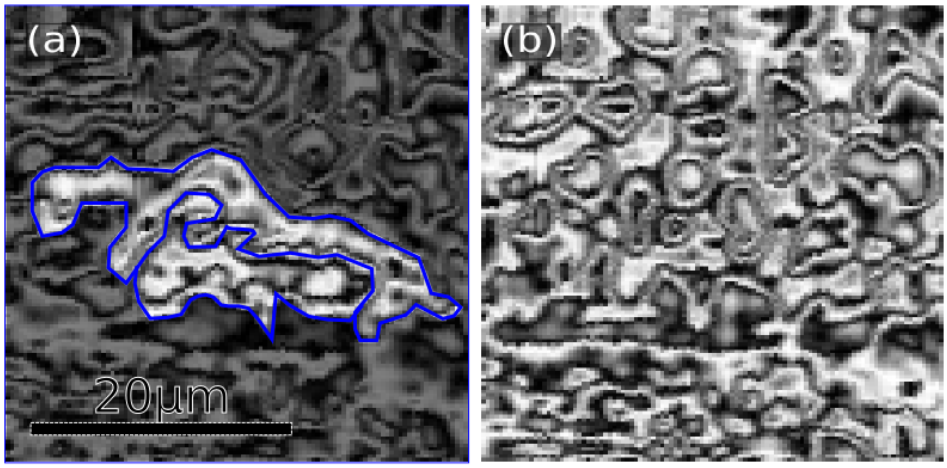

Figure 6.38: Imaging **ab**-plane (top of images is 30 µm from sample border): (a) ZFC to 200 mK and then applied 10 G in **c**-direction, (b) warmed up to 600 mK. It can clearly seen, that the two domains highlighted in (a) break up into smaller ones.

6.8.3 Center

In order to study whether other origins of the domain reconstruction than the field gradient at the sample border may be present, we undertook the same cycle at the sample center. The results can

be seen in figures 6.39 and 6.40, for 20 G and 10 G respectively. In both cases we were imaging the ab-plane and applying the magnetic field perpendicular to it.

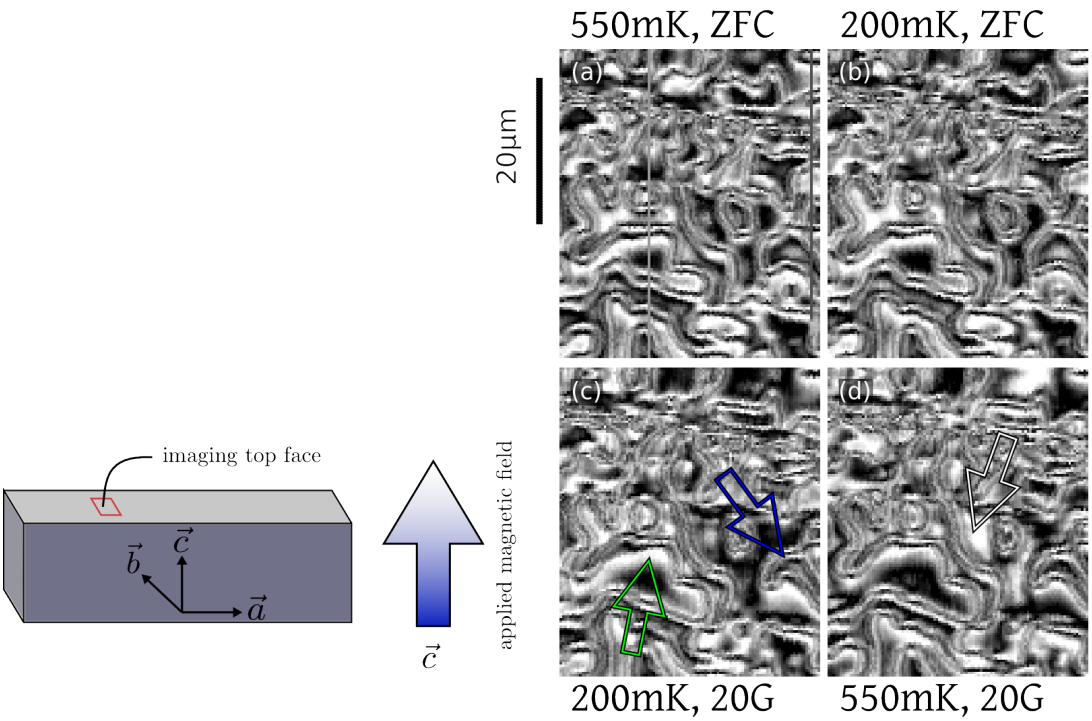

Figure 6.39: Imaging **ab**-plane: (a) ZFC to 550 mK, (b) cooling further to 200 mK, (c) applying 20 G in **c**-direction, (d) warming up to 550 mK. When we apply field, we see the some domains shrink and some grow, but when warming up above the superconducting transition temperature the domain size does not change. There is however a field shift due to the penetrating field.

In the first case you can see a difference between step (b) and (c) when we apply a field. This change is due to the local magnetic field penetrating at the domain walls (see section 6.6.3). The domains framed by rectangles change their dimensions. But when the sample is warmed up above T_{SC} the domain structure does not change and we only see a slight field shift that apparently is not strong enough to force domain boundaries to move. This shift can be explained by the penetration of the field as it expands from the inter-domain space into the domains.

Exactly the same conclusion can be drawn when analysing figure 6.40, the only difference being that an applied field of 10 G is not enough to make the domain boundaries move (b) below T_{SC}.

6.8.4 Discussion

As we have seen, the domain size only varies close to the sample border (several 10 µm) when applying a field in the superconducting state and warming up. In constrast the same procedure at the sample center does not provoke changes in the domain structure, but only field shifts. The reason for that can be that the sample border is more sensitive to the interplay between the applied field and the superconducting surface.

As was already mentioned the theoretical model does not take domain wall pinning into consideration, furthermore due to the nature of the calculations, using free energy and thus only considering equilibrium states, it is not clear what kind of dynamic domain behaviour to expect (domain movement, domain breaking). The equilibrium state assumption is not met in our measurements as we did not use any shaking fields. It is also possible that the complicated domain structure (compared

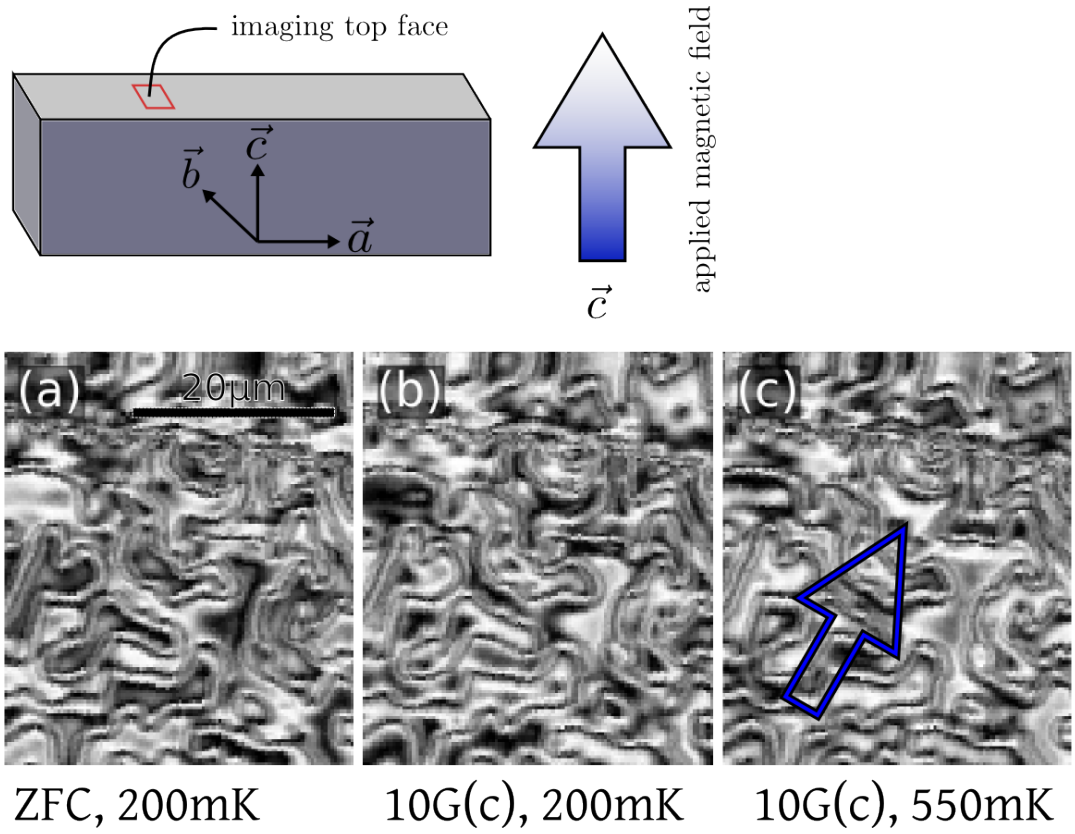

Figure 6.40: Imaging **ab**-plane: (a) ZFC to 200 mK, (b) 10 G in **c**-direction applied, (c) warmed up to 550 mK. The domains do not move. The only change visible in the images is due to a homogeneous field shift

to the stripes used in the model) is far off the global free energy minimum configuration and that as a consequence the system is stuck in a local free energy minimum configuration.

As a last point it should also be noted that the geometry used by Fauré and Buzdin [118] does not consider effects at the sample border as the domains are magnetostatically less stable and are thus more sensitive to the effects of the superconducting screening currents.

6.9 Conclusion

We have presented the **first real space images** above the surface of a superconducting ferromagnet. The spontaneous forming of the ferromagnetic state was shown. The domain size is of the order of ~ 10 µm, the magnetic field difference B_s along the **c** and **b** were quantified as 45 G and 16 G with scanning SQUID microscopy. The former one being in good agreement with bulk magnetization measurements performed by C. Paulsen that find a magnetic field at the surface of 35 G along the **c**-axis for $T \to 0$. This spontaneous magnetization is in line with most publications, but in constrast to [132].

We have estimated the domain wall width d to be smaller than 5.3 Å and have given a upper limit of 1 µm for d. Experimental results suggest the domain reconstruction happens at a depth of around 100 nm or less, based on the good agreement of the local and bulk magnetization, making UCoGe a **perfect Ising magnet**.

We also confirm **local coexistence of superconductivity and ferromagnetism** as diamagnetic screening is observed. As was shown by bulk magnetization measurements the Meissner effect

is very weak (around 3%). This was confirmed by our scanning SQUID measurements in which no difference between the superconducting state and the normal state was detectable within the sensitivity of the probe (about 1 G magnetic resolution and 2 μm spatial resolution) on the local scale at the center of the sample. However, a weak domain structure modification is observable at the sample edge which can be attributed to easier flux expulsion at the sample edge compared to the center with probable pinning of flux at domain boundaries.

The absence of a linear regime indicating the first critical field on the virgin curve of magnetization strongly suggests a **spontaneous vortex state**. However, we have shown that the spatial and magnetic resolution of our microscope in combination with the internal magnetic field makes it very difficult to observe vortices with the current setup. For a confirmation of the spontaneous vortex state a higher spatial resolution is needed. Furthermore, the detection of vortices would be much easier with a linear signal that can be obtained with a shunted SQUID and feedback. This would increase the magnetic resolution considerably as the signal would not be perturbed by the complex background in form of domains and images could be subtracted from each other.

Studies along the hysteresis loop showed the expected general behaviour for a ferromagnet. When the applied field is increased the domain size grows, when field saturated we obtain a mono-domain. This mono-domain breaks up once the field is reduced. When scanning above the **ab**-plane the reversed domains start to grow along the **b**-direction and increase their width along the **a**-axis afterwards. At the sample border domains reverse spontaneously in the course of several hours attributed to thermal relaxation as described by the Arrhenius law, though we do not know the parameters yet.

We have clearly shown that the theoretical model proposed by Fauré and Buzdin [118] predicting a **shrinkage of the domain size** when cooling the sample below T_{SC} **is not realized**. Several reasons for this discrepancy have been discussed.

We have shown on several occasions that the **sample quality** is good: The RRR is 19 and the specific heat measurements are similar to the best samples in literature. The critical current measurements show that vortex pinning is very weak, thus the sample homogeneity is very good (critical current $\sim$ 250 A/cm^2 at 100 mK). Repeated cooldowns in the ZFC state produce different magnetic configurations. Furthermore, the domains relax slowly when the applied field is decreased from the saturation field, a sign that the domain wall can move even at such low temperatures.

6.10 Outlook

UCoGe involves very interesting physics. A lot of parameters, like the magnetic anisotropy, are unknown. There is a lot of work to be done. In the case of magnetic imaging and especially for our SQUID microscope the current challenges are, to improve the **spatial resolution** (smaller SQUIDs) and to use a feedback for the SQUID, thus having a **linear signal/field dependence** instead of a periodic one.

With these improvements it would be possible to visualize vortices and the above analysis of Meissner effect and domain size could be more precise as the possibility of subtracting images from each other permits to see differences more clearly. The linear signal/field dependence could also be achieved by using a Hall probe.

Conclusion

In this thesis we have presented the work of three and a half years consisting of the development of a scanning SQUID/AFM microscope and the measurements performed with this instrument on different samples.

The performance of the microscope is unique as we can take topographic and magnetic images simultaneously with a sub-micron resolution for the topographic images and a SQUID dependent spatial resolution for the magnetic images. This is achieved by using a tuning fork as a force sensor. Two cascading PI controllers are used for the tip/sample distance regulation. The SQUID is attached on top of the force sensor. The obtained magnetic resolution of the SQUID is of the order of $10^{-4}\Phi_0/\sqrt{\mathrm{Hz}}$, enabling us not only to observe vortices, but also to determine the absolute value of their penetration depth. During this thesis we have used SQUIDs of different sizes 1.1 μm and 0.6 μm. The principal long-term effort at the moment is the development of shunted niobium SQUIDs that would increase the magnetic sensitivity by at least one order of magnitude and a new SQUID tip geometry allowing for a SQUID/sample distance of only 50 nm. This reduced distance makes it possible to use SQUIDs with a diameter of 200 nm,a feature which other groups (K. Moler and E. Zeldov) try to obtain, by using a much more complicated SQUID design or fabrication process.

The sample temperature range in which the microscope can operate is, at the time of writing, between 200 mK and 10 K. It is planned to increase the upper bound in the coming months.

In order to examine different spots on a sample surface, the microscope is capable of changing the position of the scanning area, which is 70 μm × 85 μm, on a millimeter scale with slip and stick motors (attocube).

A considerable time was being devoted to the electronics and the control software. The control software was also adapted to a room-temperature scanning Hall probe microscope built by Piotr Łaczkowski and used by Mikhail Kustov for measurements on magnetically patterned samples [**?**] [154].

The hardware of the microscope presented in this work itself underwent several iterations of improvement to obtain a robust and reliable device. These and other improvements have influenced the design of the third-generation scanning SQUID microscope built by Zhao-Sheng Wang that is not yet finished as of now.

In comparison to other scanning microscopes the main advantages of our design is clearly the simple SQUID design, making it possible to easily mass-produce SQUIDs (several hundred per wafer) that can be either cut or etched to obtain tips. The robustness of the regulation allows us to take images with the same tip for several weeks or even months.

As for the experimental results presented in this thesis, we have demonstrated the possibility of taking topographic and magnetic images on a nano-structured niobium film simultaneously, thus making the the microscope a well-adapted instrument for mesoscopic magnetic measurements.

In the case of rhenium we have shown that single vortex manipulation and characterization is possible. The manipulation is due to SQUID/vortex interaction can furthermore be turned on and off by changing the scanning height. By determining the critical height, we were capable of measuring the pinning force $F = 3.9 \times 10^{-16}$ N acting on a single vortex.

We have explained in much detail how scanning SQUID microscopy allows for obtaining an absolute value for the penetration depth. In the case of rhenium the penetration depth was found to be 79 nm. Compared to scattering techniques our method not only allows for a more direct measurement (real space instead of momentum space), but can also be used with different experimental constraints (small samples, low field) making it a versatile instrument for physics not accessible to scattering techniques.

Finally, we have for the first time shown local measurements of the domain structure of the superconducting ferromagnet UCoGe and determined the average domain size in the virgin state (10 μm). By magnetic imaging we were capable of determining the magnetic field difference above opposite domains along the **c**-axis to be 45 G and 16 G along the **b**-axis. Due to these magnetic field measurements we were able to give an upper limit for the domain wall width (∼1 μm) and domain reconstruction depth (100 nm). This is supported by simple calculations leading to a domain wall width of several angstroms. Thus UCoGe can be considered an ideal Ising ferromagnet. Different possible domain structures for an Ising ferromagnet have been discussed. The complicated domain structure found in the zero field cooled virgin state corresponds to up domains embedded in larger down domains and vice versa.

We have shown evidence for coexistence of superconductivity and ferromagnetism. The weak Meissner effect can be explained by a spontaneous vortex state, put forward by other groups [123], [136]. Numerical simulations suggest that the strong magnetic background signal and the limited spatial and magnetic resolution of the used SQUID made it difficult to resolve the expected spontaneous vortex state.

The relaxation of the domain structure over a time scale of hours was observed. More work needs to be done to clarify the reason of this relaxation taking place at temperatures below 1 K.

We showed that the theoretical prediction of domain shrinking, put forward by Fauré and Buzdin, when the sample temperature decreases below T_{SC} cannot be applied in its state to the case of UCoGe and discussed several reasons for this.

The microscope developed during this thesis will be used for probing different samples from NbS_2 to iron-based high-temperature superconductors. Only minor changes in the thermalisation will be needed in order to make the temperature range up to ∼ 30 K accessible. Several short-term improvements have been mentioned that will allow for, e.g. higher imaging speed and a reduced SQUID/sample distance.

Bibliography

[1] K. Onnes. The superconductivity of mercury. *Leiden Comm.*, 120b, 1911.

[2] Dr. Achim Marx Prof. Dr. Rudolf Gross. Festkörperphysik.

[3] R. Ochsenfeld W. Meissner. Ein neuer effekt bei eintritt der supraleitfaehigkeit. *Naturwissenschaften*, 21:787, 1933.

[4] H. London F. London. *Proc. Roy. Soc. Lond.*, A149:71, 1935.

[5] L.D. Landau V.L. Ginzburg. *Zh. Eksperim. Teor. Fiz.*, 20:1064, 1950.

[6] A. A. Abrikosov. *Zh. Eksperim. Teor. Fiz.*, 32:1141, 1957.

[7] J.R. Schrieffer J. Bardeen, L. N. Cooper. Microscopic theory of superconductivity. *Phys. Rev.*, 106:162–164, 1957.

[8] J.R. Schrieffer J. Bardeen, L. N. Cooper. Theory of superconductivity. *Phys. Rev.*, 108:1175, 1957.

[9] H. Fröhlich. *Phys. Lett.*, 79:845, 1950.

[10] H. Fröhlich. Isotope effect in superconductivity. *Proc. Phys. Soc.*, A63:778, 1950.

[11] E. Maxwell. Isotope effect in the superconductivity of mercury. *Phys. Rev.*, 78:477, 1950.

[12] W.H. Wright L.B. Nesbitt C.A. Reynolds, B.Serin. Superconductivity of isotopes of mercury. *Phys. Rev.*, 78:487, 1950.

[13] L.N. Cooper. Bound electron pairs in a degenerate fermi gas. *Physical Review*, 104:1189–1190, 1956.

[14] L.D. Landau. *Zh. Eksperim. Teor. Fiz.*, 7:19, 1937.

[15] L.D. Landau. *Zh. Eksperim. Teor. Fiz.*, 7:627, 1937.

[16] F. London. *Superfluids*. Wiley, New York, 1950.

[17] S. Hunklinger. *Festkörperphysik*. Oldenbourg Wissenschaftsverlag GmbH, 2007.

[18] P. G. de Gennes. *Superconductivity of metals and alloys*. Westview Press, 1999.

[19] T. Klein K. van Beek. Images de la physique. Technical report, Institut Neel, 2002.

[20] M. Näbauer R. Doll. *Phys. Rev. Lett.*, 7:51, 1961.

[21] W.M. Fairbank B.S. Deaver. *Phys. Rev. Lett.*, 7:43, 1961.

[22] H. Träuble U. Essmann. *Physics Letters*, 24A:526, 1967.

[23] R.B. Robinson H. F. Hess. *Phys. Rev. Lett.*, 62:214, 1989.

[24] B. D. Josephson. *Phys. Lett.*, 1:251, 1962.

[25] D. Mailly K. Hasselbach, J. R. Kirtley. *Journal of Applied Physics*, 91:4432, 2002.

[26] J. Kirtley. *Rep. Prog. Phys.*, 73:126501, 2010.

[27] J.R. Kirtley K. Hasselbach, D. Mailly. Micro-superconducting quantum interference device

characteristics. *Journal of Applied Physics*, 91(7):4432, 2002.

[28] K.K. Likharev L.A. Yakobson. *Zh. Tekh. Fiz.*, 45:1503, 1975.

[29] L. P. Gor'kov. *Zh. Eksperim. Teor. Fiz.*, 36:1918, 1959.

[30] M. Tinkham. *Introduction to superconductivity*. McGraw-Hill International Editions, 1996.

[31] S. H. Pan. *International Patent Publication No. WO 93/19494*, International Bureau, World Intellectual Property Organization, 1993.

[32] J.T. Peltonen J.P. Pekola H. Courtois, M. Meschke. *PRL*, 101:067002, 2008.

[33] W. Rabaud. PhD thesis, Université Joseph Fourier, 2001.

[34] C. Gerber E. Weibel G. Binnig, H. Rohrer. *Phys. Rev. Letters*, 49:57–61, 1982.

[35] C. Gerber E. Weibel G. Binnig, H.Rohrer. *Phys. Rev. Lett.*, 50:120–123, 1983.

[36] C. Gerber G. Binnig, C.F. Quate. *Phys. Rev. Lett.*, 56:930–933, 1986.

[37] F.J. Giessibl. PhD thesis, LMU Munich, Germany, 1991.

[38] G. Binnig F.J. Giessibl. *Ultramicroscopy*, 42-44:281–286, 1992.

[39] P. Hansma D. Rugar. *Phys. Today*, 43:23–30, 1990.

[40] T.E. Carver C.F. Quate T.R. Albrecht, S. Akamine. *J. Vac. Sci. Technol. A*, 8:3386–3396, 1990.

[41] C.F. Quate S. Akamine, R.C. Barrett. *Applied Physics Letters*, 57:316–318, 1990.

[42] C. Quate M. Tortonese, R.C. Barrett. *Applied Physics Letters*, 62:834–836, 1993.

[43] H.K. Wickramasinghe Y. Martin, C.C. Williams. *J. Appl. Phys.*, 61:4723–4729, 1987.

[44] F. J. Giessibl. Advances in atomic force microscopy. *Reviews of Modern Physics*, 75:949, 2003.

[45] R. D. Grober K. Karrai. Piezo-electric tuning fork tip-sample distance control for near field optical microscopes. *Ultramicroscopy*, 61:197, 1995.

[46] F.J. Giessibl. *Phys. Rev. B*, 56:16010–16015, 1997.

[47] F. Bertin. Cours de microscopie à force atomique. Cours de Master MnsGI, UJF Grenoble.

[48] E. Kaxiras M.Z. Bazant. *Phys. Rev. B*, 56:8542–8552, 1997.

[49] G. Baym. *Lectures on Quantum Mechanics*. Westview Press, 1974.

[50] F.J. Giessibl. *APL*, 76:1470–1472, 2000.

[51] K. Kim W. Jhe M. Lee, J. Jahng. *APL*, 91:023117, 2007.

[52] J. Schuck D. Hessmann P. Kindelmann J. Hespanha A.S. Morse K. Karrai I. Tiemann S. Manus R.D. Grober, J. Acimovic. *RSI*, 71:2776, 2000.

[53] H. le Sueur. PhD thesis, Quantronics Group, SPEC, CEA-Saclay, 2000.

[54] N. Venturi S. Field J. Siegel, J. Witt. *Review of Scientific Instruments*, 66:2520, 1995.

[55] O.V. Lounasmaa. *Experimental Principles and Methods Below 1K*. Academic Press, 1974.

[56] K. H. Kuit, J. R. Kirtley, W. van der Veur, C. G. Molenaar, F. J. G. Roesthuis, A. G. P. Troeman, J. R. Clem, H. Hilgenkamp, and H. Rogalla. *Phys. Rev. B*, 77:134504, 2008.

[57] Besancon G. Ahmad I., Voda A. *Proceedings of 48th IEEE Conference on Decision & Control - 48th IEEE Conference on Decision & Control*, 2009.

[58] S.J. Bending. *Advances in Physics*, 48:449–535, 1999.

[59] J.P. Wiksmo J.R. Kirtley. *Annu. Rev. Mater. Sci*, 29:117, 1999.

[60] T. Akashi H. Kasai T. Matsuda F. Nori A. Maeda A. Tonomura Y. Togawa, K. Harada. *PRL*, 95:087002, 2005.

[61] P.L. Gammel T.H. Johansen P.E. Goa H. Hauglin M. Baziljevich, E. Il'yashenko. *Superconductor Science and Technology*, 14:729–731, 2001.

[62] A.A.F. Olsen M. Baziljevich T.H. Johansen P.E. Goa, H. Hauglin. *Review of Scientific Instruments*, 74:141, 2003.

[63] C. Van Haesendonck Y. Bruynseraede A. Volodin, K. Ternst. Low temperature magnetic force microscopy with enhanced sensitivity based on piezoresistive detection. *Review of Scientific Instruments*, 71(12):4468, 2000.

[64] E.W.J. Straver J.E. Hoffman N.C. Koshnick E. Zeldov D.A. Bonn R. Liang W.N. Hardy K.A. Moler O.M. Auslaender, L. Luan. *Nature Physics Letters*, 5:35, 2009.

[65] O.M. Auslaender D. Rugar K.A. Moler E.W.J. Straver, J.E. Hoffman. *APL*, 93:172514, 2008.

[66] M. Henini A.Oral, S.J. Bending. *APL*, 69:1324, 1996.

[67] W. Gillijns K. de Keyser K. Vervaeke V.V. Moshchalkov T. Nishio, Q. Chen. *PRB*, 77:012502, 2008.

[68] S.J. Bending. *Physica C*, 470:754–757, 2010.

[69] M. Dede A. Oral A. Sandhu, K. Kurosawa. *Japanese Journal of Applied Physics*, 43:777, 2004.

[70] J.A. Bert C.W. Hicks J. Large H. Edwards K.A. Moler N.C. Koshnick, M.E. Huber. *APL*, 93:243101, 2008.

[71] Y. Myasoedov M.L. Rappaport L. Ne'eman D. Vasyukov E. Zeldov M.E. Huber J. Martin A. Yacoby A. Finkler, Y. Segev. *Nano Letters*, 10:1046, 2010.

[72] K.G. Stawiasz J.S. Sun W.J. Gallagher S.H. Blanton S.J. Wind J.R. Kirtley, M.B. Ketchen. *APL*, 66:1138, 1995.

[73] F.W.J. Hekking L. Levy B. Pannetier R. Dolata A.B. Zorin N. Didier A. Fay E. Hoskinson F. Lecocq Z.H. Peng I.M. Pop O. Buisson, W. Guichard. *Quantum Inf Process*, 8:155, 2009.

[74] R.P. Huebener. *Magnetic Flux Structure in Superconductors*. Springer-Verlag, 1979.

[75] C.P. Bean. *PRL*, 8:250, 1962.

[76] C. Veauvy. *Imagerie magnétique par micro-SQUID à basse température*. PhD thesis, Université Joseph Fourier, 01 2002.

[77] J.G. Analytis J.-H. Chu I.R. Fisher K.A. Moler B. Kalisky, J.R. Kirtley. *arXiv:1012.4271*, 2010.

[78] T.M. Lippman-C.W. Hicks B. Kalisky J.-H. Chu J. G. Analytis I.R. Fisher J.R. Kirtley K.A. Moler L. Luan, O. M. Auslaender. *PRB*, 81:100501, 2010.

[79] B. Cabrera M.E. Huber G.S. Park, C.E. Cunningham. *PRL*, 68:1920, 1992.

[80] T. Proslier Y. Noat W. Sacks D. Roditchev-G. Giubileo F. Bobba A.M. Cucolo N. Zhigaldo S.M. Kazakov J. Karpinski A. Kohen, T. Cren. *APL*, 86:212503, 2005.

[81] P. Diener P. Rodiere J.P. Brison R. Prozorov-T. Olheiser R.W. Giannetta J.D. Fletcher, A. Carrington. *PRL*, 98:057003, 2007.

[82] A. Hosseini D. A. Bonn W.N. Hardy S. Kamal, R. Liang. *PRB*, 58:R8933, 1998.

[83] P. Pincas. *PRL*, 13:21, 1964.

[84] E. Baggio-Saitovitch S.L. Budko P.C. Canfield J.P. Carlo T. Goko J. Munevar N.Ni Y.J. Uemura W. Yu M. Luke T.J. Williams, A.A. Aczel. *PRB*, 80:094501, 2009.

[85] D. Pal, L. DeBeer-Schmitt, T. Bera, R. Cubitt, C. D. Dewhurst, J. Jun, N. D. Zhigadlo, J. Karpinski, V. G. Kogan, and M. Eskildsen. *PRB*, 73:012513, 2006.

[86] J. Pearl. Structure of superconductive vortices near a metal-air interface. *Journal of Applied Physics*, 37(11):4139, 1966.

[87] J.R. Clem. *Journal of Low Temperature Physics*, 18:427, 1974.

[88] H. F. Hess H. L. Kao J. Kwo A. Sudbo T. Y. Chang A. M. Chang, H. D. Hallen. *Europhysics Letters*, 20:645–650, 1992.

[89] L. Harriott H.F. Hess H.L. Kao J. Kwo R.E. Miller R. Wolfe J. van der Ziel A. M. Chang, H.D. Hallen. *Applied Physics Letters*, 61:1974, 1992.

[90] M. Ledvij V. G. Kogan, A. Yu. Simonov. *PRB*, 48:392, 1993.

[91] E. H. Brandt G. Carneiro. *PRB*, 61:6370, 2000.

[92] K.A. Moler V.G. Kogan J.R. Clem A.J. Turberfield J.R. Kirtley, C.C. Tsuei. *Applied Physics Letters*, 74:4011, 1999.

[93] C. Veauvy. PhD thesis, UJF Grenoble, 2002.

[94] J.R. Clem K.A. Moler J.R. Kirtley, V.G. Kogan. *PRB*, 59:4343, 1999.

[95] S.A. Teukolsky W.T. Vetterling W.T. Press, B.P. Flannery. *Numerical Recipes in C*. Cambridge University Press, 1988.

[96] R. J. Creswick R. Prozorov C. P. Poole Jr., H. A. Farach. *Superconductivity*. Academic Press, 2007.

[97] K.V. Samokhin V.P. Mineev. *Introduction to Unconventional Superconductivity*. Gordon and Breach Science Publishers, 1999.

[98] A. Garg S. Yip. *PRB*, 48:3304, 1993.

[99] K. Ueda M. Sigrist. *Review of Modern Physics*, 63:239, 1991.

[100] C.D. Bredl W. Lieke D. Meschede W. Franz H. Schaefer F. Steglich, J. Aarts. *PRL*, 43:1892–1896, 1979.

[101] K.A. Mueller J.G. Bednorz. *Z. Phys. B*, 64:189, 1986.

[102] J.K. Hulm G.F. Hardy. *Phys. Rev.*, 87:884, 1953.

[103] J. Prigent R. Chevrel, M. Sergent. *J. Solid State Chem.*, 3:515, 1971.

[104] B. Batlogg H. W. Zandbergen J. J. Krajewski W. F. Peck Jr R. B. van Dover R. J. Felder T. Siegrist K. Mizuhashi† J. O. Lee† H. Eisaki† S. A. Carter & S. Uchida† R. J. Cava, H. Takagi. *Nature*, 367:146, 1994.

[105] T. Muranaka Y. Zenitani J. Akimitsu J. Nagamatsu, N. Nakagawa. *Nature*, 63, 2001.

[106] W.A. Little. *Phys. Rev.*, 134:A1416, 1964.

[107] M. Ribault K. Bechgaard D. Jerome, A. Mazaud. *C.R. Hebd. Acad. Sci. Ser.*, B290:27, 1980.

[108] V.A. Stenger C.H. Pennington. *Review of Modern Physics*, 68:885, 1996.

[109] N. Wang X.X. Zhang G.H. Wen G.D. Li J.N. Wang C.T. Chan P. Sheng Z.K Tang, L. Zhang. *Science*, 292:2462, 2001.

[110] C.J. Torng P.H. Hor R.L. Meng L. Gao Z.J. Huang Y.Q. Wang C.W. Chu M.K. Wu, J.R. Ashburn. *PRL*, 58:908–910, 1987.

[111] M. Hirano H. Hosono Y. Kamihara, T. Watanabe. *J. Am. Chem. Soc.*, 130:3296, 2008.

[112] C. Pfleiderer. *Review of Modern Physics*, 81:1551, 2009.

[113] S.Doniach. *Physica B*, 91:231, 1977.

[114] J. Appel D. Fay. *PRB*, 22:3137–3182, 1980.

[115] H.H. Hill. *Nuclear Metallurgy*, 17, 1970.

[116] L.E. DeLong R.W. McCallum M.B. Maple B.T. Matthias W.A. Fertig, D.C. Johnson. *PRL*, 38:987, 1977.

[117] M. Peter V. Jaccarino. *PRL*, 9:290, 1962.

[118] A.I. Buzdin M. Faure. *PRL*, 94:187202, 2005.

[119] K. Ahilan F.M. Grosche R.K.W. Haselwimmer M.J. Steiner E. Pugh I.R. Walker S.R. Julian P. Monthoux S.S. Saxena, P. Agarwal. *Nature*, 406:587, 2000.

[120] T. Fujiwara T.C. Kobayashi E. Yamamoto Y. Haga R. Settai Y. Onuki T. Akazawa, H. Hidaka. *J. Phys. Condens. Matter*, 16:L29, 2004.

[121] D.E. de Nijs Y. Huang J.C.P. Klaasse T. Gortenmulder A. de Visser A. Hamann T. Goerlach H.v. Loehneysen N.T. Huy, A. Gasparini. *PRL*, 99:067006, 2007.

[122] E. Ressouche D. Braithwaite J. Flouquet J.P. Brison E. Lhotel C. Paulsen D. Aoki, A. Huxley. *Nature*, 413:6856, 2001.

[123] K. Ishida Y. Nakai E. Osaki K. Deguchi N. K. Sato I. Satoh T. Ohta, T. Hattori. *Journal of Physical Society Japan*, 79:023707, 2010.

[124] A. de Visser N.T. Huy, Y.K. Huang. *Journal of Magnetism and Magnetic Materials*, 321:2691–2693, 2009.

[125] N.T. Huy. *Ferromagnetism, Superconductivity and Quantum Criticality in Uranium Intermetallics*. PhD thesis, van der Waals-Zeeman Instituut, Universiteit van Amsterdam, 2008.

[126] F. Lévy. PhD thesis, Université Joseph Fourier, 2003.

[127] Y.K. Huang A. de Visser N.T. Huy, D.E. de Nijs. *PRL*, 100:077002, 2008.

[128] L. Taillefer G.G. Lonzarich. *Journal of Physics C: Solid State Physics*, 18:4339, 1985.

[129] N.T. Huy J.C.P. Klaasse T. Naka E. Slooten A. de Visser A. Gasparini, Y.K. Huang. *Journal of Low Temperature Physics*, 2010.

[130] C. Meingast P. Schweiss P. Burger H. v. Loehneysen J. Flouquet F. Hardy, D. Aoki. *arxiv.org*, 1012.5097, 2010.

[131] V. Sechovsky J. Poltierova Vejpravova, J. Pospisil. *[cond-mat.str-e]*, 0806.3561, 2008.

[132] J. Prokleska K. Prokes A. Stunault V. Sechovsky J. Vejpravova-Poltierova, J. Pospisil. *PRB*, 82:180517, 2010.

[133] J. Hartbaum H.v. Loehneysen A. de Visser A. Gasparini, Y.K. Huang. *PRB*, 82:052502, 2010.

[134] A. Gasparini D.E. de Nijs D. Andreica C. Baines A. Amato A. de Visser, N.T. Huy. *PRL*, 102:167003, 2009.

[135] A. de Visser N.T. Huy. *Solid State Communications*, 149:703–709, 2009.

[136] S. Ban N. Tamura Y. Simura T. Sakakibara I. Satoh N.K. Sato K. Deguchi, E. Osaki. *Journal of Physicsal Society Japan*, 79:083708, 2010.

[137] V. Taufour E. Hassinger G. Knebel J. Flouquet D. Aoki, T. D. Matsuda. *J. Phys. Soc. Jpn.*, 78:113709, 2009.

[138] K. Ishida Y. Nakai E. Osaki K. Deguchi N.K. Sato I. Satoh Y. Ihara, T. Hattori. *PRL*, 105:206403,

2010.

[139] A. Gasparini Y.K. Huang A. de Visser E. Slooten, T. Naka. *PRL*, 103:097003, 2009.

[140] G. Knebel J. Flouquet E. Hassinger, D. Aoki. *Journal of Physics: Conference Series*, 200:012055, 2010.

[141] D. Aoki J. Flouquet E. Hassinger, G. Knebel. *Phys. Soc. Jpn*, 77:115117, 2008.

[142] V.P. Mineev. *AIP Conference Proceedings*, 1134:68–73, 2009.

[143] Tatsuma D. Matsuda Valentin Taufour Georg Knebel Dai Aoki, Ilya Sheikin and Jacques Flouquet. *J. Phys. Soc. Jpn.*, 80:013705, 2011.

[144] V.P. Mineev. *PRB*, 66:134504, 2002.

[145] T. Champel V.P. Mineev. *PRB*, 69:144521, 2004.

[146] Y.K. Huang B. Fak E. Ressouche K. Prokes, A. de Visser. *PRB*, 81:180407, 2010.

[147] Touraj Nikazad. *The Use of Landweber Algorithm in Image Reconstruction*. PhD thesis, Linköping Studies in Science and Technology, 2007.

[148] L. Peng W. Q. Yang. *Meas. Sci. Technol.*, 14:R1 – R13, 2003.

[149] Soshin Chikazumi. *Physics of Magnetism*. John Wiley & Sons, 1964.

[150] B. Lebech P.J. Brown O. Vogt K. Mattenberger G.H. Lander, M.S.S. Brooks. *APL*, 57:989, 1990.

[151] Private communication with Carley Paulsen.

[152] R. Schäfer A. Hubert. *Magnetic Domains*. Springer, 2000.

[153] Marc Drillon Joel S. Miller. *Magnetism: Nanosized magnetic materials*. Wiley-VCH, 2002.

[154] M. Kustov. *Characterisation and design of micro-magnets for the diamagnetic levitation of micro- and nanoparticles*. PhD thesis, Grenoble University, 2010.